
**GAS-PHASE STUDIES OF
ASTROPHYSICAL RELEVANT
POLYCYCLIC AROMATIC
HYDROCARBON IONS**



Benedikte Klærke

Department of Physics and Astronomy
Aarhus University, Denmark

PhD Thesis
December 2012

Contents

Preface	iii
List of publications	v
Outline	ix
1 Introduction	1
2 PAHs and the interstellar medium	3
2.1 Identification of interstellar PAHs	4
2.2 Properties of interstellar PAHs	6
2.3 The role of interstellar PAHs	10
2.4 Experimental astrophysics	13
3 Theory and numerical methods	17
3.1 Radiative lifetime	21
3.2 Density functional theory	22
4 Experimental techniques	27
4.1 Ion sources	28
4.2 ELISA	31
5 Methyl substituted quinoline	41
5.1 Experimental and numerical details	42
5.2 Results	43
5.3 Conclusions and outlook	52
6 Hydrogenated PAHs	55
6.1 Introduction	55
6.2 Hydrogen addition to PAHs	58
6.3 Absorption spectra of HPAHs	74

6.4 Summary and outlook	98
7 Summary	101
8 Dansk resumé	103
9 Acknowledgements	105
References	107

Preface

This thesis has been submitted to the Graduate School of Science and Technology at the Faculty of Science and Technology, Aarhus University, Denmark, in order to fulfil the requirements for the PhD degree. The work presented in this thesis has been performed in a collaboration between my two supervisors, Professor Lars H. Andersen and Associate Professor Liv Hornekær, in the period from August 2009 to December 2012.

My training and day-to-day scientific life have been with the Molecular Dynamics group led by Lars H. Andersen, which means that I have also participated in the laboratory work on the main interest of the group: biological relevant chromophores. This has resulted in several publications. In the list of publications, the title, author list, and abstract of the published work related to this part of my PhD are given, but this topic will not be touched further upon in the thesis. Besides this, I have participated in the construction work of a new electrostatic storage ring SAPHIRA and a fragment analyser – both installed at the Separator II facility in Aarhus. The applications of these setups are discussed only in the context of possible experiments with PAHs.

List of publications

The work of this thesis has led to the two following publications:

- **B. Klærke**, A. I. S. Holm, and L. H. Andersen,
UV action spectroscopy of protonated PAH derivatives. Methyl substituted quinolines
Astron. & Astrophys., (532), A132 (2011)
- **B. Klærke**, Y. Toker, D. B. Rahbek, L. Hornekær, and L. H. Andersen,
Formation and stability of hydrogenated PAHs in gas phase
Astron. & Astrophys., (549), A84 (2012)

During my PhD-studies I have also contributed to the following publications that are not related to the topic of this thesis:

- T. Rocha-Rinza, O. Christiansen, D. B. Rahbek, **B. Klærke**, L. H. Andersen, K. Lincke, and M. B. Nielsen,
Spectroscopic implications of the electron donor-acceptor effect in the photoactive yellow protein chromophore
Chem. Eur. Jour. **16**, 11977 (2010)
Abstract: The importance of the donor-acceptor push-pull system in the photoabsorption of the trans p-coumaric acid, the cofactor within the photoactive yellow protein and other xanthopsins, has been investigated. We recorded gas-phase absorption spectra and performed high-level quantum chemical calculations of three chromophore models, namely, the deprotonated trans ortho-, meta- and para-methyl coumarates. The ortho and para isomers, which have the electron-donating phenoxy oxygen and the electron-withdrawing acyl group in conjugation, present absorptions in the high-energy region of the visible spectrum, that is, in the interval of wavelengths in which the photoactivity of the xanthopsins is observed. On the other hand, the meta isomer, in which the conjugation between the phenoxy and acyl groups is disrupted, exhibits a significantly shifted maximum and presents no absorption in the region from blue to ultraviolet A. It is found that the push-pull system in the trans p-coumaric acid is critical for

the wavelength and the intensity of its photoabsorption. Absorption spectra were also measured in methanol and showed an appreciable hypsochromic effect. Linear response calculations within the formalism of the approximate coupled cluster singles and doubles CC2 model and time-dependent DFT using the functional CAM-B3LYP provided insights into the relevant processes of excitation and aided to the interpretation of the experimental results. There is good agreement between theory and experiment in the description of the gas-phase absorption spectra of the considered chromophore models. Differential density plots were used to predict the effect of hydrogen-bonded amino acids to the trans p-coumaric acid on the protein tuning of this chromophore.

- K. Lincke, T. Sølling, L. H. Andersen, **B. Klærke**, D. B. Rahbek, J. Rajput, C. B. Oehlenschläger, M. Å. Petersen, and M. B. Nielsen, *On the absorption of the phenolate chromophore in the green fluorescent protein – role of individual interactions* *Chem. Commun.* **46**, 734 (2010)
Abstract: Model compounds of the green fluorescent protein (GFP) phenolate chromophore are synthesized and investigated for their intrinsic optical properties by state-of-the-art gas-phase action spectroscopy.
- G. Aravind, R. Antoine, **B. Klærke**, J. Lemoine, D. B. Rahbek, J. Rajput, P. Dugourd, and L. H. Andersen, *Sub-microsecond photodissociation pathways of gas phase adenosine 5'-monophosphate nucleotide ions* *Phys. Chem. Chem. Phys.* **12**, 3486 (2010)
Abstract: The sub-microsecond dissociation pathways for the protonated and deprotonated forms of adenosine 5'-monophosphate were probed in the gas phase using a linear time of flight spectrometer. The studies show two dissociation pathways for the AMP ions indicating dominant ergodic pathways in the photodissociation of these species. The photofragmentation was determined to be a single photon process for the AMP ions. Photodetachment of the AMP anion excited at 266 nm was not observed, leaving dissociation as the prominent pathway for relaxation of the excess energy in the biomolecule. The photofragments were analysed at the electrostatic ion storage ring (ELISA) and found to be similar to collision induced fragments in the case of anions but different in the case of cations.
- G. Aravind, **B. Klærke**, R. Rajput, Y. Toker, L. H. Andersen, B. V. Bochenkova, R. Antoine, J. Lemoine, A. Racaud, and P. Dugourd *Photodissociation pathways and lifetimes of protonated peptides and their dimers* *Jour. Chem. Phys.* **136**, 014307 (2012)
Abstract: Photodissociation lifetimes and fragment channels of gas-phase, protonated YAn ($n = 1,2$) peptides and their dimers were measured with 266 nm photons. The protonated monomers were found to have a fast dissociation channel with an exponential lifetime of ~ 200 ns while the protonated dimers show an additional slow dissociation component with a lifetime of $\sim 2 \mu\text{s}$. Laser power dependence measurements enabled us to ascribe the fast channel in the

monomer and the slow channel in the dimer to a one-photon process, whereas the fast dimer channel is from a two-photon process. The slow (1 photon) dissociation channel in the dimer was found to result in cleavage of the H-bonds after energy transfer through these H-bonds. In general, the dissociation of these protonated peptides is non-prompt and the decay time was found to increase with the size of the peptides. Quantum RRKM calculations of the microcanonical rate constants also confirmed a statistical nature of the photodissociation processes in the dipeptide monomers and dimers. The classical RRKM expression gives a rate constant as an analytical function of the number of active vibrational modes in the system, estimated separately on the basis of the equipartition theorem. It demonstrates encouraging results in predicting fragmentation lifetimes of protonated peptides. Finally, we present the first experimental evidence for a photo-induced conversion of tyrosine-containing peptides into monocyclic aromatic hydrocarbon along with a formamide molecule both found in space.

- Y. Toker, D. B. Rahbek, **B. Klærke**, A. V. Bochenkova, and L. H. Andersen
Direct and indirect electron emission from the green fluorescent protein chromophore
Phys. Rev. Lett. **109**, 128101 (2012)
Abstract: Photoelectron spectra of the deprotonated green fluorescent protein chromophore have been measured in the gas phase at several wavelengths within and beyond the S₀-S₁ photoabsorption band of the molecule. The vertical detachment energy (VDE) was determined to be 2.68 ± 0.1 eV. The data show that the first electronically excited state is bound in the Franck-Condon region, and that electron emission proceeds through an indirect (resonant) electron-emission channel within the corresponding absorption band.
- A. V. Bochenkova, J. Rajput, D. B. Rahbek, **B. Klærke**, and L. H. Andersen,
Nuclei versus electrons, a striking ultrafast dual photoresponse of bio-chromophores prompted by nature
Submitted to Nature Chemistry
- D. B. Rahbek, Y. Toker, A. V. Bochenkova, **B. Klærke**, and L. H. Andersen,
Inhomogeneous broadening in spectral shapes of the protonated GFP chromophores: para- versus meta-effects
In preparation
- Y. Toker, D. B. Rahbek, **B. Klærke**, J. Rajput, A. V. Bochenkova, and L. H. Andersen,
Electronic dynamics in photo-detachment channels of the PYP chromophore probed by photo-electron spectroscopy
In preparation

Outline

This PhD thesis is organised as described below:

Chapter 1 shortly introduces the molecular family of polycyclic aromatic hydrocarbons (PAHs) and their scientific relevance.

Chapter 2 gives an overview of the field of PAHs in an astrophysical context. A few historical remarks are made along with a description of the identification of interstellar PAHs. Their properties and physical and chemical role in the interstellar medium are discussed, and a short summary of the experimental techniques used to investigate the molecules is given.

Chapter 3 starts with a quick exposition of relevant concepts of molecular physics. Thereafter, a description of the applied method to obtain radiative lifetimes of hot ions is given. The chapter ends with an introduction to the computational method of density functional theory (DFT), its time-dependent version (TD-DFT), and finally a short review of the errors and limitations of the methods.

Chapter 4 presents the experimental setups used to produce the results of this thesis. Two different types of ion sources (the Nielsen plasma ion source and the electrospray ion source) were used for the production of hydrogenated PAHs. Subsequently, details of the electrostatic storage ring ELISA is given, and finally the concepts of the data analysis are explained.

Chapter 5 is based on the publication *UV action spectroscopy of protonated PAH derivatives. Methyl substituted quinolines* published in *Astronomy &*

Astrophysics **532**, A132 (2011) [1]. The absorption spectrum, dissociation lifetime, and dissociation channels obtained at 210 – 330 nm are presented and discussed for four different methyl substituted quinoline isomers. DFT and TD-DFT calculations are used to support and explain the experimental results.

Chapter 6 introduces the relevance of hydrogenated PAHs especially in the context of acting as catalysts in production of molecular hydrogen. Two separate experimental studies were performed to illustrate different aspect of the field. First, experimental and computational results on formation and stability of hydrogenated PAHs are presented. This work is published in *Formation and stability of hydrogenated PAHs in gas phase*, Astronomy & Astrophysics **549**, A84 (2012) [2]. Secondly, preliminary results on action absorption spectra, dissociation lifetimes, and dissociation channels for the radical cations of pyrene and two hydrogenated forms of pyrene, tetrahydropyrene, and hexahydropyrene, are presented and discussed.

Chapter 7 shortly summarises the thesis.

Chapter 8 is a summary in Danish.

Chapter 9 acknowledges the people who have played a role in the making of this thesis.

CHAPTER 1

Introduction

Polycyclic aromatic hydrocarbons (PAHs) are a family of aromatic molecules consisting of honeycomb carbon skeletons consisting of fused six-member, aromatic rings with hydrogen atoms at the edge sites. The electronic orbitals of the carbon atoms are sp^2 -hybridised resulting in a planar structure of the molecules. The remaining p-orbitals combine to form a large delocalised electronic orbital, which spans the entire molecule. The smallest PAH is naphthalene, which consists of only two rings, while the larger PAHs contain hundreds of aromatic rings. Due to the aromaticity, the molecules are very stable. Figure 1.1 shows a selection of smaller PAHs along with modified versions: substituted and hydrogenated PAHs and PAHs with side chains.

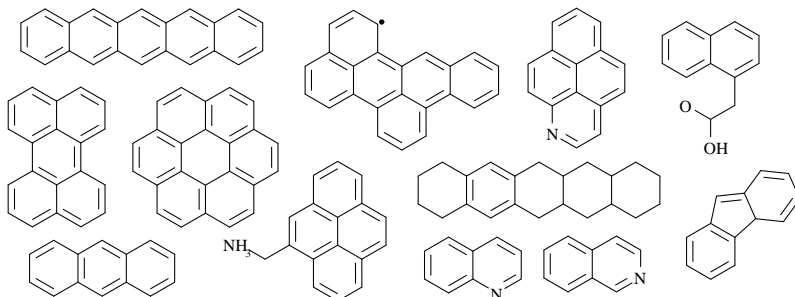


Figure 1.1: PAHs can be found in many different forms. Here, a selection of smaller PAHs is shown along with substituted (a CH group has been replaced by an N atom), hydrogenated (the rings lose their aromaticity), and side chains (e.g. NH_3 and CH_2COOH).

On Earth, the PAHs are found in oil, coals, and cigarette smoke, and are important by-products of petroleum manufacturing. They are also a major component of the soot formed in combustion processes. Therefore, they represent an important class of pollutants because of their known biological activity [3]. However, the main motivation for my PhD thesis is the presence of PAHs in the interstellar medium.

During recent years, observational evidence has made it clear that polycyclic aromatic hydrocarbons (PAHs) are ubiquitous in the interstellar medium (ISM) [4]. As one of the major molecular species, they are expected to carry 5-10% of the total amount of interstellar carbon [5]. It has been suggested that PAHs may be intimately involved in the molecular origin of life [6, 7], and as carriers of interstellar infrared and UV/visible spectral features. They may also act as interstellar catalysts for the formation of molecular hydrogen (H_2) [8, 9] – the most abundant molecule in space.

CHAPTER 2

PAHs and the interstellar medium

The interstellar medium (ISM) consists of gas and dust particles grouped in clouds of varying densities ($10^{-1} - 10^6$ atoms/cm 3) and fills the space between the stars in galaxies. In the densest regions, stars are formed. The ISM is detectable as light is emitted, absorbed, and reflected by the particles. In total, the ISM makes up 10 % of the mass of the Milky Way of which 99 % is gas particles and only 1 % is dust grains. The dust particles consist of ice, silicates and probably also graphite, while by far the most abundant atoms in the ISM are hydrogen (89 %) and helium (9 %). However, nearly all elements with atomic numbers up to 30 (zinc) have been detected [10].

More than 200 molecular species have been identified in the ISM – from small di- and triatomic molecules to larger molecules, such as C₆₀ and C₇₀ [11]. Due to the strong ultraviolet radiation field in some regions, cations are present. In other regions, anions are thought to be formed by electron attachment to neutral molecules [12]. Interstellar molecules can be identified through their electronic, vibrational, and rotational spectra in the UV-visible, infrared, and radio range of the electromagnetic spectrum, respectively.

As mentioned above, PAHs are a major class of interstellar molecules and carry a substantial part of the interstellar carbon atoms. PAHs are found in all sorts of interstellar objects such as reflection nebulas, planetary nebulas, HII regions, diffuse interstellar clouds, and photodissociation regions. This chapter gives a brief overview of the knowl-

edge on interstellar PAHs.

2.1 Identification of interstellar PAHs

The PAH hypothesis (see below) was first proposed in the mid 1980's independently by A. Leger and J. L. Puget [13] and L. Allamandola [14] in the context of identifying the mysterious carriers of a family of unidentified infrared emission bands, at that time known as UIRs. The UIRs are now known as the aromatic infrared bands (AIRs) due to their aromatic origin. The AIRs consist of strong IR emission features at 3.3, 6.2, 7.7, 8.6, and 11.2 μm . They are observed in interstellar spectra from all sorts of astronomical objects, which are associated with dust and gas particles and are illuminated by UV photons. These features are observed in the Milky Way as well as in nearby galaxies. The AIRs are believed to stem from free neutral or ionised PAHs pumped by UV, visible, and/or NIR photons. These features were first observed and reported by F. C. Gillett *et al.* in 1973 [15].

The PAH hypothesis was summarised by A. G. G. M. Tielens at the 25th anniversary symposium in 2010 [5] as:

- A substantial fraction of the carbon in the universe is in form of PAH molecules.
- A substantial fraction of the UV-visible radiative stellar energy in galaxies is "transformed" by PAHs to the mid-IR range.
- PAH molecules may provide observational signatures throughout the full spectral range from the extreme ultraviolet to the radio regime.
- PAHs are at the basis of a complex chemistry in the ISM of galaxies.
- PAHs contribute to many key processes that affect the basic structure and evolution of the interstellar medium of galaxies.

Figure 2.1 shows the AIRs from 3 – 20 μm on top of broad plateaus for two different astronomical objects along with the characteristic vibrational modes of the PAHs. The plateau is associated with PAHs as subunits of larger carbonaceous grains [17]. As seen in the figure, the

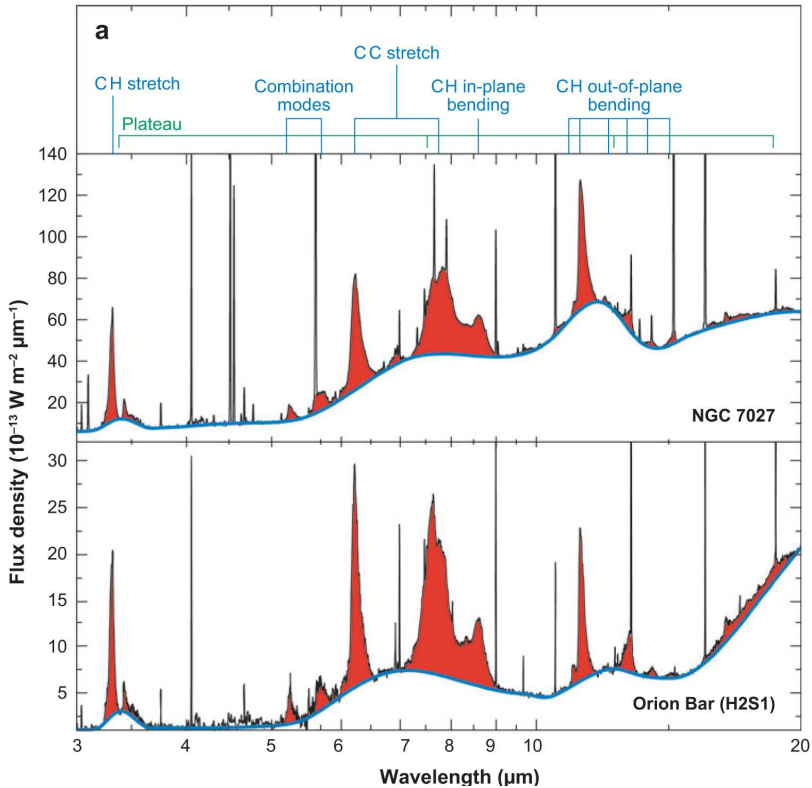


Figure 2.1: Infrared emission spectra of two different astronomical objects: a photodissociation region (Orion Bar) and a planetary nebula (NGC 7027). At the top, the frequencies of the vibrational modes of PAHs are listed and on the two astronomical spectra they are marked with red. The figure is from [16] and reprinted with permission from the publisher.

bands can vary in position, width, and strength indicating a dependence on the local physical conditions [16]. In the high energy part of the IR range (short wavelengths), the vibrational modes mainly involve the C-H bond (either stretching or bending of this bond). These spectral features cannot be used to identify specific PAHs, but only to verify the presence of the molecular family, since these vibrations are almost independent of the size and structure of the molecule. The $3.3\text{ }\mu\text{m}$ band is ascribed to the stretch of the C-H bond in aromatic species. A feature often weaker, but sometimes as strong as the $3.3\text{ }\mu\text{m}$, is found at $3.4\text{ }\mu\text{m}$. This band can most likely be ascribed to hydrogenated PAHs,

in which an extra hydrogen atom is attached to one or more carbon atoms, resulting in destruction of the aromatic characteristics and the planar structure. The frequencies of the skeleton bending and stretching modes lie at lower energies ($15\text{ }\mu\text{m}$ and up in wavelength). Hence, the position and strength of the emission lines at longer wavelengths are more sensitive to the structure of the molecule. In this region, it might be possible to do a more direct identification of the PAHs. At even longer wavelengths, rotational spectra can be used for identification. For this, high precision measurements are necessary as the dipole moment of PAHs is very small.

Another possibility to identify specific interstellar PAHs lie in the visible and UV range. The electronic transitions of a molecule are its fingerprints and can be used for a molecule specific identification. A large family of so far unidentified absorption bands (Diffuse Interstellar Bands, DIBs) have been known since the 1920's [18], and it has long been speculated that PAHs could also be the carriers of these bands [19–24]. A recent catalogue of DIBs obtained from spectra of the binary star system HD 204827 contains 380 confirmed bands in the region $390 – 810\text{ nm}$ [25]. The bands show no apparent regularity in wave number separation and are not only observed in the Milky Way but also in other galaxies. The bands are diffuse and rotational features have been resolved indicating a molecular origin [16, 17, 21–23, 25, 26].

2.2 Properties of interstellar PAHs

A brief overview of the properties of the interstellar PAHs is given below. Interstellar PAHs can reveal details of the conditions and history of the medium. The ionisation balance of the medium is reflected in its charge state, while the distribution in size, composition, and structure give information on the energetic and chemical history [17].

Charge state

The charge state of interstellar PAHs is controlled by the processes of photoionisation and charging by collisions with electrons and ions. The number of charge states is limited by two main factors: the electron affinity and the ionisation potential. For small PAHs, the second electron affinity is typically negative, and doubly charged anions will rapidly emit an electron and become singly charged. For cations, the number

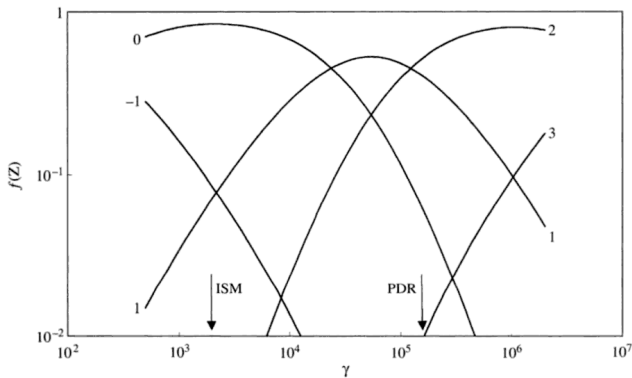


Figure 2.2: Distribution of charge states of circumcoronene ($C_{54}H_{18}$) as a function of the ionisation parameter, γ . On the figure, values of γ for diffuse interstellar clouds (ISM) and photodissociation regions (PDR) are marked by the vertical arrows. The figure is from [27] and reprinted with permission from the publisher.

of charge states is limited by the ionisation potential of hydrogen (13.6 eV), since most photons with this energy or higher will be absorbed by the very abundant hydrogen atoms [27]. Figure 2.2 shows the distribution of charge states of circumcoronene ($C_{54}H_{18}$) as a function of the ionisation parameter, γ , which is given by $\gamma = G_0 T^{1/2} / n_e$, where G_0 is the intensity of the radiation field in units of the average interstellar radiation field, T the temperature, and n_e the electron number density. As can be seen, several charge states are present in different interstellar environments. Anions can survive in shielded regions, but are also harder to detect as the light escaping the clouds has been strongly damped by absorption and scattering.

The charge state of the PAHs has a large effect on both their vibrational and electronic spectra, see figure 2.3. In the vibrational spectrum, the band positions can shift a bit, while the relative strength of the vibrational modes is affected more strongly. Thus, the IR emission spectra can be used as an indication of the charge state for PAHs in a certain environment, although this trend applies only for small (less than 50 carbon atoms) PAHs [4]. The ultraviolet extinction can be modelled by a mixture of classical dust particles and PAHs, and charge state variations of the mixture components can explain varying relative strengths of the extinction features [28, 29].

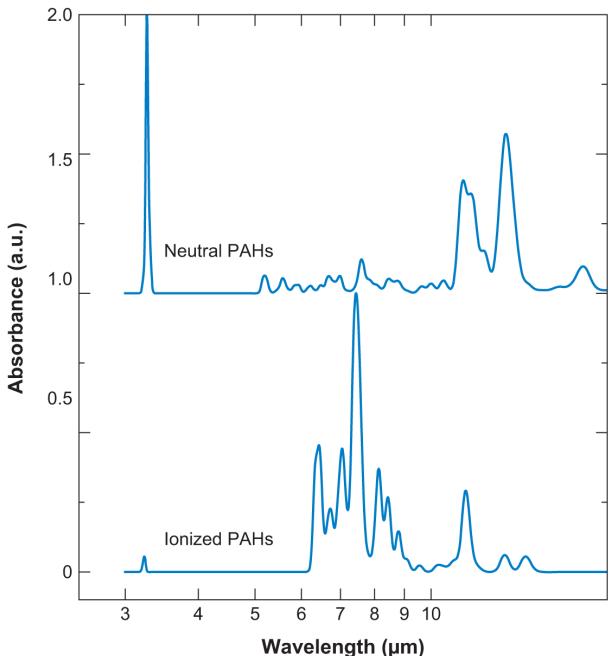


Figure 2.3: Combined IR absorption spectra of antracene, tetracene, 1,2-benanthracene, chrysene, pyrene and coronene in their neutral (top) and cationic (bottom) state. The difference between the two charge states is predominantly seen as a shift in the relative intensities rather than in the position of the frequencies. The figure is from [4] and reproduced by permission of the AAS.

Size distribution

PAHs are often described as the link between interstellar dust grains and gas phase molecules. They are believed to be present in the ISM with sizes ranging from only a few tens of carbon atoms up to several hundred carbon atoms, the larger probably in the shape of clusters of smaller PAHs rather than single, planar PAHs [27]. Again, the AIRs can be used to deduct the size distribution [30]. Figure 2.4 shows the contribution from different sizes of PAHs to some of the prominent IR emission features. As can be seen, the smaller PAHs contribute more to the high energy modes than the larger ones and vice versa for lower energy modes [31]. V. Le Page *et al.* [32] state that small PAHs with about 15 – 20 carbon atoms are quickly destroyed in the normal UV

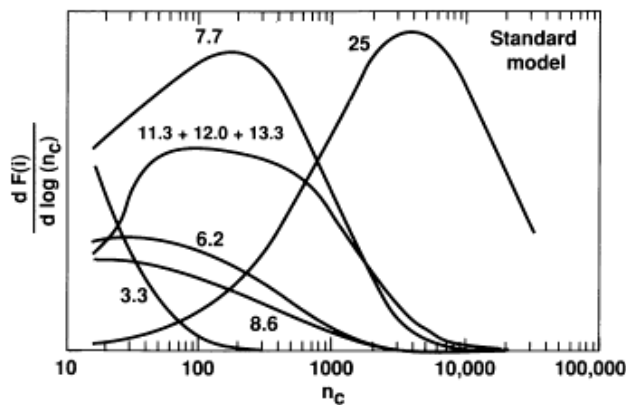


Figure 2.4: Contribution to prominent IR emission features in interstellar spectra as a function of size (number of carbon atoms). The numbers indicate the wavelength of the IR bands in μm . The figure is from [31] and reproduced by permission of the AAS.

radiation field.

The size distribution is also affected by both the charge and hydrogenation state. As an example, completely dehydrogenated ovalene has a photodissociation rate three orders of magnitude greater than ovalene and four times higher than the ovalene cation [33].

Substitution

A range of different substituted PAHs are believed to take part in the interstellar chemistry. The substituted PAHs can be divided into two subgroups: substitution of a skeleton or edge carbon atom, and substitution of a hydrogen atom with a peripheral functional group. The first subgroup includes e.g. nitrogen and oxygen substituted PAHs, the former being the most studied. Nitrogen-containing PAHs have a larger dipole moment than PAHs containing only carbon and hydrogen, and their rotational spectra in the microwave range can be observable. Hence, detection of specific PAHs might be possible at these wavelengths [17]. PAH and metal (iron, silicon and magnesium) complexes have also been investigated and are possible components of the interstellar medium [34].

PAHs with side groups such as methyl, ethyl, and amine have been found in meteorites and in interplanetary dust particles, and some of

these PAHs are believed to be of interstellar origin [35]. A study by S. R. Langhoff *et al.* [3] concludes that adding a methyl or cyano side group does not alter the mid-IR emission spectrum of neither the neutral nor the cationic PAH. On the other hand, a NH₂-side group changes the charge distribution of the neutral molecule and thereby introduces cationic features in the spectrum.

Hydrogenation state

A special case of substitution is the addition or subtraction of hydrogen atoms to/from the peripheral carbon atoms and the carbon atoms of the skeleton. Establishment of the presence of hydrogenation states of PAHs is based on correlation between the frequencies of their vibrational modes and the AIRs [16]. As mentioned above, the aliphatic stretch (e.g. C bonds to two H atoms) is shifted to 3.4 μm from the aromatic 3.3 μm. This emission band is also observed and hydrogenated PAHs are therefore likely components of the interstellar medium [31, 36–38]. Hydrogenated PAHs seem also to affect the 6.2 μm emission band [39]. Dehydrogenated PAHs are also of astrophysical interest and has been investigated in the context of the UV extinction bump [40]. However, so far, a quantitative estimate of the hydrogenation state of interstellar PAH molecules based on observations is not possible.

2.3 The role of interstellar PAHs

PAHs play a crucial role in both the chemistry and physics of the interstellar medium. In these processes, e.g. the charge state of PAHs is an important factor [41]. Also, interstellar PAH characteristics can be used to determine physical parameters such as temperatures, densities, and UV radiation field in certain ranges [42].

At low photon energies, photoionisation is the most relevant process, but at higher energies, photodestruction becomes important. Especially the competition between unimolecular dissociation and radiation emission upon photoexcitation is interesting in an astrophysical context. A photoexcitation process followed by radiation emission is probable to happen repeatedly for a specific molecule. As the absorption probability is low – due to the very low densities of PAHs – simultaneous absorption of more than one photon is on the other hand very unlikely, but can be important in regions with a high UV photon flux.

Different dissociation channels are open: e.g. loss of atomic hydrogen and C₂H₂, and in the context of hydrogenated PAHs, loss of molecular hydrogen is an open question [16, 27].

Gas phase reactions are very important in the interstellar medium owing to the low molecular density. Some of these reactions can lead to the formation of PAHs: reactions between benzene and carbon containing radicals (e.g. CH₃) or C₂H (which has no energy barrier) are both probable paths to growth of PAHs from benzene [43]. In addition, PAH growth can also occur by addition of C₂H₂ and dimerisation. To understand the initiation of the formation of interstellar PAHs, formation of benzene is the key. Different reactions can result in formation of benzene, e.g. reactions between 1-buten-3-ynyl (1-C₄H₃) and C₂H₂ [44, 45], 1,3-butadienyl (1-C₄H₅) and C₂H₂ [46] and 1,3-butadiene (C₄H₆) and C₂H [47]. Small molecules are formed when PAH radical cations react with atoms. The radical cation of naphthalene can react with atomic hydrogen, oxygen, and nitrogen resulting in the formation of protonated naphthalene, CO, and HCN, respectively. However, for bigger PAHs only addition of atomic species to the PAH is observed. Recombination processes of cations with electrons or anions result in neutralisation and dissociation [43].

The high absorption cross section of PAHs in the UV leads to many physical implications on the interstellar medium. When absorbing UV photons with higher energy than the ionisation potential, electrons with a kinetic energy of 1 – 2 eV can be emitted from the PAHs. These emitted photoelectrons heat the surrounding gas by inelastic scattering. The gas is then cooled by collisional excitation of larger atoms and small molecules, which eventually re-emit the energy as visible photons. Hence, the temperature of the gas is controlled by the mechanism of photoelectric heating. Another important mechanism affecting the gas temperature is the shielding of other astronomical objects, which provides an efficient UV screen [41]. The PAHs make a huge contribution to the interstellar extinction and are believed to be responsible for the far-UV nonlinear rise in the extinction curve [48].

Star formation

In general, molecules play a crucial part in the cooling mechanism necessary for star formation. By electronic, vibrational, and rotational excitations, the molecules absorb the energy emitted from the collapsing

matter, which enables further collapsing. At one point, the collapsing system will reach a temperature high enough to cause fusion giving the new born star an energy source supplying the energy needed to stop the collapse. As PAHs are the most abundant molecules after H₂ and CO, they represent a substantial cooling potential in the interstellar medium. The size of the PAHs near star formation is approximately twice as big as found in most interstellar objects. The intense radiation field near the new born star leads to photodissociation (both single and multiphoton contribution) of the PAHs leaving only the bigger, more photostable molecules [16].

2.3.1 Origin of life

It has been suggested that PAHs are linked with the origin of life [6, 7, 49]. Prebiotic molecules (such as amino acids, nucleobases, and simple sugars) observed in the interstellar medium are few compared to aromatic species as they are fragile to heat and radiation. However, meteorites provide protection for the prebiotic molecules and more than 80 different amino acids have been found here.

P. Ehrenfreund *et al.* [6] argue that the prebiotic molecules may have been formed in the interstellar medium and survived the journey to the early Earth, but as the temperature and radiation conditions were harsh, amino acids were not able to assemble into proteins. As described, PAHs are stable to both high temperatures and radiation fields.

In this context, life is defined as a system that "converts resources into building block, grows, replicates, and evolves" [6]. This boils down to three essential, interconnected processes: conversion of available matter into building blocks, replication of template molecules and embedding of the two first processes. PAHs have been suggested as candidates for these three processes. They can be used to build up simple membrane structures providing the necessary container. The PAHs have the ability to transform light into other energy forms. And last, by stacking the PAHs, a compound with similarities to nucleic acids is formed.

The point made by P. Ehrenfreund *et al.* [6] is that all three requirements for simple life are met by one simple molecular family – the PAHs – which happens to be abundant in the interstellar medium and can survive the harsh environment of the early Earth.

2.4 Experimental astrophysics

The knowledge about interstellar PAHs relies on both computational and experimental work performed by many research groups worldwide. In the following, a short summary of the most widely used experimental techniques is given. As mentioned above, the PAH hypothesis was introduced to solve the problem of the IR emission features and great experimental effort has therefore been focused on producing astrophysical relevant data in the IR spectral range. One of the biggest problems has been producing the PAH molecules and ions in a state and under conditions similar to those in the interstellar medium. Note that the physical state of laboratory PAHs with astrophysical relevance is not the same for e.g. IR emission (hot PAHs) and UV absorption (cold PAHs).

Neutral and cationic PAHs have been studied by the technique of matrix isolation spectroscopy (MIS). Gas phase PAHs are condensed on a substrate in a noble gas matrix (neon and argon are most commonly used) at 10 K or less. The absorption (of IR, visible and UV photons) can be investigated by irradiating the matrix with a laser. Irradiation with far UV photons can ionise the sample resulting in the formation of radical cations, and absorption spectra can be produced for the ionised species. The signal-to-noise ratio is rather low as the ionisation efficiency is not very high. Hence, the cation absorption fingerprints can be hard to distinguish from the ones of the neutral molecule. Ionisation may be the most probable process, but the molecules can also undergo dissociation after irradiation – primarily by hydrogen loss resulting in dehydrogenated species. The interaction with the matrix is nearly negligible for neutral molecules, but for cations it results in larger frequency shifts, wider profiles, and larger intensity changes. Many groups have applied this technique over the past 20 years [30, 50–52].

During the last 15 years, cavity ring-down experiments have become a power full tool in the investigation of the electronic transitions of PAHs [53–57]. A solid PAH sample is evaporated and seeded into a cold, supersonic molecular beam. A short laser pulse is guided into a cavity consisting of two highly reflective mirrors. The pulse will then bounce back and forth in the cavity and the intensity of the light that escapes the cavity is measured as a function of time. This decay will be exponential. Letting the gas phase molecules into the cavity will dis-

turb the decay, and direct absorption spectra of the analyte molecule can be constructed. This technique is very powerful as it can be used for both neutrals and ions and, very importantly, for cold molecules. Hot gas phase molecules have also been investigated [58].

Gas phase ions stored in an ion trap have been studied using multiphoton dissociation (MPD) techniques. For these experiments, a free electron laser (tunable in the IR region) supplies the amount of photons needed to cause dissociation. A single IR photon only possesses around 0.05 eV, much less than the 10 eV required to dissociate the molecule. The mass of the photofragments are recorded as a function of the wavelength. The free electron laser, FELIX, in the Netherlands has provided the necessary equipment for the experiment on many small PAHs [59–61]. Another group has made use of this technique but with visible photons [62].

The techniques described above are all based on the principle of absorption. However, as mentioned, the IR features in the interstellar spectra are emission bands. To test the PAH hypothesis directly (not considering the direct identification with electronic absorption spectra) emission spectra are needed as the band intensities may vary from absorption to emission spectra. The technique for measuring infrared emission (IRE) is difficult, especially for ions, due to the complications of space charge. Nevertheless, H. S. Kim *et al.* have succeeded in measuring the IR emission spectra of highly excited gas phase PAH cations [63, 64].

Along with the experimental techniques, the numerical approach of density functional theory (DFT) have been used to investigate different systematic trends of the PAH properties. Combined with the experimental results, a good understanding of the physical processes and properties can be obtained. Several groups have used this method [65–71], and databases of different physical properties of PAHs are available online, with data provided by the NASA Ames group¹ and the Astrochemistry Group in Cagliari, Italy². Ionisation energies, electron affinities, rotational constants, harmonic vibrational frequencies, electronic excited states, and experimental spectra are among the results that can be found.

Figure 2.5 shows a comparison of both neutral and cationic spec-

¹<http://www.astrochem.org/pahdb/>

²<http://astrochemistry.ca.astro.it/database/>

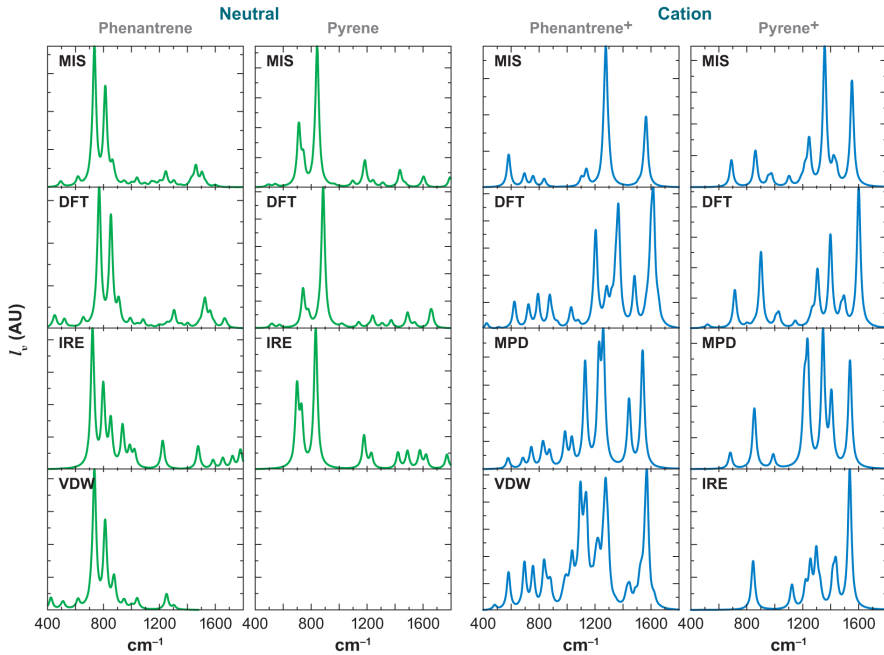


Figure 2.5: A comparison of both neutral and cationic spectra of phenanthrene and pyrene obtained by the different methods described: Matrix Isolation Spectroscopy (MIS), Density Functional Theory (DFT), Infrared Emission (IRE), Multiphoton Dissociation (MPD) and Van der Waal cluster (VDW – not described, see [16] for description). The spectra by the different techniques have some similarities but are not identical. The figure is from [16] and reprinted with permission from the publisher.

tra of phenanthrene and pyrene obtained by the different methods described above. The different techniques produce fairly similar results. However, a closer look at the spectra reveals positional shifts, broadenings, and intensity variations of the bands. A comparison between the results from cavity ring-down spectroscopy and MIS give matrix shifts of $\sim 3 \text{ cm}^{-1}$ and broadenings of up to 80% [72]. The intensity variation may originate from both matrix effects and, for the DFT results, from anharmonicity shifts. The same goes for the MPD data. A more detailed analysis of the shortcomings of the different techniques gives an overall confidence in the experimental and numerical results when comparing them to interstellar spectra.

CHAPTER 3

Theory and numerical methods

In the ISM, PAHs are exposed to strong radiation fields and collisions with all kinds of particles. In the following, the interaction between molecules and radiation will briefly be discussed as this is the basis of the experiments described later. Thereafter, a short introduction to the numerical method used to optimise the molecular structures and calculate the electronic transitions is given.

The Schrödinger equation (3.1) describes the quantum state of a system with the wave function, Ψ , in an energy field described by the Hamiltonian operator, \hat{H} .

$$i\hbar \frac{\partial}{\partial t} |\Psi(\vec{r}, t)\rangle = \hat{H} |\Psi(\vec{r}, t)\rangle, \quad (3.1)$$

where \hbar is the reduced Planck constant, and \vec{r} and t are the space and time coordinates. Solving this equation gives all the information on the system. The problem of finding the stationary states of a molecule reduces the Schrödinger equation to a time independent eigenvalue problem and this equation is given by

$$E|\Psi\rangle = \hat{H}|\Psi\rangle. \quad (3.2)$$

In order to obtain energies and structures of the excited states of a molecule, the time dependent and more troublesome version is needed.

As hydrogen is the only atom which can be treated analytically, it is clear that a number of approximations are necessary in order to

describe polyatomic molecules. The main simplification to the complicated many-particle Schrödinger equation is the Born-Oppenheimer approximation, where the electron motion is separated from the motion of the nuclei. This simplification is justified by the fact that electrons are approximately 2000 times lighter than the protons and neutrons making up the nuclei resulting in much shorter time scales for the electron motion. The electrons can therefore be regarded as moving around in an electric potential generated by the nuclei particles in fixed positions. This boils down to a total wave function of the molecule (3.3) given by the product of the electronic and nuclei wave functions, and the total energy (3.4) is given by the sum of the electronic and nuclei energy. The nuclei energy consists of contributions from both vibrations and rotations of the molecule [73]. The electronic part of the wave function is called the molecular orbital.

$$\Psi_{molecule} = \Psi_{electrons} \Psi_{nuclei} \quad (3.3)$$

$$E_{molecule} = E_{electronic} + E_{vibrations} + E_{rotations} \quad (3.4)$$

Photoexcitation and de-excitation channels

The huge difference in mass and the resulting difference in time scales of motion is also used to simplify the description of the photoexcitation process. When exciting the molecule electronically, the electron density is displaced – this is another way of saying that the electron goes from one molecular orbital to another.

In the Franck-Condon approximation, where the internuclear separation remains constant during the excitation, the transition moment of an electronic excitation is given by equation (3.5). Here, $M_{i \rightarrow f}$ is the transition moment and \hat{M} the transition operator. The transition moment includes higher order terms too, but the electric dipole moment is on the order of 10^5 and 10^7 times higher than the magnetic dipole and electric quadrupole moments, respectively. Hence, higher terms of the operator can usually be neglected.

$$M_{i \rightarrow f} = \langle \Psi_f | \hat{M} | \Psi_i \rangle \quad (3.5)$$

The electric dipole moment operator is given in equation (3.6) and depends on the coordinates of the electrons, r_i , and nuclei, R_j , as well as the nuclei charges, eZ_j .

$$\hat{M}_d = -e \sum_i r_i + e \sum_j Z_j R_j, \quad (3.6)$$

where e is the elementary charge.

When equation (3.6) is inserted into (3.5), the transition moment simplifies to equation (3.7), because the electronic states are orthonormal.

$$M_{d,i \rightarrow f} = -\langle \Psi_{N,f} | \Psi_{N,i} \rangle \langle \Psi_{e,f} | e \sum_i r_i | \Psi_{e,i} \rangle \quad (3.7)$$

$\langle \Psi_{N,f} | \Psi_{N,i} \rangle$ is called the Franck-Condon factor and describes the spatial overlap of the initial and final nuclei wave functions. In a large molecule with many vibrational modes, a large Franck-Condon overlap results in broadening of the absorption profile as many vibrational modes of the electronically excited molecule will be populated.

$\langle \Psi_{e,f} | e \sum_i r_i | \Psi_{e,i} \rangle$ is the electronic transition moment and is often referred to as the oscillator strength of the transition [73–75].

Besides the Franck-Condon overlap, the temperature can also broaden the absorption profile. For a molecule in thermal equilibrium, the population of an excited state is given by the Boltzmann distribution (3.8), where g_i is the degeneracy of the state and ΔE_i is the energy difference between the i 'th state and the ground state.

$$\frac{N_i}{N_0} = g_i \frac{\exp(\beta \Delta E_i)}{\sum_i \exp(\beta \Delta E_i)}, \quad (3.8)$$

where N_0 is the ground state population and β is given by $(k_B T)^{-1}$ (k_B being Boltzmann's constant).

After excitation from the electronic ground state to an electronically excited state, several de-excitation processes compete [27]. Figure 3.1 shows a diagram of the different processes. The coloured arrows indicate radiative transitions and the grey arrows the non-radiative. When absorbing a photon, the molecule is excited to a particular vibrational mode in the electronically excited state, but within picoseconds or faster, the vibrational energy is redistributed to all the vibrational modes available in the excited state – this is called intramolecular vibrational redistribution (IVR), and the molecule is still electronically excited after this process.

Several processes can bring the molecule into a lower lying electronic state. When internal conversion (IC) takes place, the electronic

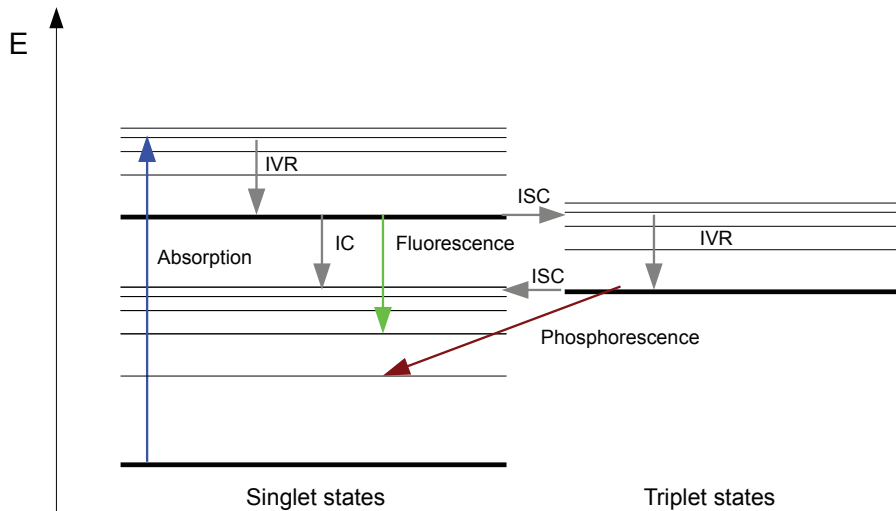


Figure 3.1: Jablonski diagram showing different competing deexcitation channels. The blue arrow indicates the initial excitation by photon absorption. The red and green arrows indicate the radiation emitting processes of fluorescence and phosphorescence, while the gray arrows indicate the non-radiative channels of intramolecular vibrational redistribution (IVR), internal conversion (IC), and intersystem crossing (ISC).

energy of the excited state is converted into vibrational energy in the ground state. The rate of IC depends on the specific molecular structure, overlap of nuclear wave functions, the electronic coupling between the states, and the energy gap. The time scale for IC is usually $10^{-5} - 10^{-8}$ s. This can, however, be as fast as subpicosecond if the potential energy surfaces of the electronically excited state, S_1 , and the ground state, S_0 , touch in a conical intersection at an accessible nuclear geometry.

Another possibility is transition to a different spin multiplicity state. This process is called intersystem crossing (ISC) and is normally a very slow channel on a time scale in the ms regime. However, if higher lying states are involved, e.g. if the photon energy is high, ISC can take place very rapidly.

After returning to the electronic ground state, e.g. through IC, the molecule can dissociate due to the increased internal energy. All of the processes mentioned above can lead to either dissociation (most probable after IC leaving the molecule highly vibrationally excited in the

electronic ground state) or radiative emission normally in the infrared region (corresponding to the energy of the vibrational modes).

3.1 Radiative lifetime

In order to determine whether dissociation after IC is a probable route or not, the radiative lifetime of the molecule is estimated by using the frequency and intensity of the vibrational modes. These quantities are obtained from quantum chemical calculations. The IR radiation rate can be estimated by considering Einsteins A coefficient (3.9), which gives the rate of spontaneous emission. Even for low energy modes, the spontaneous emission rate is higher than the stimulated, so this can be neglected in the estimation of the radiative lifetime of the molecule.

$$A = \frac{64\pi^4\nu^3}{3hc^3} |\langle 1 | \hat{M}_d | 0 \rangle|^2, \quad (3.9)$$

where ν is the vibration frequency of the specific mode, h is Planck's constant and c the speed of light. $|1\rangle$ is a vibrationally excited state and $|0\rangle$ a lower lying state. By Taylor expanding the dipole moment operator to second order, and evaluating from $|1\rangle$ to $|0\rangle$, only the linear displacement plays a role in form of a displacement operator. Assuming that the vibrational modes behave like harmonic oscillators, allows the displacement operator to be expressed by the step up and down operators. The A coefficient can be re-written as the product of a constant, the wavenumber squared, and the IR intensity, see equation (3.10). The wavenumbers of the vibrational modes, $\tilde{\nu}[\text{cm}^{-1}]$, and their corresponding IR intensities, $IR_G[\text{km/mole}]$, can be found from numerical calculations (see section 3.2).

$$A = 1.25 \cdot 10^{-7} (s^{-1}) (\tilde{\nu}[\text{cm}^{-1}])^2 IR_G[\text{km/mole}] \quad (3.10)$$

Each specific vibrational mode has its own radiative lifetime. The larger the frequency or intensity, the shorter the lifetime. The mode dominating the time scale of the radiative lifetime is not surprisingly the most active mode. Normally, the radiative lifetime is in the millisecond range.

3.2 Density functional theory

As mentioned above, the exact energy of a time independent system is found by solving the time independent Schrödinger equation. Solving this equation for many body systems such as molecules with more than two electrons, becomes impossible without further simplifications and approximations. One way to make the problem less complicated is to consider the electron density, $\rho(\vec{r})$, which depends only on one set of coordinates instead of the electronic wave function which depends on the coordinates of all the individual electrons. The energy then becomes a function of a function, a functional, hence the name of the method: Density Functional Theory (DFT).

3.2.1 Time independent DFT

DFT relies on two fundamental theorems shown by P. Hohenberg and W. Kohn in 1964 [76]. These state that the energy can be found from the density, and that the exact density is found by minimising the energy. Unfortunately, only the nuclei-electron attraction and nuclei-nuclei and electron-electron repulsion can be found from the density, whereas the kinetic and exchange energies cannot. This means that the exact energy cannot be found from a single Slater determinant¹, and to reduce the computational costs, approximate expressions must be used.

The most common version of DFT is called the Kohn-Sham method. Here, the electrons are considered as non-interacting particles, which move in an effective potential caused by the electron density. The interaction is then instead placed in the so-called exchange-correlation function. The energy in a system ($E(\rho)$) is found as the sum of the kinetic energy of the non-interacting electrons (a single Slater determinant) ($E_{kin,S}(\rho)$), the potential energy of the electron-nuclei attraction ($E_{ne}(\rho)$), the Coulomb energy of the electron-electron repulsion ($E_C(\rho)$), and the exchange-correlation energy ($E_{XC}(\rho)$) (3.11).

$$E(\rho) = E_{kin,S} + E_{ne}(\rho) + E_C(\rho) + E_{XC}(\rho) \quad (3.11)$$

The exchange-correlation energy contains two terms: the exchange energy which describes the Pauli exclusion principle of not allowing

¹Expression for the wave function of a system containing more than one electron that satisfies the Pauli exclusion principle for spin half particles.

two identical electrons to be in the same spin state, and the correlation energy that includes the Coulomb repulsion of the electrons. As mentioned, the density can be found by minimising the energy, so the DFT energy must be minimised by varying the orbitals, ϕ_i , from which the density is found. These orbitals are linear combinations of atomic one-particle wave functions, χ_j , where the expansion coefficients, C_{ij} , are found iteratively. From this, the Kohn-Sham and overlap matrices are constructed. The Kohn-Sham matrix is diagonalised and the expansion coefficients and energies are found by solving the eigenvalue problem. This is called the self-consistent field method (SCF).

Functional

If the correct exchange-correlation functional is used, the exact energy can be found [76]. In order to get the best results at the lowest computational cost, the functional must be chosen carefully. One of the most common exchange-correlation functionals is the BLYP (Becke-Lee-Yang-Parr). Here, the exchange functional proposed by Becke is a sum of a simple functional, where the electron density is uniform, and a more complicated functional, where the spatial variations of the density is taken into account. The correlation functional is based on calculations performed for helium. By combining the DFT-Becke functional with a Hartree-Fock exchange functional (based on single Slater determinants), a hybrid functional is obtained. The most commonly used exchange-correlation functional in computational chemistry is the hybrid functional B3LYP [77, 78].

Choice of basis set

Different functions can be used as atomic orbitals when calculating the density. The size of the basis set is chosen as a compromise between accuracy and acceptable calculation time. In this work, 6-31+G(d,p) has been used for the larger PAHs and 6-311+G(d,p) for the smaller. The numbers indicate the number of atomic orbitals in the basis set for the 1s-, 2s- and 2p-orbitals. The "+" gives a diffuse set of s- and p-orbitals to all atoms except hydrogen and is especially used for anions. G is for Gaussian. (d,p) adds a d-orbital to all atoms except hydrogen and a p-orbital to hydrogen. These are very common choices of basis sets for PAHs [65–70].

Gaussian

For the results presented in this thesis, the commercial program Gaussian03 [79] has been used. This program was written by John Pople and co-workers in 1970 and has been updated since (the most recent version is Gaussian09). In the Gaussian package, the atomic orbitals are mimicked by Gauss functions (hence the name) to speed up the calculation time. The shape of the orbitals is given by equation (3.12), where c is the normalisation factor, $\vec{r} = (x, y, z)$ the space coordinate, n , m , and l are integers and α gives the radial extent of the given orbital [80]. The right values of n , m , and l give orbitals that mimic the needed s -, p -, and d - orbitals.

$$g(\alpha, \vec{r}) = c \cdot x^n \cdot y^m \cdot z^l \cdot e^{-\alpha r^2} \quad (3.12)$$

Gaussian can perform both semi-empirical and ab initio quantum chemical calculations such as Hartree-Fock, DFT, coupled cluster, and Møller-Plesset. In the computational work done for this thesis, mainly structure optimisation of ground state and transition state geometries, determination of vibrational frequencies, and calculations of excited state energies have been performed. However, the program is capable of providing all desired information for a specific system. Of course the program – as well as the method – has some draw-backs and limitations that will be discussed in section 3.2.3.

3.2.2 Time dependent DFT

Time independent DFT can only be used to obtain information of the molecule in its ground state. If excitation energies or other information of the excited states are needed it is necessary to use time dependent DFT (TD-DFT) where the time dependent Schrödinger equation (3.13) is solved.

$$i \frac{\partial \phi(t)}{\partial t} = \hat{H}(t)\phi(t) \quad (3.13)$$

The Hamilton operator is time dependent due to the presence of a time dependent field, e.g. electric and/or magnetic. The electron density is now both dependent on space and time. The main difference between DFT and TD-DFT is the existence of a minimum for the

DFT energy. TD-DFT builds on the Runge-Gross theorems, which correspond to the Kohenberg-Kohn theorems in DFT. These state that the exact time dependent density can be found from a so-called action functional which has a stationary point instead of a minimum. It can be shown that the time dependent version of the Kohn-Sham equation is given by (3.14) where $V_s(\rho(\vec{r}, t))$ is the effective potential, which, as indicated, depends on the electron density itself. Again, this equation is solved iteratively until the desired convergence criterion is met [81, 82].

$$\left[-\frac{1}{2} \nabla^2 + V_s(\rho(\vec{r}, t)) \right] \phi_i(t) = i \frac{\partial}{\partial t} \phi_i(t) \quad (3.14)$$

3.2.3 Errors and limitations

To estimate the error of the DFT or TD-DFT calculations it is necessary to compare the results with results from either experiments or other, more accurate computational methods. When comparing the calculated vibrational frequencies with experimentally obtained frequencies, the DFT frequencies tend to be a little too high. National Institute of Standards and Technology (NIST) gives scaling factors for different exchange-correlation functionals and basis sets [83], these are typically ~ 0.965 for the functional and basis sets chosen in this thesis. Bond lengths are subject to errors of typically less than 1 pm. Errors in TD-DFT calculations stem both from the method itself and from the errors of the optimised structure used in the calculation. In the literature, the error in the energy is typically around 0.1 – 0.2 eV depending on the basis set and exchange-correlation functional.

A. J. Cohen *et al.*[84] give an overview of the major failures in DFT calculations and their origin. Barriers of chemical reactions, energetic band gap of materials, dissociation energies of molecular ions, and energies of excitations with charge transfer character are all underestimated, while binding energies of charge transfer complexes and the response to an electric field in molecules and materials are overestimated. These deviations are caused by the delocalisation error of approximate functionals, which spread out the electron density not taking the discrete nature of the electrons properly into account. This problem can be thought of as fractioning of charges. DFT also fails to describe degenerate and near-degenerate states as in transition metals, when breaking chemical bonds and in strongly correlated materials. Here, the problem

is not fractional charges, but fractional spins. All the problems point toward the approximate functional, and the solution to the problems lie in the development of a functional that properly takes the physical nature of the electrons into account.

CHAPTER 4

Experimental techniques

As mentioned, gas phase experiments are essential in the field of experimental astrophysics in order to mimic the conditions of low densities in the interstellar medium. This type of experiments are also used to investigate physical and chemical properties of molecules and ions not related to astrophysics. Many different fields within physics and chemistry also benefit from the possibility of studying a molecule or ion without external interactions. Another advantage is the possibility to explicitly choose the interaction one wants to investigate: cluster experiments, microsolvation, effects of hydrogen bonding, etc. Compared to liquid phase experiments, a large setup is often required to overcome the difficulties of gas phase experiments. Many gas phase experiments are performed on ions, as the charge provides a very useful handle to guide the ions through the experiment using electrostatic or magnetic fields.

The setup used for the work of this thesis, ELISA, is primarily used to investigate the interaction between ions and photons. In solution phase, the law of Lambert-Beer is applied to obtain the absorption cross section for analyte molecules or ions. Here, the light intensity depletion caused by the photon absorption by the molecules is measured and directly converted into an absorption cross section. When performing gas phase experiments, the number of ions is often so small that a depletion of the laser pulse cannot be monitored. The number of ions is typically a factor of 10^{10} smaller than the number of photons in a 1 mJ laser pulse when using the electrospray ion source (see section 4.1). Instead, the action of molecule neutralisation upon photoexcitation is measured. The

use of a pulsed laser in combination with a storage ring also makes it possible to investigate the lifetime of an excited ion.

In the following, first the ionisation methods are described. Second, the setup of ELISA, the concept of action spectroscopy, and the analysis of the obtained data are explained – hopefully spreading light on the scientific possibilities of this great machine.

4.1 Ion sources

Bringing the ions into gas phase is the first hurdle of the experiment. Many different types of ion sources can be used depending on the ions one wants to produce. Two different types of ion sources have been used for the work of this thesis and production of PAH ions: The electrospray ionisation source, and the Nielsen plasma ion source. The ionisation process in these sources is a soft and hard ionisation method, respectively. In the following, the designs and ionisation processes for both types of sources are described.

Electrospray ion source

The electrospray ion source was developed by the Nobel Prize winner in chemistry of 2002, J. Fenn [85], and a schematic drawing is shown in figure 4.1. In this kind of ion source, the neutral molecules are dissolved or diluted in a solvent (e.g. water, methanol, ethanol, or mixtures of these) and are present as ions in the solution. By adding a base or acid, the degree of protonation or deprotonation can be enhanced, and more ions can be brought into gas phase. The solution is transported to the tip of a needle by a thin capillary attached to a syringe placed on a syringe pump. This controls the flow rate and ensures a steady flow of solution from the syringe to the needle tip. At the tip, charged droplets are formed and sprayed – forming a Taylor cone – towards the opening of the low pressure region by applying a voltage of 2 – 4 kV between the needle and the opening. In the heated capillary (typically between 25 – 140°C) placed just after the opening, the solvent molecules are evaporated. The charged droplets undergo Coulomb explosion as the repulsive force between particles with the same charge sign overcome the surface tension of the droplet. The process of electrospray ionisation is not completely understood, and especially the needle voltage plays a crucial role in the production of the ions. During

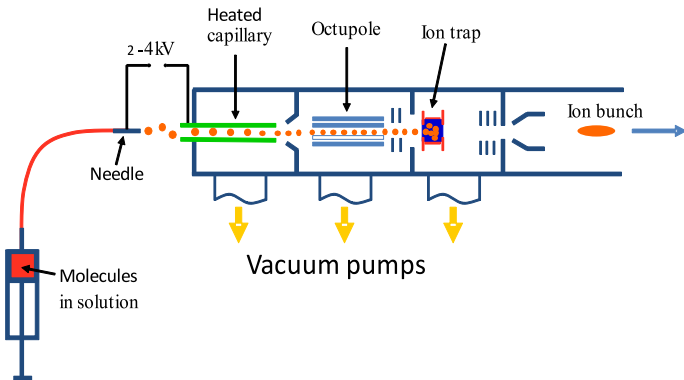


Figure 4.1: A schematic drawing of the electrospray ionisation source used to produce both protonated and radical cationic PAHs.

my time in the laboratory, it was observed that the ratio of produced radical cations to protonated cations is very dependent on the needle voltage.

A tube lens, a skimmer, an octupole, and another set of lenses guide the ions into a RF-trap, where they are collected and extracted in bunches. This step increases the ion density and thereby enables lifetime measurements. The trap is a multipole trap consisting of 14 circular electrodes arranged as a cylinder with a diameter of 5 cm. The ions are collisionally cooled and slowed down by a helium buffer gas let into the trapping region. The bunches are created by switching the exit electrodes for typically 30 μ s, and they consist of $\sim 10^5$ ions. The internal energy of the ions can be lowered by cooling the trap with liquid nitrogen down to 150 K. The molecules are not exposed to sufficient energy exchange to cause fragmentation, or change conformation or configuration of the rigid PAHs during ionisation by this soft ionisation method.

Because of the preparation method of the ions in solution, this type of ion source is suitable for production of protonated or deprotonated ions. It is hard to produce molecular radical cations and anions as it requires either an electron acceptor with high electron affinity or an electron donor where the electron affinity of the molecule must be higher

than that of the donor. It is, however, possible when adding e.g. silver nitrate to the solution. If the silver ions have an ionisation energy higher than that of the analyte molecules, electron exchange can take place resulting in radical cations of the analyte molecule. This technique has been used to produce radical cations of pyrene [86, 87], anthracene [88], and in this work to produce radical cations of commercially produced hydrogenated PAHs. The ionisation process is explained in depth in section 6.3.1. The purity of the sample must be taken into account when analysing the outcome of the ion source. M. Vala *et al.* [89] showed that with a sample of commercial pyrene with a purity of 98%, the product with highest abundance of electrospray ionisation of the sample was the protonated species of the impurity nitrogen substituted pyrene (1-azapyreneH^+ , mass 204). The protonated pyrene abundance is only 3% of the 1-azapyreneH^+ abundance.

Nielsen plasma source

The Nielsen ion source is a plasma ion source developed by K. O. Nielsen in the 1950's [90]. Figure 4.2 shows a schematic drawing of the region where the ions are formed. A plasma is created by electrons evaporated from a tungsten filament and gas consisting of atoms and molecules let in through a needle valve. A solid sample of the desired molecules is loaded into an oven, from which molecules are evaporated into the plasma. In order to create the plasma, an electric current is applied and increased until a spark initiates an ionisation cascade where collisions between electrons and neutral molecules and atoms induce further ionisation of the gas. Ions can be extracted from the plasma by applying an appropriate voltage to the housing of the ion source. In the ion source, a magnetic field is applied parallel to the symmetry axis of the ion source making the charged particles circle to enhance the number of collisions without affecting the motion parallel to the symmetry axis.

The ion source was invented for production of cations but has been used to produce anions as well. Here, the production relies on a relatively high electron affinity of the species in question. The Nielsen source has successively been used in the production of e.g. C_{60} anions which has an electron affinity of ~ 2.5 eV. In figure 4.2, the setup for production of cations is shown. In the case of production of anions, the anode is grounded instead of the filament.

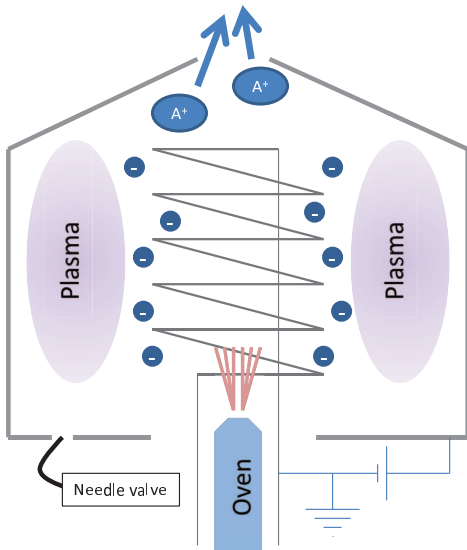


Figure 4.2: A schematic drawing of the Nielsen plasma source used for production of PAH cations.

The conditions in the plasma are very harsh with 100 – 200 eV electrons, and even multiply charged noble gas cations can be produced in this source. The bombardment of electrons leads to a broad temperature distribution which has been shown to extend up to 3000 K for fullerene cations produced in the source [91]. Most ions are expected to have a temperature of about 800 – 1000 K.

4.2 ELISA

ELISA (ELECTROSTATIC Ion Storage ring, Aarhus) is an electrostatic ring, which can store relatively large ions compared to storage rings based on magnetic deflectors. This enables experiments on e.g. large biomolecules and PAHs. The ring has been described in details by S. P. Møller [92–95] and L. H. Andersen *et al.* [96], and a schematic drawing of the ring is shown in figure 4.3.

An ion source is placed on a high voltage platform and the ions are accelerated to 22 kV. Usually, an ion trap is used to collect the ions in bunches of $\sim 30 \mu\text{s}$ which are extracted at a rate of 10 or 20 Hz (normally 10 Hz). If no trap is available, an electrostatic chopper can be used

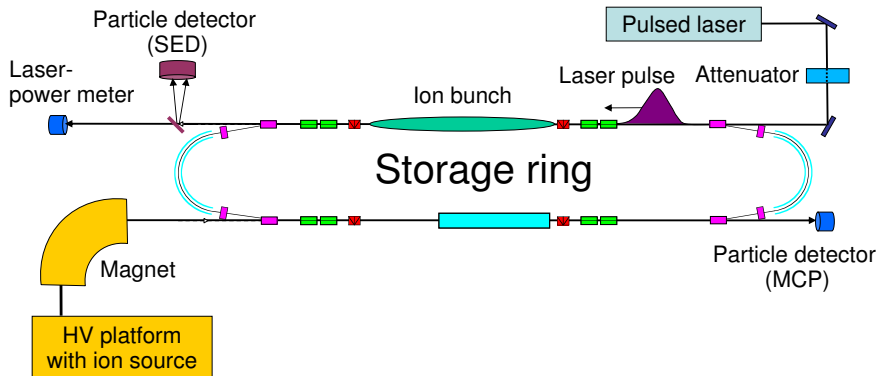


Figure 4.3: The EElectrostatic Ion Storage ring, Aarhus – ELISA.

instead. An extraction lens, and electrostatic steering and quadrupole focusing elements (not shown in figure 4.3) are placed in the injection beam line letting the operator optimise the beam before injection into the storage ring. In the injection beam line, a 90° bending magnet is used to select the ions with the desired m/q -ratio. The injection beam line is differentially pumped by turbo pumps, and the pressure just before the ring entrance is in the order of 10^{-9} mbar.

The storage ring consists of two straight segments connected by two sets of two 10° and one 160° deflectors and has a circumference of 7.62 m. Steering and focusing elements are placed in the straight segments, which will be referred to as the injection section (bottom) and interaction section (top). The 10° deflectors serve several purposes. A design using two 180° deflectors showed not to be stable, and one of the 10° deflectors works as the main entrance for injection of the ion bunches. They also allow for detection of neutrals created in the straight sections giving an indication of both the number of ions in the bunch and the pressure in the ring. Furthermore, this setup allows for dumping the stored ions on one of the detectors – a particularly useful option during daughter mass analysis of the photofragments (see section 4.2.1). The 160° deflectors are cylindrical instead of spherical which improves the lifetime of especially high intensity beams. After optimisation, the settings can be used for all ions as the deflection is only dependent on the energy and not the mass of the ions when using electrostatic deflectors. This is easily shown by comparing the force on a particle in a static

electric field and the centripetal force.

The storage time of the ions can be up to seconds because of the very low pressure attained with the diffusion pumps ($\sim 10^{-11}$ mbar). Normally, the ions are stored for about 100 ms (corresponding to an injection rate of 10 Hz), but lifetimes up to 30 s have been observed. The revolution time of the ions depends on their mass and is $\sim 60\ \mu\text{s}$ for the larger biomolecules and PAHs normally studied, but only $3.5\ \mu\text{s}$ for protons. The ion bunch of the larger molecules is spatially extended up to half of the storage ring.

Laser system

A tuneable EKSPLA Nd:YAG laser (NY342/C/3/UVE) is placed so that interaction between ions and photons takes place at the straight segment opposite the injection – both longitudinal (laser beam parallel to the ion beam) and transverse (laser beam vertically crossing the ion beam) interaction with the ion bunch is possible. The 3rd harmonic (355 nm) of the Nd:YAG laser is split into two beams, the signal and idler, in an Optical Parametric Oscillator (OPO) to produce photons with wavelengths in the region 420 – 710 nm (the signal) and 710 – 2300 nm (the idler). Another set of non-linear crystals are used to produce 210 – 419 nm UV photons by frequency doubling of either the signal or the idler. The pulses are 3 ns long and have an energy ranging from below 1 mJ (some UV and IR regions) to a few tens of mJ (strongest in the visible region). An attenuator may be used to control the energy of the pulses before they enter the interaction region. The energy of the laser pulse is measured by a power meter placed at the end of the interaction segment.

4.2.1 Data collection and analysis

At the end of the two straight segments, detectors are placed for measuring the number of neutral fragments created by either collisions with the residual gas or by laser interaction as a function of time. A standard Micro Channel Plate detector (MCP) is positioned at the end of the injection section along with a phosphor screen which allows for an easy way to optimise the beam quality before and during experiments.

A Secondary Electron Detector (SED) is placed at the end of the interaction section and a schematic drawing of its design is found in fig-

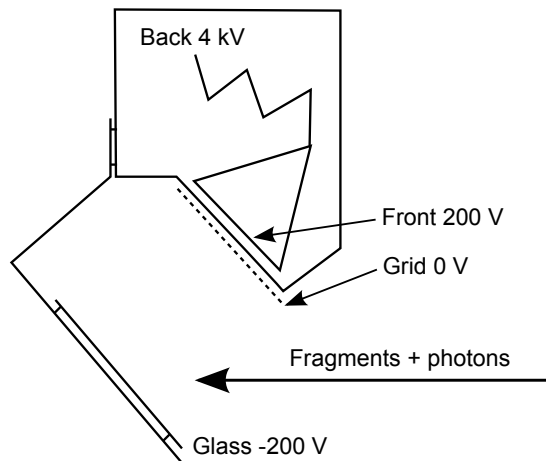


Figure 4.4: Schematic drawing of the secondary electron detector, SED, used to monitor the neutral fragments produced at the interaction section of ELISA. Figure from [97] and reproduced with permission of the author.

ure 4.4. The SED consists of a glass plate (so that the laser pulse is transmitted without reduction of the energy) coated with a layer of tin doped indium oxide. When particles hit the glass plate, secondary electrons are produced. In order to accelerate these towards the standard channeltron detector above, the glass plate is negatively biased. When the electrons enter the channeltron after passing through the grounded grid, a chain reaction of electron production takes place resulting in a detectable signal at the end of the channeltron. The design of this detector allows for monitoring of the laser pulse energy in the visible region, as the absorption of the coated glass plate is negligible. Below 350 nm and at very high laser pulse energies the coating is damaged, and hence, the detector is not used under such circumstances.

Action absorption spectroscopy

In order to identify the PAHs as components of the interstellar medium, it is necessary to have laboratory absorption spectra to compare with the spectra of stars lying behind interstellar clouds. As previously mentioned, absorption spectra are usually measured as the difference between incoming and transmitted light of a given sample according to Lambert-Beers law. This kind of measurement is fairly easy to do for solution phase samples. However, for species in gas phase, the decrease

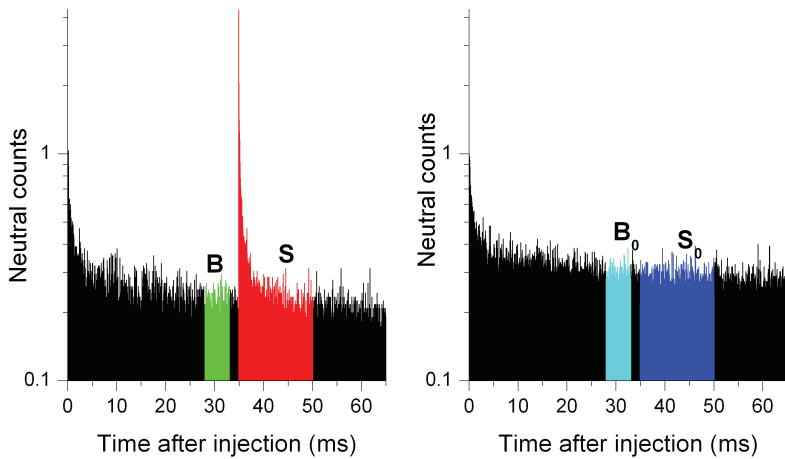


Figure 4.5: Illustration of the applied technique of action absorption spectroscopy. The figure shows recording of neutral fragments produced in the storage ring as a function of time. The right and left panels show a measurement of neutrals produced for 65 ms after injections of ions with (left) and without (right) laser excitation of the ions at 35 ms after injection. In the figure is indicated *green and cyan*: background window B and B₀ and *red and blue*: signal window S and S₀

in the transmitted light is not measurable due to the low density of molecules compared to photons. Action spectroscopy is a useful tool to overcome this problem. The ions are electronically excited, and the process of IVR followed by IC leaves the ions in a vibrationally hot ground state. This may lead to dissociation of the ion – this being the *action* of the experiment. The dissociation cross section depends on the excitation energy (wavelength of the laser). By scanning the energy (done by scanning the wavelength of the tuneable laser) and measuring the number of neutral fragments (action) produced, photodissociation spectra or action absorption spectra can be created, giving a measure for the real absorption spectra. Figure 4.5 shows a measurement at a single wavelength and illustrates the principle of the technique. The action of the experiment is indicated by red.

The absorption cross section is proportional to the number of neutral fragments caused by the photoexcitation and inversely proportional to the number of ions and number of photons:

$$\sigma_{\lambda}^0 \propto \frac{N_{0,\lambda}}{N_{\lambda} N_I}, \quad (4.1)$$

where $N_{0,\lambda}$ is the number of neutral fragments generated in the interaction, N_λ the number of photons, and N_I the number of ions in the ion bunch. The number of photons can be estimated from $E_\lambda \lambda$ (the laser pulse energy and wavelength), and the number of ions is proportional to the integrated background B (green in figure 4.5). The number of laser induced neutrals can be found by subtracting neutrals created by residual gas collisions, see equation (4.2), where S , S_0 and B_0 are shown in figure 4.5.

$$N_{0,\lambda} = S - \frac{B}{B_0} S_0 \quad (4.2)$$

When assuming a linear dependency between the number of neutrals created and the number of photons, the cross section can be found by (4.3). It is necessary to perform scans of the laser pulse energy in order to verify that these are in fact one photon processes.

$$\sigma(\lambda) \propto \frac{S - \frac{B}{B_0} S_0}{B} \frac{1}{E_{laser} \lambda} \quad (4.3)$$

The order of absorption

In the previous section, it was assumed that absorption by a single photon is adequate to cause dissociation. Some ions may require a higher number of absorbed photons to dissociate, due to a difference in dissociation barriers and order of the electronic transitions. The time scale for non-radiative conversion of electronic energy into the vibrational modes (internal conversion) is expected to be picoseconds. As the laser pulse duration is on the nanosecond time scale, it is possible for ions to absorb more than one photon during the passage of the laser pulse – referred to as multiphoton absorption in the following. The actual number of photons needed to result in dissociation is determined by monitoring the number of neutrals generated at a certain wavelength (often at an absorption maximum) as a function of laser pulse energy. This energy can be varied by attenuating the laser beam with filters.

The number of absorbed photons can be found by fitting the data to a Poisson distribution, equation (4.4), of different orders [96, 98], n . Poisson statistics apply when an event can happen independently of any previous events. Conversion of the electronic excitation energy to

vibrational energy in the ground state is very fast, thus absorption of several photons is possible within the interaction time.

$$f(n) \propto \frac{\nu^n \cdot e^{-\nu}}{n!} \quad (4.4)$$

In equation (4.4), ν is the average number of photons absorbed during the interaction time $[0, \tau]$ and is given by

$$\nu = \sigma_{abs} \frac{\epsilon}{\hbar\omega} / A_L, \quad (4.5)$$

where σ_{abs} is the absorption cross section area, ϵ the laser pulse energy, $\hbar\omega$ the energy of a single photon, and A_L the overlap area.

Saturation effects are important in order to determine the correct absorption order. The correct assignment of the absorption order must include careful measurements at low laser pulse energies to avoid saturations effects.

Lifetime analysis

One of the advantages of storage rings is the ability to measuring the dissociation lifetime of the excited ion. As can be seen in figure 4.5, the decay of the excited ions can extend over several milliseconds. Some decays occur on a time scale that is smaller than the revolution time, which we refer to as prompt decay. Neutrals created under these circumstances are only detected by the SED-detector, and lifetimes below a lower limit of $\sim 10 - 15 \mu s$ cannot be determined.

As mentioned in chapter 3, intersystem crossing may lead to trapping in a triplet state. In this case, two lifetime components can be seen in the lifetime spectrum. If several dissociation channels are present they all sum up to give a single combined lifetime. Assuming a simple Arrhenius decay, the decay rate, k , is given by (4.6), where A is the pre-exponential factor, E_a the activation energy, k_B Boltzmanns constant, and T the temperature of the molecule.

$$k = A \exp \left(-\frac{E_a}{k_B T} \right) \quad (4.6)$$

There is a spread in the energy of the ions, when they are created. This needs to be taken into account when simulating the lifetime. The

ions are considered as a number of microcanonical ensembles (thermodynamically isolated systems with fixed energy) with an energy distribution, $G(E)$, which can be approximated by e.g. a Gaussian function. The decay rate then becomes a function of the energy of the ions, as the temperature T can be set to the microcanonical temperature, T_m . The microcanonical temperature used in the rate constant have been shown by J. U. Andersen *et al.* [99] to match the average of the initial temperature and the temperature upon photoexcitation to first order. However, it should be noted that this deviation holds only when the assumption of equal level densities for the parent and daughter molecule is true. In the case of photodissociation, this is clearly not the case, and the error introduced by this simplification should be kept in mind. However, in the case of thermionic emission (not discussed in this thesis) the assumption is fairly good.

The number of neutrals created as a function of time is, taking these considerations into account, given by equation (4.7).

$$N_{\text{neutrals}}(t) = N_0 \int_{-\infty}^{\infty} G(E) k(E) \exp(-k(E)t) dE \quad (4.7)$$

In this expression, there are several unknown factors. The decay rate is the desired unknown, but this depends on the pre-exponential factor, the activation energy, and the initial temperature of the ions which are all unknown. The spread of the internal energy distribution can be found from the initial temperature and the heat capacity of the molecules found from their vibrational modes. Thus, in order to get the correct factors, measurements at several wavelengths are necessary.

Daughter mass analysis

Mass spectra of the charged photofragments can be obtained at ELISA. The charged daughter fragments created as a result of photoexcitation can be stored by switching the voltages of the electrostatic deflectors. The kinetic energy of the parent molecule is split between the fragments generated after dissociation proportionally to the mass of the fragments. As the voltages required for storing the ions depend on the kinetic energy of the ions, it is, with the right voltage, possible to store ions with a smaller energy and thereby smaller mass than the parent molecule and not lose them as in normal operation mode. Figure 4.6 shows the concept of voltage switching.

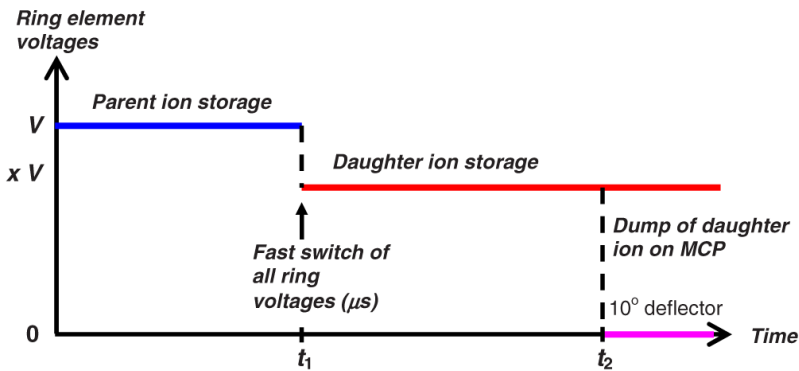


Figure 4.6: Illustration of the deflector voltages at different times which allows initial storage of the parent ions and subsequently the daughter fragments. Reprinted with permission from [100]. Copyright 2008, American Institute of Physics.

The switching time can be varied allowing for storage of fragments created at different times after photoexcitation. The time is limited by collisions with the residual gas. Hence, time resolved daughter mass spectrometry can be performed at the microsecond time scale. After switching, the stored daughter ions are dumped on the MCP detector. Figure 4.7 illustrates this concept. At all times, the parent molecule is still stored in the ring, but at switching times t_{1A} and t_{1B} the open dissociation channels are different and different daughter masses appear in the mass spectrum. The yield ratio of the daughter masses may also change as a function of time, allowing for estimates of the lifetimes of the fragments. These may be formed in a highly vibrationally excited state, which again can lead to further dissociation.

The resolution of this technique is very low ($\Delta m/m \approx \frac{1}{100}$) due to the high energy acceptance of the ring and the large detection area of the MCP detector. Though, for simple mass spectra and with some knowledge about the molecule, it is a useful tool. For more details see [100].

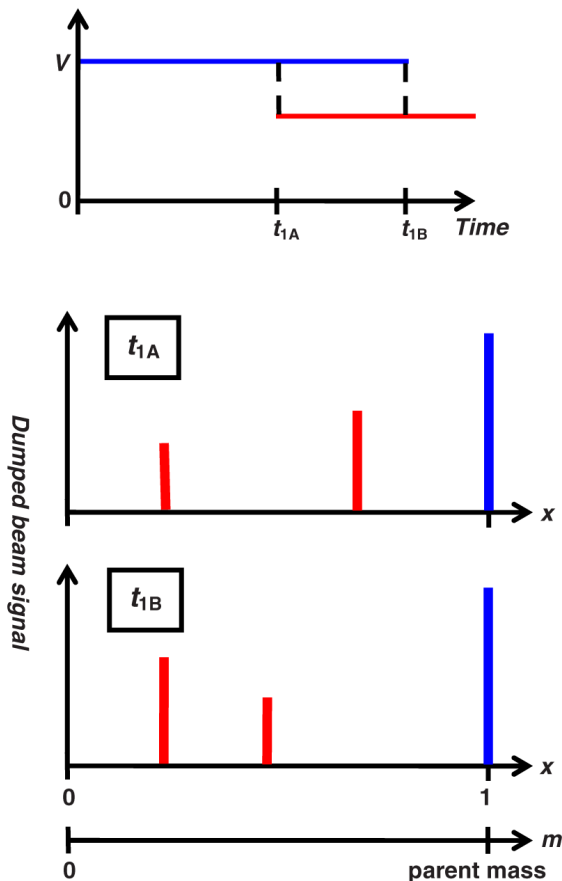


Figure 4.7: Different dissociation channels can open as a function of time and result in different mass spectra. The top graph illustrates two possible switching times. The two bottom graphs show mass spectra obtained at these two switching times. Reprinted with permission from [100]. Copyright 2008, American Institute of Physics.

CHAPTER 5

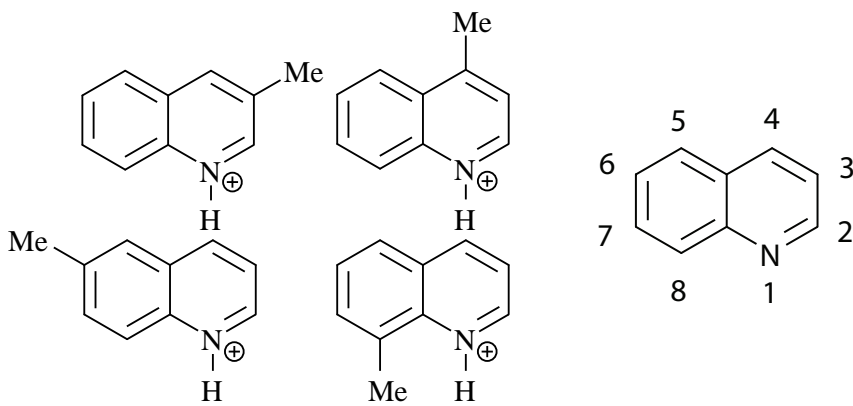
Methyl substituted quinoline

As mentioned in chapter 2, most of the AIR features are reproduced in laboratory spectroscopic studies of PAH cations [16]. But the 6.2 μm band appears at a shorter wavelength than expected. In order to explain the shift of the 6.2 μm UIR band, nitrogen containing PAHs (PANHs) have been studied both experimentally and theoretically [101–105] and through astronomical observations [106, 107] as nitrogen is the fourth most abundant molecule found in the interstellar medium. N and CH are isoelectronic and therefore substitution of a CH group with a nitrogen atom does not alter the conjugation of the molecule and facilitates protonation of the molecule. Their higher permanent dipole moment compared to PAHs make them an interesting class of molecules, as they can be detected in the microwave range. This can ease the identification of specific types or classes of PAHs in the interstellar medium.

The interstellar medium is not the only environment where PANHs are believed to play an important role since they have also been found in meteorites [108, 109] and in the atmosphere of the moon Titan [110]. As PAHs form by aromatic ring formation, the substitution of carbon and nitrogen can occur by gas phase reactions with nitrogen containing molecules, e.g. HCN. These reactions result in PANHs. PANHs are important in a biological sense as they act as precursors of biogenic material.

Here, the photostability of four gas phase methyl substituted quinolines are studied in their protonated form ($\text{CH}_3-\text{C}_9\text{H}_7\text{NH}^+$), namely protonated 3-methylquinoline (3-MeQ), 4-methylquinoline (4-MeQ), 6-

methylquinoline (6-MeQ), and 8-methylquinoline (8-MeQ) (figure 5.1a). These are chosen to investigate the effect of a methyl side group on the conjugation of the heterocycle (N containing) ring and the homocyclic ring. Methyl substituted PAHs have previously been investigated [3, 62, 111–115], and here methyl substituted PANHs are studied for the first time. The results are published in *Astronomy & Astrophysics* [1].



(a) The molecules chosen for the study of the effect of a methyl side group on the conjugation of the heterocycle (N containing) ring and the homocycle.

(b) The numeration of the skeleton atoms of quinoline used in the naming of the isomers.

Figure 5.1: Isomers of methyl substituted quinoline.

5.1 Experimental and numerical details

The experimental work was performed at ELISA. The protonated MeQs (commercial from Sigma Aldrich, purity > 97%) dissolved in a MeOH and acetic acid solution were brought into gas phase by the electrospray ionisation source and accumulated for 100 ms, before injection into the storage ring. After 35 ms of storage, the ion bunch was irradiated with photons in the region of 215 – 338 nm.

The experimental results were compared to DFT and TD-DFT calculations using the B3LYP level of theory and the 6-311+G(d,p) basis set. All normal mode frequencies were checked and found positive, and

zero point corrections and scaling of the vibrational frequencies were taken into account.

5.2 Results

Numerical results

Table 5.1 lists the order of the ground state energies calculated for the different methyl substituted quinoline isomers. As can be seen, the substitution is next to the nitrogen atom for the most stable isomer. Unfortunately, experiments were not performed on this isomer due to problems with the delivery of the sample. Numerical results for excitation and dissociation energies are described in the following sections.

Position of methyl group	Energy (eV)
2	0
4	0.09
7	0.12
6	0.15
3	0.16
8	0.18
5	0.20

Table 5.1: Order of calculated ground state energies of methyl substituted quinoline. The energies are given relative to the lowest energy isomer of 2-MeQ.

Action spectra

Figure 5.2 shows the action spectra of the four protonated methyl substituted quinolines recorded in vacuum. The upper two panels show the spectra of 6-MeQ and 8-MeQ where the methyl group is placed on the ring not containing nitrogen. The lower panels show 4-MeQ and 3-MeQ where the methyl group is placed on the ring with nitrogen. The absorption maximum of 6-MeQ and 8-MeQ is at 238 nm (5.21 eV), while for 3-MeQ and 4-MeQ it is at 232 nm (5.35 eV). The absorption is hence shifted 0.14 eV by moving the methyl group from the ring not

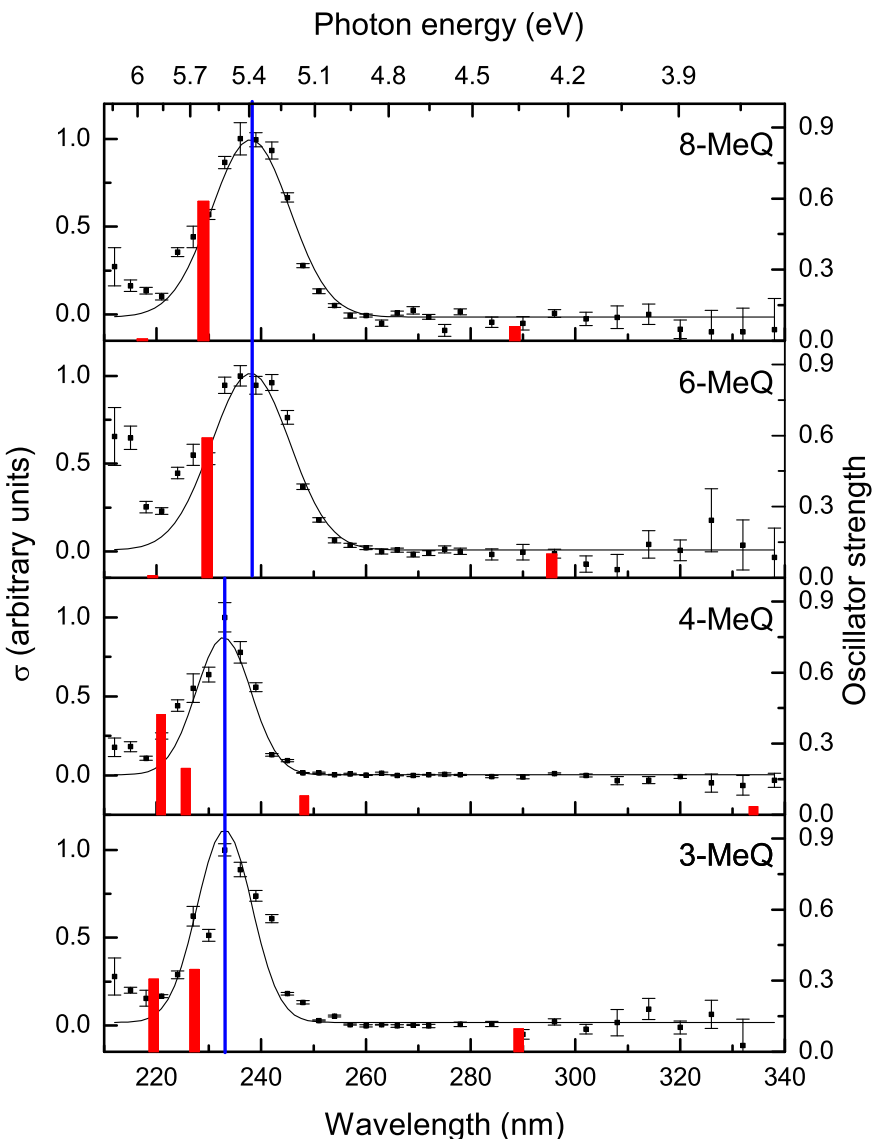


Figure 5.2: Measured action spectra (black squares) of the four methyl substituted qui-nolines and the calculated electronic transition and their oscillator strengths (red bars). Gaussian profiles (black curves) with centres at 232 nm (3-MeQ and 4-MeQ) and 238 nm (6-MeQ and 8-MeQ) and widths of 10.5 nm and 15 nm respectively, have been plotted together with the absorption profiles to indicate the spectral differences. It is clearly seen that the absorption profiles depend on the position of the methyl group.

containing nitrogen to the ring with nitrogen. Note that in addition to the spectral shift, the absorption is narrower for 3-MeQ and 4-MeQ.

The absorption maximum represents the energy of maximum overlap between the wave functions of the electronic ground state and the excited state. This means that the vertical excitation energy probably lies in the red part of the absorption peak. However, the exact determination of the vertical excitation energy is difficult as the initial vibrational excitation of the ion is not known. As mentioned above, the energy distribution of the ions plays a crucial role in the broadening of the absorption peak.

Figure 5.3 shows the data for determination of the absorption order at 245 nm for 4-MeQ. The data agrees well with a first order Poisson distribution corresponding to a one photon absorption process. The saturation energy is found to be 5.14 eV – well above the laser pulse energies used in these experiments.

A difference of the electronic transitions is also seen in the TD-DFT calculations (red bars in figure 5.2). 3-MeQ and 4-MeQ have two rela-

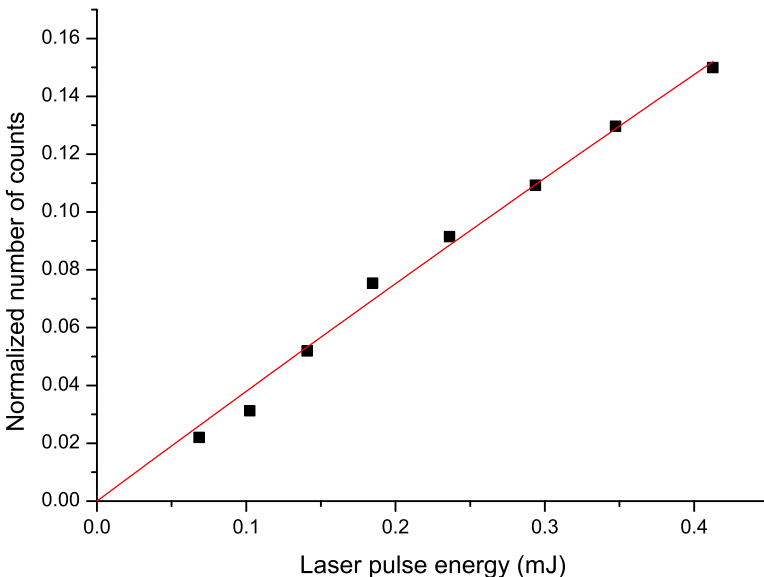


Figure 5.3: Measured absorption at 245 nm for 4-MeQ as a function of laser pulse energy for determination of the absorption order. The data has been fitted to give a saturation energy of 5.14 eV. The absorption order is clearly one.

tively strong transitions in the 220 – 227 nm region, while 6-MeQ and 8-MeQ only have one strong transition near 229 nm. Even though the calculated transitions do not match the measured absorption maxima exactly, the redshifting trend is clearly seen. The calculations also indicate that the experimentally observed absorption feature cannot be ascribed to the $S_0 \rightarrow S_1$ transition, but is a transition between the ground state and higher excited states $S_0 \rightarrow S_n$.

The calculated electronic transition energy cannot be directly compared to the measured absorption maximum, as the TD-DFT calculations give the vertical excitation energy, while the experimental absorption maximum is determined by the Franck-Condon overlap of the involved electronic states.

Dissociation channels

The mass spectra of the charged dissociation products from 4-MeQ and 6-MeQ produced by laser excitation are shown in figure 5.4. The methyl group is placed on the ring containing and not containing nitrogen, respectively, for the two isomers. At 230 nm, the most dominant channels are loss of methyl (or a molecule containing a single carbon atom and a number of hydrogen atoms) and a molecule containing two carbon atoms and a number of hydrogen atoms. Other channels are observed at lower masses but with much lower yield and will not be discussed further. The mass spectra are very similar for the two molecules, except that the dominant peak seems to be shifted from 117 amu (4-MeQ) to 115 amu (6-MeQ) (loss of C_2H_n or HCN). Because of the resolution and limitations of this method, it is not possible to measure the yield of hydrogen loss (atomic and/or molecular) from the mother molecule nor distinguish between e.g. C_2H_2 and C_2H_3 .

Table 5.2 gives the calculated adiabatic dissociation energies of the expected dissociation channels for 4-MeQ. The barriers for these transitions have not been found. Note that the absorbed photon carries an energy of $\sim 4.8 - 5.9$ eV. As seen in the table, the least expensive fragmentation channel is loss of a hydrogen atom on the methyl group, followed by loss of C_2H_3 from the heterocycle and C_2H_2 from the homocycle. Loss of the methyl group is less expensive than loss of hydrogen from the carbon and nitrogen atoms. The same results have been reported for non-nitrogen containing PAHs [113]. Even though it is not possible to measure this, hydrogen loss (either atomic or molecular) is

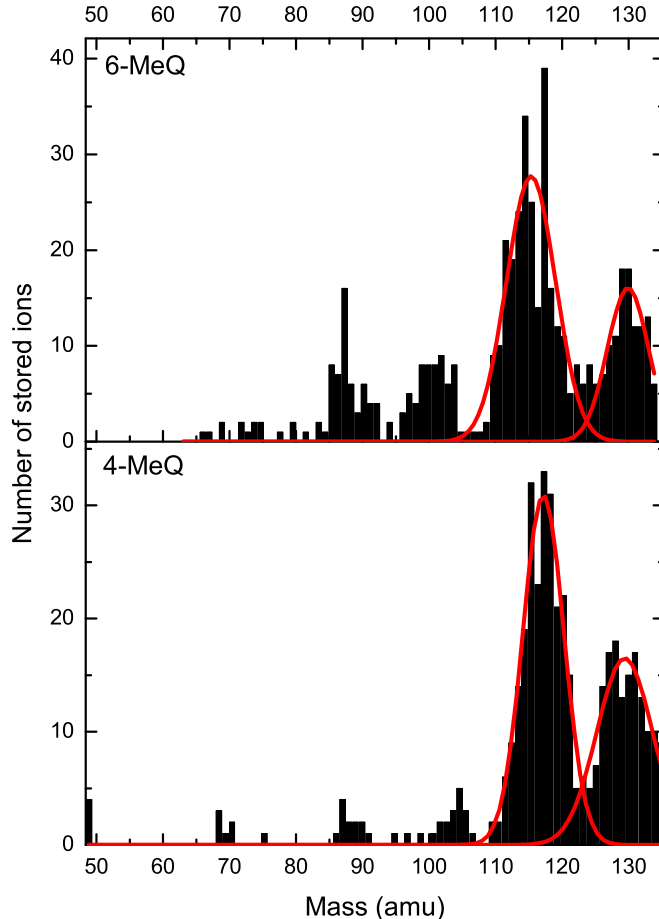


Figure 5.4: Mass spectra of the photodissociation products of 4-MeQ (lower panel) and 6-MeQ (upper panel) generated upon excitation by a 230 nm photon. Gaussian profiles have been plotted with centres at 117 and 129 amu for 4-MeQ and 115 and 129 amu for 6-MeQ. The main dissociation channels are identified to be methyl loss and loss of a molecule containing two carbon atoms and a number of hydrogen atoms.

an expected dissociation channel due to the low adiabatic dissociation energy.

As mentioned, we cannot distinguish between the loss of C_2H_2 and

Dissociation channel	E_{diss} (eV)
H from methyl	4.41
C_2H_3 from heterocycle	4.71
C_2H_2 from homocycle	4.79
Methyl	4.98
H from nitrogen atom	5.40
H from carbon atoms	5.51 – 5.68

Table 5.2: Calculated adiabatic dissociation energies of 4-MeQ.

C_2H_3 . The indole cation ($C_8H_7N^+$) is stable and therefore a possible end product after dissociation. The adiabatic dissociation energy of 4-MeQ and $C_2H_2 + H$ from the homocycle is 5.71 eV, while only 4.71 eV for 4-MeQ and C_2H_3 . To clarify which pathway is observed, transition state calculations have been carried out for the loss of C_2H_3 and the lowest barrier is found to be 9.9 eV. There are other possibilities for dissociation products. However, the complete potential energy surface for the dissociation pathways of photoexcited 4-MeQ has not been completed due to difficulties in obtaining optimised structures of the intermediate states. In the following, a discussion of the experimental results compared to results found in the literature is given.

Works published in the 1990's by Y. Gotkis *et al.* [117] and H. W. Jochims *et al.* [118] both show that atomic and molecular hydrogen and C_2H_2 are possible dissociation products after photoexcitation of PAHs cations with 7 – 35 eV photons. It was shown that smaller PAHs with less than 30 – 40 carbon atoms dissociate rather than relax by emission of IR photons.

Y. A. Dyakov *et al.* [116] have, by ab initio methods, investigated the reaction paths of H, H_2 , and C_2H_2 loss from the naphthalene cation via photodissociation. The photoproducts are shown together with the calculated barriers in figure 5.5. The C_2H_2 loss results in either benzocyclobutadien (a fusion of an aromatic and a four member ring) or phenylacetylene (an aromatic ring with a CCH side group) – both reaction products are around 4.7 eV higher in energy than naphthalene and the barrier is calculated to 4.93 eV. The reaction path involves either ring opening after migration of one of the H atoms or creation of the four member ring upon bending of one of the aromatic rings. The first barrier of H migration is 3.1 eV and the following is negligible. The H_2

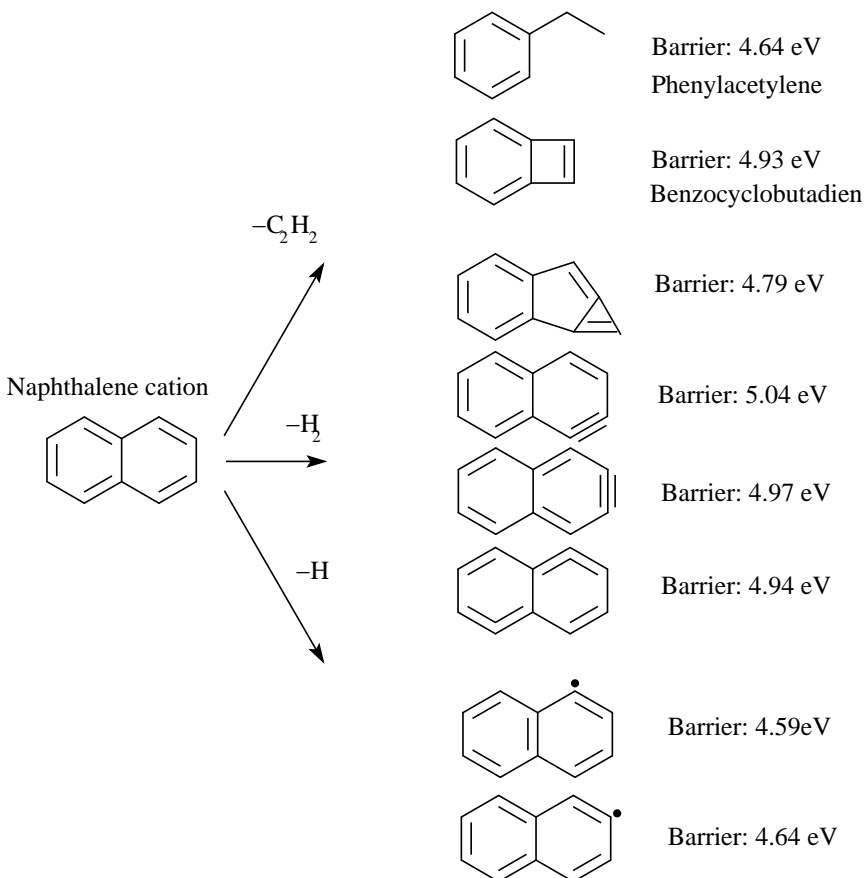


Figure 5.5: Some of the reaction products and barriers when photodissociating the naphthalene cation found by Dyakov *et al.* [116].

loss is also initiated by migration of H atoms around the carbon rings and H₂ is then emitted from the CH₂-group formed upon this migration. The migration is as mentioned nearly barrierfree, hence H₂ loss can happen from all carbon atoms in the aromatic ring. H loss occurs without a distinct transition state either by direct cleavage of the C-H bond or upon H migration and emission from the formed CH₂ group. The barrier is 4.59 eV. The barriers for all dissociation pathways are comparable and with only one exception less than 5 eV.

The groups of H. Cederquist in Stockholm and B. Huber in Caen have in collaboration studied multiple ionisation of PAHs as well as

dissociation of PAHs and PAH clusters [119–122]. The experiments involve collisions of neutral PAHs and PAH clusters with ions and the theoretical work includes calculations of dissociation and multiple ionisation energies for smaller PAHs not containing nitrogen or other substitutions. Again, loss of atomic hydrogen and C₂H₂ are observed channels.

F. Useli-Bacchitta *et al.* [62] noted that loss of C₂H₂ is seen when methyl substituted pyrene cations are excited by photons in the visible spectral range. They observe sequential loss of atomic hydrogen for all studied molecules (positively charged pyrene, methyl-pyrene, corone, and doubly dehydrogenated coronene).

H. A. B. Johansson *et al.* [88] (also a work from the group of H. Cederquist) studied the C₂H₂ and HCN dissociation channels for the linear, positively charged PAH anthracene (C₁₄H₁₀⁺) and PANH protonated acridine (C₁₃H₉NH⁺) in gas phase when collided by a neutral xenon target. Both molecules contain three aromatic rings, the only difference being the substitution of one of the central carbon atoms with a nitrogen atom. C₂H₂ and HCN are the main dissociation products, but groups of products centered around consecutive numbers of carbon atoms are also observed. The authors argue that the first step of the different dissociation channels of the protonated acridine cation, is loss of the hydrogen atom attached to the nitrogen atom. Their investigation of the dissociation pathways therefore starts from the acridine radical cation. The calculated barriers are 4.83 eV for loss of C₂H₂ and 5.27 eV for loss of HCN from the acridine radical cation. For the anthracene radical cation, the barrier for loss of C₂H₂ is 4.99 eV.

An IR multiphoton dissociation study by H. A. Galué *et al.* [105] finds that for protonated quinoline (129 amu) the fragment masses lie at 103, 102, and 77 amu. A possible explanation in line with the results of H. A. B. Johansson *et al.* [88] is a sequential dissociation route involving two processes: loss of HCN (27 amu) giving mass 103 amu followed by C₂H₂ loss (26 amu) eventually resulting in the creation of the phenyl cation (77 amu). The mass at 102 amu is explained by loss of H₂ followed by loss of C₂H₂. As for our technique, they cannot distinguish the loss of multiple hydrogen atoms or molecular hydrogen from the parent ion.

Our experimental results and both experimental and computational results found in the literature suggest that the mass spectra of the charged dissociation products can be interpreted as loss of methyl, C₂H₂, or

HCN, and atomic and molecular hydrogen. The reaction barriers stated in the literature is below the energy of the absorbed photons in our experiments and the dissociation pathways should be open. DFT calculations were performed to investigate the possible dissociation pathways of photoexcited 4-MeQ, but at present the calculations have not converged. The main problem is the ring opening before the molecule emits e.g. C₂H₂ or HCN. The pathways investigated include both protonated 4-MeQ and the radical cation generated after ejection of the H atom from the nitrogen atom. The calculations for the 4-MeQ radical cation (inspired by H. A. B. Johansson *et al.* [88]) are the most promising.

Dissociation times

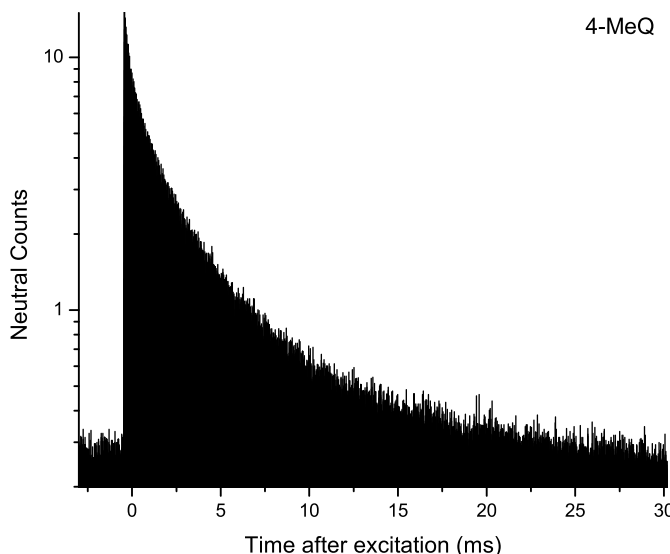


Figure 5.6: Number of neutrals measured 0 – 30 ms after photo-excitation 4-MeQ by a 230 nm ns pulse. The number of neutral counts have been normalised to the height of the injection peak not shown in this figure. It is clearly seen that the dissociation lifetime spans over several milliseconds. This is also seen for the other three methyl substituted quinolines studied at ELISA.

Figure 5.6 shows, as an example, the decay of 4-MeQ after excitation at 230 nm. The decay is clearly statistical with a lifetime of several milliseconds and hence energy is redistributed in the molecule before the decay. 4-MeQ does not have a simple exponential decay – most likely due to the spread in energy gained in the preparation process of the stored ions.

The Arrhenius model, which takes the energy spread of the molecules into account has been applied to the data. The fit gives an activation energy of about 4.5 eV and a pre-exponential factor of 10^{28} s^{-1} . The obtained activation energy is in relatively good agreement with the lowest dissociation energy of 4.41 eV (table 5.2). The dissociation rate gives a lifetime of $\sim 4 - 5 \text{ ms}$, which is of the same order of magnitude as calculated by Y. A. Dyakov *et al.* [116]. The two factors in the Arrhenius expression cannot be determined exactly as it requires time spectra at more wavelengths over the absorption feature. Based on the Einstein A-factor the radiative lifetime can be estimated from the frequency modes. The molecule is expected to decay radiatively with a lifetime of $\sim 91 \text{ ms}$ – an order of magnitude slower than the dissociation lifetime. The three other isotopes decay at the same time scale.

5.3 Conclusions and outlook

The action absorption spectra of four methyl substituted quinolines have been recorded in gas phase. The results show a redshift of 0.14 eV and clear broadening of the absorption profile when moving the methyl group from the heterocycle to the homocycle. TD-DFT calculations ascribe the main absorption to $S_0 \rightarrow S_n$ with $n \neq 1$ and show the same redshifting trend as the experimental data.

Many dissociation channels are observed after photoexcitation at 230 nm. The observed main channels are loss of methyl and a molecule containing two carbon atoms and a number of hydrogen atoms or HCN. Adiabatic dissociation energies calculated for 4-MeQ using DFT also give loss of hydrogen atoms and molecular hydrogen as possible dissociation channels, but the present technique cannot identify loss of masses less than 10% of the mass of the mother molecule. Loss of either C_2H_2 from the homocycle, C_2H_3 from the heterocycle, or CH_3 all have adiabatic dissociation energies smaller than the photon energy (5.40 eV). Transition state calculations of pathways of dissociation of

C_2H_3 from the heterocycle give an energy barrier of 9.9 eV, thus excluding this channel. However in the literature, several dissociation pathways for similar molecules have much lower barriers. The potential energy surface for the dissociation pathways of 4-MeQ have not been completed as the optimisation calculation for a couple of intermediate states have not converged yet.

The dissociation lifetime of 4-MeQ is several milliseconds and the decay is not a simple exponential. The three other molecules in this study have lifetimes of the same order of magnitude. Using the frequencies and IR intensities obtained from the DFT optimisation calculations, 4-MeQ is expected to decay radiatively with a lifetime of ~ 91 ms, which is an order of magnitude slower than the dissociation lifetime.

This study shows that the dissociation pattern of even small PAHs can be very complex and that dissociation happens faster than emission of the absorbed energy through the vibrational modes. Absorption of a UV photon leads to creation of cations which then, in turn can emit excess energy as infrared photons. These molecules should also be taken into account when considering molecules and ions contributing to the infrared emission features of the interstellar medium. The results obtained by the technique demonstrated in this study provide insight into many photophysical properties interesting in an astrophysical context. Experiments on other PAHs have the potential of giving key information for solving unanswered interstellar questions.

CHAPTER 6

Hydrogenated PAHs

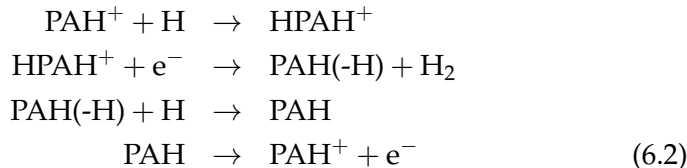
6.1 Introduction

H_2 plays a key role in the physical and chemical processes that lead to the formation of new stars and the evolution of interstellar chemical complexity [123]. The mechanisms behind the formation of H_2 in the ISM have been intensely studied. Formation routes on dust grain surfaces, as originally suggested by D. Hollenbach and E. E. Salpeter in 1971 [124], have proven efficient in low temperature dense and diffuse interstellar clouds [125–129], but not under harsher conditions such as those found in photodissociation regions (PDRs) [130, 131]. The presence of PAHs in regions with high rates of H_2 formation in PDRs [8] has led to the suggestion that PAHs could be the missing H_2 catalyst in these regions. The hypothesis is supported by the fact that H_2 and PAH emission are correlated in some interstellar regions [8, 132].

Theoretical studies have supported the hypothesis that PAH cations [113, 133–136] and superhydrogenated neutral PAHs [9, 137] might act as catalysts for H_2 formation. Laboratory experiments have shown that atomic and molecular hydrogen react with benzene and small PAHs [138–141]. Several mechanisms have been proposed involving PAHs as catalysts. The first step of reaction (6.1) (proposed by C. W. Bauschlicher Jr. in 1998 [142] and M. Hirama *et al.* in 2003 [134]) is hydrogenation of a normally hydrogenated PAH cation resulting in a protonated PAH cation (HPAH^+). The protonated cation can now react with a hydrogen atom which extracts the hydrogen atom and H_2 is formed.



This reaction was found inefficient by the group of V. Bierbaum and they proposed another mechanism [43, 136] shown in reaction (6.2). The first step is identical to the first step of reaction (6.1). In the second step, the protonated PAH cations combine with a free electron by dissociative recombination and form a dehydrogenated PAH ($\text{PAH}(-\text{H})$) and molecular hydrogen. The last two steps produce a free electron and a PAH radical cation.



In both cases, the net reaction is between two hydrogen atoms resulting in molecular hydrogen (reaction (6.3)), but PAH radical cations are needed as catalysts to make the reaction efficient.



More recently, the formation of superhydrogenated neutral coronene has been observed by scanning tunnelling microscopy, thermal desorption measurements, and infrared spectroscopy [143–145]. Very high superhydrogenation states approaching full superhydrogenation with one excess H atom per carbon atom were observed [145]. Furthermore, both infrared spectroscopy measurements and thermal desorption measurements provided evidence for hydrogen abstraction reactions producing H_2 , and hence showed that PAHs do act as catalysts for molecular hydrogen formation [144, 145]. The reaction cross section for these abstraction reactions was found to be $0.06 \text{ \AA}^2 \text{ pr. excess H atom}$ [144]. For PAHs with very high degrees of superhydrogenation, such a cross section could explain the high H_2 formation rates observed in low UV flux PDR regions [8]. Additionally, Y. Fu *et al.* [146] have recently shown that H_2 is formed upon exposure of a doubly hydrogenated PAH to UV-photons and found reaction routes with barriers of $2.3 - 3.4 \text{ eV}$.

Multiphoton infrared photodissociation studies [89, 147, 148] also show that H₂ is emitted by vibrationally excited hydrogenated PAHs. These findings highlight the fact that in order to be able to predict the efficiency of PAHs as interstellar molecular hydrogen catalysts we need detailed knowledge of the hydrogenation state of PAHs under interstellar conditions.

Establishment of the presence and hydrogenation state of PAHs is based on correlation between the frequencies of their vibrational modes and the aromatic emission features which appear in the 3 – 20 μm range throughout the entire galaxy [16]. The strong aromatic C-H stretch has a vibrational frequency of 3.3 μm while the aliphatic (e.g. C bonds to two H atoms) stretch is shifted to 3.4 μm. This emission band is also observed and hydrogenated PAHs are therefore likely components of the interstellar medium [31, 36–38]. However, quantitative estimates of the hydrogenation state of interstellar PAH molecules based on observations is so far not possible.

Besides acting as catalysts for H₂ formation, protonated and hydrogenated PAHs have been suggested as possible carriers of the diffuse interstellar bands (DIBs) [16]. Both computational and experimental results show that protonation and hydrogen addition strongly influence the optical spectra [21, 22, 149–155]. This indicates that although bare and singly protonated PAHs can be ruled out as carriers of the DIBs [23], hydrogenated PAHs cannot.

In the following, two studies involving hydrogenated PAHs are presented. First, the formation and stability of hydrogenated PAH cations was investigated using two very different types of ion sources. This work is published in *Astronomy & Astrophysics* [2]. Second, preliminary results of absorption, lifetimes, and dissociation channels of radical cations of pyrene and two different hydrogenation states of pyrene are shown and discussed.

6.2 Hydrogen addition to PAHs

Formation of hydrogenated PAH cations was investigated under very different external conditions. Hydrogenated cations of nitrogen substituted naphthalene, quinoline (C_9H_7N , 129 amu, Sigma Aldrich, purity > 97%), was formed from the soft ionisation method of the electrospray ionisation source (section 4.1). Both dehydrogenated and hydrogenated cations of pentacene ($C_{22}H_{14}$, 278 amu, Sigma Aldrich, purity 99%) were formed in the harsh environment of the Nielsen plasma source (section 4.2). Figure 6.1 shows the schematic structure of quinoline and pentacene. The ion sources were mounted on the HV-platform and the ions (singly charged) were accelerated to 20 keV. The outcomes of the ion sources were then analysed by scanning the magnetic field and thereby measuring the ion yield on the MCP detector as a function of mass over charge. In the resulting mass spectra it is possible to distinguish ions with 1 amu mass difference.

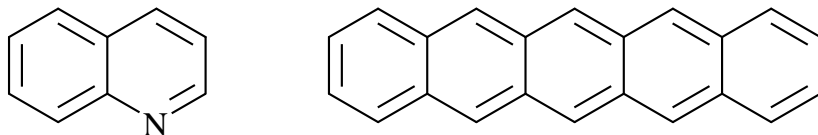


Figure 6.1: Quinoline (C_9H_7N , 129 amu, left) and pentacene ($C_{22}H_{14}$, 278 amu, right). Because of the nitrogen atom, protonated quinoline and its hydrogenated states are easily generated in the electrospray ionisation source. Pentacene is solid at room temperature and the radical cation as well as cationic de- and hydrogenated states were produced by a Nielsen plasma ion source.

Density functional theory calculations were performed for comparison with the experimental results. Structure optimisation and energy calculations were carried out at the B3LYP level of theory and using the 6-311+G(d,p) basis set for the smaller molecules, quinoline and naphthalene, and 6-31+G(d,p) for the bigger, pentacene. Zero point corrections and scaling of the vibrational energies were taken into account. All vibrational frequencies were found to be positive for the optimised structures.

Structure optimisation of the hydrogenated PAHs and calculation of their energies is a cumbersome job as hydrogenation can lead to many

different isomers. For example, doubly hydrogenated pentacene with two excess H atoms ($C_{22}H_{16}$, here denoted H_2Pen) has 34 different isomers, corresponding to the different positions of the extra hydrogen atoms on the perimeter of the molecule. The experience gained from the calculations for quinoline and naphthalene has therefore been taken into account when performing the calculations for pentacene.

In the following, we define the binding energy of a hydrogen atom to an already hydrogenated PAH according to

$$E_{bind} = E_H + E_{n-1} - E_n, \quad (6.4)$$

where n is the number of hydrogen atoms attached to the molecule, E_n the energy of the corresponding molecule and E_H the energy of a hydrogen atom.

The hydrogenated states of protonated quinoline and the pentacene cation will be denoted H_nQuiH^+ and H_nPen^+ , respectively.

6.2.1 Quinoline

Figure 6.2 shows the mass spectrum of the hydrogenated and dehydrogenated states of protonated quinoline (C_9H_7N , 129 amu, shown schematically in figure 6.1), generated by spraying a sample of quinoline dissolved in methanol (a drop of acetic acid was added to the solution to enhance protonation). Only a weak yield of the radical cation (129 amu) and dehydrogenated states is observed as expected considering the preparation method of the ions. Hydrogenated states are produced up to $+8H$ – the same as the number of edge atoms of the structure. In the mass spectrum, the number of extra hydrogen atoms ascribed to the individual peaks corresponds to the number of extra hydrogen atoms with reference to the protonated molecule.

Mass spectra give an indication of the relative stability of the different species, i.e., the more stable a molecule the higher the expected yield. The binding energies of all the different isomers were calculated for every state of hydrogenation for both quinoline and naphthalene – the unsubstituted brother of quinoline. Table 6.1 presents both the most stable isomers and a direct route of hydrogenation, where a single hydrogen atom is added along with their binding energies. The binding energies are plotted in figure 6.3 as a function of the total number of hydrogen atoms attached to the PAH. The energy difference of the lowest isomers can in a few cases be as low as 0.007 eV, less than the accuracy

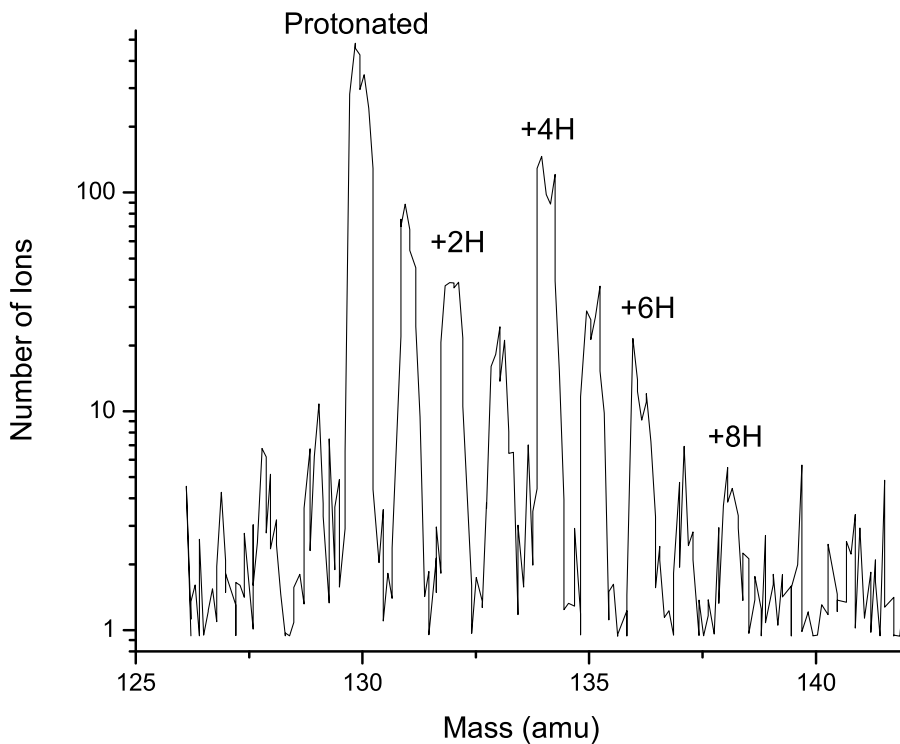


Figure 6.2: Mass spectrum of hydrogenated and dehydrogenated states of protonated quinoline generated in the electrospray ionisation source. All hydrogenated states bear a single positive charge. The number of extra hydrogen atoms ascribed to the individual peaks is with reference to the protonated quinoline cation. Note the logarithmic scale.

of the calculations. Hydrogenated states with isomers with energy differences below 0.1 eV have been marked with a * in tables 6.1 and 6.2 and only the lowest energy isomer is shown.

A clear odd-even pattern in terms of n is visible in table 6.1 and figure 6.3: The energy released by attaching a hydrogen atom resulting in a molecule with an even number of attached hydrogen atoms is considerably higher (~ 2 eV) than that resulting in a molecule with an odd number of hydrogen atoms. For naphthalene, the binding energies reveal that hydrogenation of the second aromatic ring takes place independently of the first ring as $E_{bind}(n) \simeq E_{bind}(n + 4)$. This does not apply to quinoline due to the effects of the nitrogen atom.

Quinoline is similar to naphthalene ($C_{10}H_8$), except for the substitu-

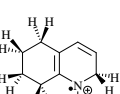
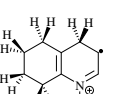
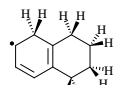
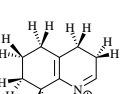
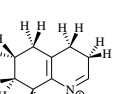
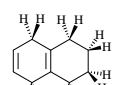
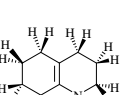
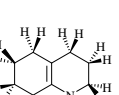
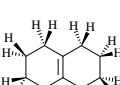
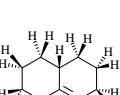
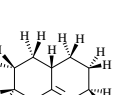
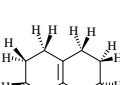
n	E_{bind} (eV)	Quinoline Lowest energy isomer	E_{bind} (eV)	Quinoline Direct addition	E_{bind} (eV)	Naphthalene
1	2.0*		2.0		1.6	
2	3.9*		3.9		3.9	
3	2.5*		2.5		2.4	
4	4.0		4.0		4.2	
5	2.0		1.8		1.5*	
6	3.4		3.6		3.8*	
7	3.1		3.1		2.6	
8	3.8		3.8		4.1	

Table 6.1: Binding energies for attaching a hydrogen atom to protonated quinoline and neutral naphthalene according to equation (6.4) using B3LYP/6-311+G(d,p). The final structure (with energy E_n) of the attaching process is shown. The binding energies labelled by a * indicates molecules with stable isomers with energy differences less than 0.1 eV.

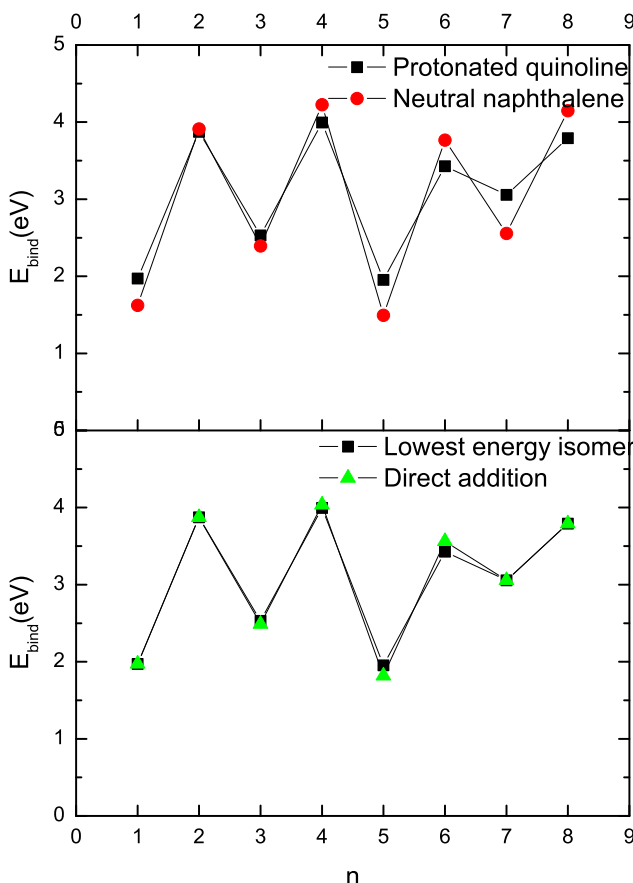


Figure 6.3: The binding energy of a hydrogen atom of a certain hydrogenated state of protonated quinoline and neutral naphthalene. n is the total number of hydrogen atoms attached to the PAH and E_{bind} is calculated according to equation (6.4). The upper graph shows the binding energies of the lowest energy isomers for protonated quinoline and neutral naphthalene. The lower graph shows the comparison of the binding energies of the lowest energy isomers and direct addition of protonated quinoline. A clear odd-even pattern is clear in all cases.

tion of a carbon and hydrogen atom by a nitrogen atom. The two molecules are isoelectronic and the substitution is only expected to cause small perturbations to the bond lengths. Protonation of quinoline does not change this. Indeed, the computational results for the binding of hydrogen to protonated quinolines presented in figure 6.3 and table

6.1 show that the trends of hydrogenation of the protonated quinoline cation and neutral naphthalene are the same. Nitrogen substituted PAHs are also very likely components of the interstellar medium and the hydrogenation of quinoline is thus interesting. One advantage of studying nitrogen substituted PAHs lies in them having a higher proton affinity because of the electronic lone pair of the nitrogen atom, hence making them easier to produce as ions and ideal for electrospray ionisation.

The results show that for +1H, hydrogenation of the carbon atoms nearest to the fusion of the aromatic rings is most favourable. For an even number of extra hydrogen atoms, the last hydrogen atom is added adjacent to the previous addition, hence minimising the number of broken double bonds as expected from the work of C. W. Bauschlicher Jr. [142]. Up to $n = 4$, the hydrogenation process is expected to occur on the same ring thus preserving the aromacity of the other ring. Interestingly, while for most hydrogenated states the hydrogenation of the nitrogen atom is energetically unfavourable, for the +4H case, calculations show that full hydrogenation of the aromatic ring including the protonated nitrogen atom is stable by > 0.8 eV compared to partial hydrogenation of both rings. Full hydrogenation of the ring not containing nitrogen (shown in table 6.1) is still the most stable isomer by 0.5 eV.

After full hydrogenation of the aromatic ring not containing nitrogen, hydrogenation of the other ring follows the same scheme. Finally, for +8H, hydrogenation of one of the skeleton carbon atoms is energetically more favourable than hydrogenation of the protonated nitrogen atom. The H_8QuiH^+ -state does therefore not, according to the calculations, correspond to full hydrogenation of the edge atoms.

A striking feature in the mass-spectrum is the relatively high abundance of H_4QuiH^+ . Calculations show that this state, together with H_2QuiH^+ have the highest binding energy. The odd-even pattern is only weakly seen in the mass spectrum (figure 6.2).

6.2.2 Pentacene

Figure 6.4 shows the mass spectrum of pentacene ($\text{C}_{22}\text{H}_{14}$, 278 amu), exhibiting several interesting features. The radical cation is produced in significant amount as well as both dehydrogenated and hydrogenated pentacene cations. Some of the hydrogenated pentacene cations are

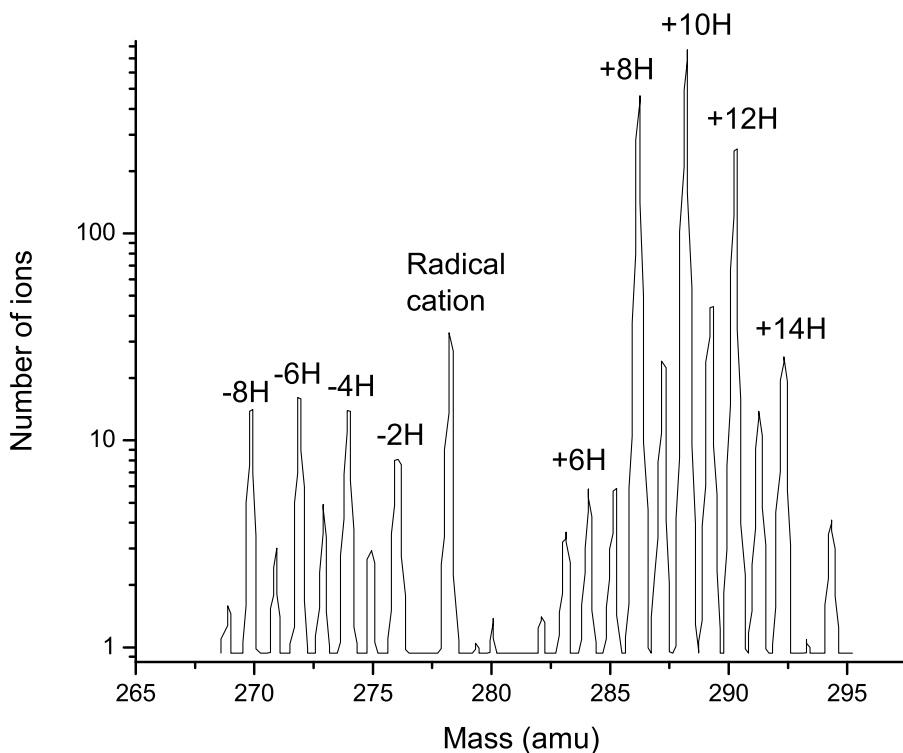


Figure 6.4: Mass spectrum of hydrogenated and dehydrogenated states of pentacene generated in the hot Nielsen plasma ion source. All hydrogenated states bear a single positive charge. Note the logarithmic scale.

even more prominent than the radical cation, and the yield of the higher hydrogenated states is 100 times larger than that of the lower hydrogenated states. Hence, a considerable amount of hydrogen must be present in the ion source. The small peak at 279 amu (corresponding to HPen^+) could be ascribed to isotope effects (^{13}C) while no peak is observed at 281 amu (corresponding to H_3Pen^+) in the spectrum. In this spectrum, the odd-even effect is very prominent. All states with an even number of hydrogen atoms are generated. The dehydrogenated states are probably generated by collisions in the plasma and H/H_2 exchange between the PAHs is likely to occur. An additional peak appears at mass 294 amu corresponding to $278 + 16$ amu. Two possible explanations have crossed our minds: Either hydrogenation of the skeleton could have taken place or an oxygen atom could have been at-

tached to the pentacene radical cation. The pentacene-oxygen complex could be dehydrogenated in the same manner as the bare pentacene radical cation explaining the resemblance between the pattern in mass 270 – 276 amu and 286 – 292 amu. None of these possible explanations have been investigated further.

An alternative interpretation of the presence of molecules with mass 292 amu would be the substitution of an H atom with a methyl group, the mass of which happens to coincide with full hydrogenation of the edge sites of pentacene. In this scenario, hydrogen atoms would then be stripped off the methyl substituted pentacene cation in the same way as for the radical pentacene cation resulting in two groups in the mass spectrum corresponding to dehydrogenation of the radical pentacene cation and the methyl substituted pentacene cation, respectively. However, since no sign of ions with masses corresponding to substitution of two methyl groups and its dehydrogenated states was seen, we interpret the ions with masses 279 to 292 amu to be hydrogenated states of pentacene.

Figure 6.5 shows the binding energies for the lowest energy isomers of the hydrogenated states of pentacene. For comparison, figure 6.6 shows the binding energies for a direct route of hydrogen addition leading to full hydrogenation of pentacene. The structures are depicted in the tables 6.2 ($n=1 - 7$) and 6.3 ($n=8 - 14$) along with the calculated binding energies. The calculations have been carried out for both cations and neutrals. The odd-even pattern clearly present in the experimentally obtained mass spectrum is also recognised in the calculations. For the neutral molecules, an even number of extra hydrogen atoms result in higher stability as expected based on electronic shell closing. On the basis of shell closing, one also expects that for the cation the odd hydrogenation numbers will be more stable, which according to calculations, is indeed the case except for +4H and +8H which appear as magic numbers even for cations. Thus, the odd-even pattern observed in the experiment suggests that in the Nielsen ion source, hydrogenation takes place prior to ionisation. Thus, the mass spectrum is related to the stability of the neutral molecules rather than the cations.

The calculations show (see tables 6.2 and 6.3) that the central edge carbon atom is the most favoured hydrogenation site when adding a single hydrogen atom to a stable structure (+1H, +3H, +5H and +9H). For adding two hydrogen atoms, the same trend of hydrogenation as for protonated quinoline and neutral naphthalene appears, namely hy-

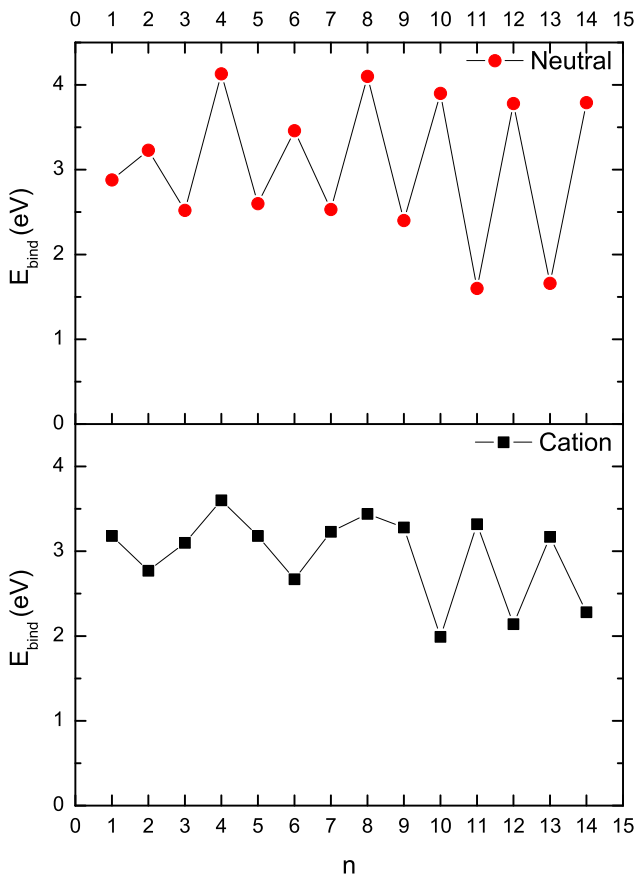


Figure 6.5: The binding energy of a hydrogen atom of a certain hydrogenated state of pentacene resulting in the lowest energy isomer of the hydrogenated state (see tables 6.2 and 6.3). n is to the total number of hydrogen atoms attached to the PAH and E_{bind} is calculated according to equation (6.4). Note the clear odd-even pattern for the neutral, while magic numbers of $n = 4$ and $n = 8$ appear for the cation. This corresponds to hydrogenation of either one or both of the outer rings.

drogenation of two adjacent carbon atoms in one of the outer rings near the ring fusion ($+2\text{H}$, $+4\text{H}$, $+6\text{H}$ and $+8\text{H}$). When both outer rings have been fully hydrogenated, hydrogenation of the central rings begins. The $+10\text{H}$ to $+13\text{H}$ states all have several stable structures that are very close in energy, but as for quinoline, the isomers of the lowest energy route of hydrogenation is shown. In the pentacene case, with a PAH

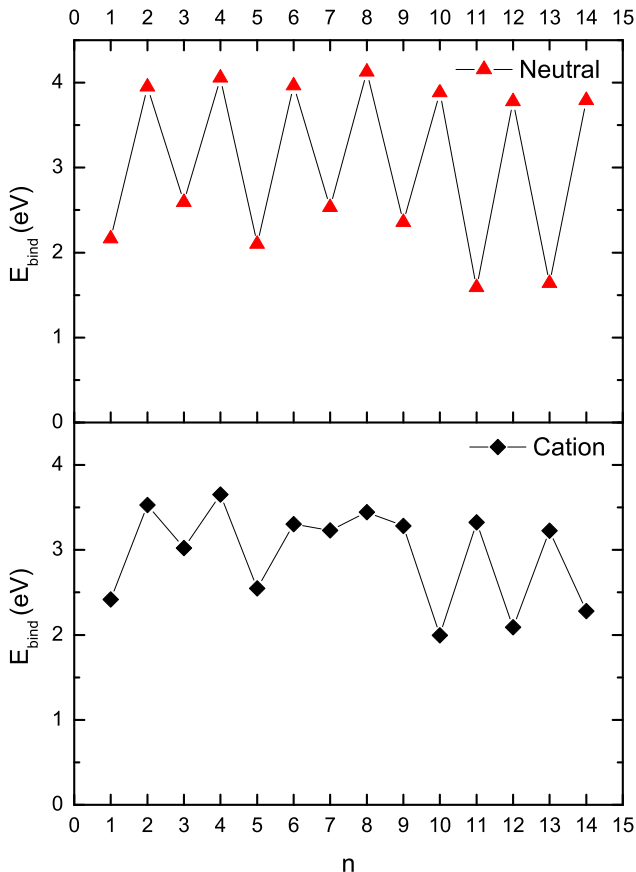


Figure 6.6: The binding energy of sequential addition of a hydrogen atom to hydrogenated pentacene (see tables 6.2 and 6.3). This is the lowest energy path found. n is to the total number of hydrogen atoms attached to the PAH and E_{bind} is calculated according to equation (6.4). Note the clear odd-even pattern for the neutral, while magic numbers of $n = 4$ and $n = 8$ appear for the cation. This corresponds to hydrogenation of either one or both of the outer rings.

skeleton consisting solely of carbon atoms, hydrogenation of the edge atoms is much preferred compared to the carbon atoms in the ring fusions. The sequential addition of hydrogen atoms thus follows the same trend as for protonated quinoline and neutral pentacene. Hydrogenation of the end rings happens one at a time, breaking only one double bond at a time. When both outer rings have been fully hydrogenated,

n	Cat. E_{bind} (eV)	Neu. E_{bind} (eV)	Structure	Cat. E_{bind} (eV)	Neu. E_{bind} (eV)	Structure
			Lowest energy isomer			Direct addition
1	3.2	2.9		2.4	2.1	
2	2.8	3.2		3.5	3.9	
3	3.1*	2.5		3.0	2.6	
4	3.6	4.1		3.7	4.1	
5	3.2	2.6		2.5	2.1	
6	2.7	3.5		3.3	4.0	
7	3.2	2.5		3.2	2.5	

Table 6.2: Binding energies for attaching a hydrogen atom to cationic and neutral pentacene for $n = 1 - 7$ according to equation (6.4) using B3LYP/6-31+G(d,p). The binding energies labeled by a * indicates molecules with stable isomers with energy differences less than 0.1 eV.

hydrogenation of the central rings begins.

Interestingly, in the mass spectra there is almost no yield of hydrogenated states below +5H. According to the calculations, this corresponds to full hydrogenation of one of the outer rings and one of the central edge carbon atoms. A large increase in ion yield is observed for the +8H state, after which the height of several of the peaks is even higher than that of the radical ion. The ion abundance from the ion source is related to the stability of the molecules, but also the amount

n	Cat. E_{bind} (eV)	Neu. E_{bind} (eV)	Structure		Cat. E_{bind} (eV)	Neu. E_{bind} (eV)	Structure	
			Lowest energy isomer				Direct addition	
8	3.4	4.1			3.4	4.1		
9	3.3	2.4			3.3	2.4		
10	2.0*	3.9			2.0	3.9		
11	3.3*	1.6			3.3	1.6		
12	2.1*	3.8			2.1	3.8		
13	3.2*	1.7			3.2	1.6		
14	2.3	3.8			2.3	3.8		

Table 6.3: Binding energies for attaching a hydrogen atom to cationic and neutral pentacene for $n = 8 - 14$ according to equation (6.4) using B3LYP/6-31+G(d,p). The binding energies labeled by a * indicates molecules with stable isomers with energy differences less than 0.1 eV.

of hydrogen available for hydrogenation in the source and the duration of presence of the molecules in the plasma. The distribution of hydrogenation states may depict an equilibrium of H/H₂ exchange of the dehydrogenated and hydrogenated pentacene cations. The gap in abundance below +5H, and the stepwise increase in abundance at +8H are prominent effects, which are probably explained by the internal ion

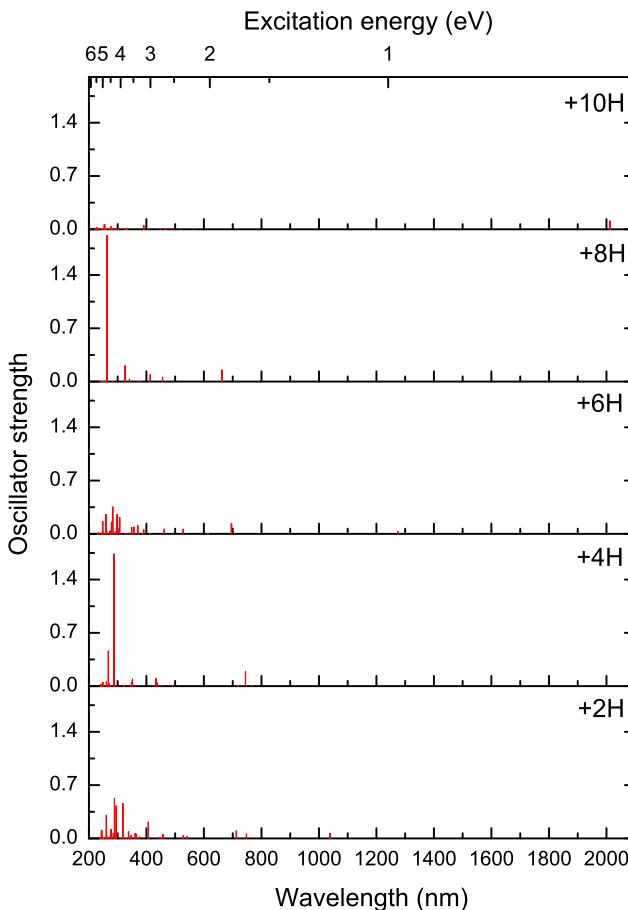


Figure 6.7: Excitation energies of different hydrogenated states of pentacene calculated by TD-DFT. There is no clear trend in the excitation energies as a function of the degree of hydrogenation. The results suggest that the electronic transitions cannot explain the gap in the mass spectrum from H_1Pen^+ to H_4Pen^+ .

source conditions.

This conclusion has been drawn after several considerations. The possibility of photodestruction of the lower hydrogenated states of pentacene due to a pattern in the excitation energies was looked into. In the plasma in the ion source, UV-photons are present as a consequence of recombination processes, and these photons may photoexcite the hydrogenated pentacene cations. This could result in dissociation of the

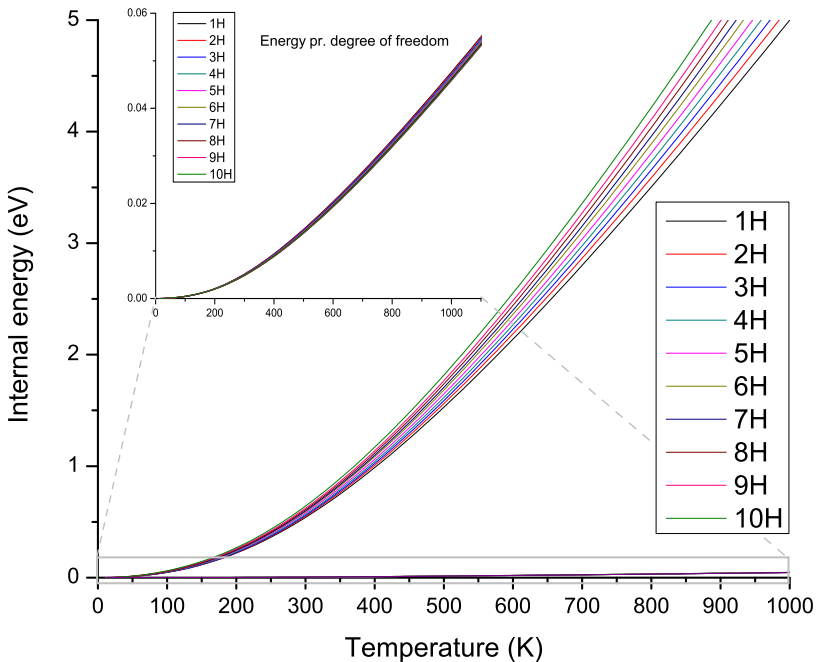


Figure 6.8: Internal vibrational energy as a function of temperature for different hydrogenation states. The inset shows the internal vibrational energy per degree of freedom. This is the same for all hydrogenation states and can therefore not explain the gap in the mass spectrum from H_1Pen^+ to H_4Pen^+ .

hydrogenated molecules. Therefore, TD-DFT calculations (B3LYP/6-31+G(d,p)) were carried out to clarify this. Here, only the excitation energies of the even hydrogenation states were calculated, as the abundance of these ions is the highest. The results are shown in figure 6.7. As can be seen, there is no clear pattern in the calculated electronic transitions neither regarding wavelength nor oscillator strength. For +2H and +10H, transitions in the near-IR region with low oscillator strengths are present, while +4H and +8H both show strong transitions in the near-UV region. On the basis of these calculations, we conclude that the absence of H_1Pen^+ to H_4Pen^+ cannot be explained by photodestruction upon photon excitation.

Another possibility is the destruction of ions and molecules due to their internal vibrational energy. The internal vibrational energy is de-

terminated by the temperature in the plasma. As mentioned in section 4.2, the temperature distribution of the ions is very broad and most molecules have a temperature of 800 – 1000 K. The internal energy can be calculated from the frequencies of the vibrational modes of the molecules. Figure 6.8 shows the internal energy of H_1Pen^+ to $\text{H}_{10}\text{Pen}^+$ as a function of the temperature of the molecules. At 800 – 1000 K the molecules possess 3.5 to 6 eV which corresponds to 0.04 – 0.06 eV per degree of freedom (illustrated in the inset in the figure). Only if the entire internal energy is directed into one specific vibrational normal mode is there sufficient energy to break the weakest bond (the aliphatic C-H bond), thereby destroying the hydrogenated state and removing it from the mass spectrum. Even if the energy was high enough, the internal energies of H_1Pen^+ to H_4Pen^+ are not very different from the higher hydrogenation states.

6.2.3 Conclusions and outlook

The experimental results show that both protonated quinoline and pentacene can be formed in multiply hydrogenated states under conditions and with ionisation methods that are very different. The hydrogenated protonated quinolines have been formed by the soft method of electrospray ionisation, where the molecules are very unlikely to break apart. Protonation of PAHs by electrospray ionisation have previously been reported [89, 147, 148, 152, 153], but here, it is shown that up to full hydrogenation of the edge sites occur. Cationic states of highly hydrogenated pentacene are generated in the harsh environment of the Nielsen plasma ion source, thus demonstrating very high stability.

The results are supported by calculations by several groups [71, 156]. J. A. Rasmussen *et al.* [71] show that chemical binding of hydrogen to neutral pyrene (a small PAH consisting of four fused aromatic rings) is exothermic by 1.6 eV and the barrier for further hydrogenation is negligible (0.06 eV). A. Ricca *et al.* [156] find that single hydrogenation of the naphthalene cation has no barrier while double hydrogenation has a small barrier. In this study, the reaction barriers for hydrogen addition was not calculated. Nevertheless, the measurements show that the barrier can be passed both in solution and in gas phase, as hydrogenated PAHs are observed from both ion sources, indicating low reaction barriers.

The very clear odd-even pattern in the experimental mass spectrum

of the pentacene cations is matched by the binding energies of the neutral hydrogenated pentacene states and not by the hydrogenated pentacene cations. Thus the hydrogenation process is likely to take place prior to the ionisation in the Nielsen plasma ion source. For protonated quinoline, the binding energy of a hydrogen atom to $H_n\text{QuiH}^+$ is ~ 2 eV higher for even than odd n 's. The odd-even pattern is only seen weakly in the experimental mass spectrum of protonated quinoline, although $H_4\text{QuiH}^+$ has the highest abundance after QuiH^+ . The trend of the hydrogenation sites of the investigated molecules are in agreement with the calculations by A. Ricca *et al.* [156].

A study by L. Boschman *et al.* [157] from December 2012 showed that when exposing coronene cations to atomic hydrogen gas, the hydrogen sticks sequentially to the cations. The results show that odd hydrogenation states dominate the mass spectrum. This is interpreted as proof of an energy barrier for formation of even hydrogenation states. These results also suggest that formation of closed shell molecules is favoured. The same is found for neutral coronene by E. Rauls and L. Hornekær [9]. These results support the claim that hydrogenation of pentacene takes place prior to ionisation of the generated species.

This study was motivated by the still unanswered question of H_2 formation in intermediate temperature regions of the interstellar medium. Both PAHs and their de- and hydrogenated forms have been proposed as catalysts. This study has shown stability and abundance of highly hydrogenated PAHs. In addition, V. Mennella *et al.* [144] have recently shown that the degree of hydrogenation plays a critical role in the process of H_2 formation. These findings encourage further experimental work on the subject. It is not possible to compare the results of this study directly to astrophysical objects as the exact conditions in the sources are not known, but the results show that hydrogenated PAHs are indeed stable under very different conditions. The formation of highly hydrogenated PAHs in the gas phase from bare PAHs underpin the attribution of the $3.4 \mu\text{m}$ IR feature to the C-H stretch of hydrogenated PAHs. As PAHs are unarguably components of the interstellar medium and because of the shown stability, we conclude that a wide range of hydrogenated PAHs are very probable components of the interstellar medium.

6.3 Absorption spectra of HPAHs

In this section, preliminary results obtained at ELISA on the radical cations of pyrene, Pyrene $^{+\bullet}$ ($C_{16}H_{10}^{+\bullet}$) and two hydrogenated derivatives of pyrene, tetrahydropyrene, $H_4\text{Pyrene}^{+\bullet}$ ($C_{16}H_{14}^{+\bullet}$), and hexahydropyrene, $H_6\text{Pyrene}^{+\bullet}$ ($C_{16}H_{16}^{+\bullet}$), are discussed. The molecular structures are shown in figure 6.9. As can be seen, the aromatic parts of the molecules are very different. For pyrene, it spans the entire molecule. The aromatic part of tetrahydropyrene consists, in the simple picture, of two decoupled aromatic benzene rings, biphenyl. The aromatic part of hexahydropyrene resembles the naphthalene molecule.

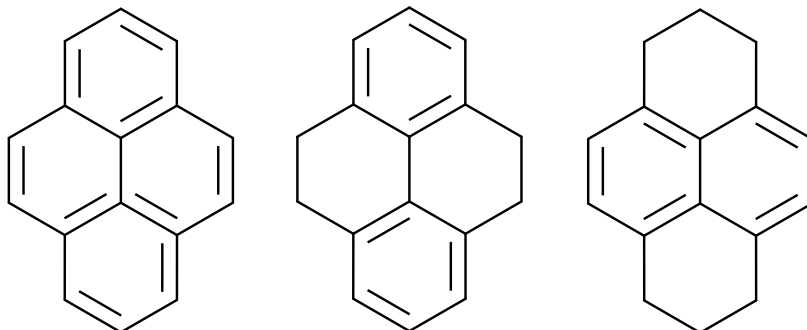


Figure 6.9: From the left: Pyrene ($C_{16}H_{10}$), tetrahydropyrene ($H_4\text{Pyrene}$, $C_{16}H_{14}$) and hexahydropyrene ($H_6\text{Pyrene}$, $C_{16}H_{16}$).

6.3.1 Experimental and computational details

The experiments have been performed at ELISA using the electrospray ion source for the production of the radical cations of the mentioned species. The experiments have mainly been performed in the visible window of the EKSPLA laser (420 – 710 nm), however, a few measurements were made in the UV region to clarify the need of further experiments.

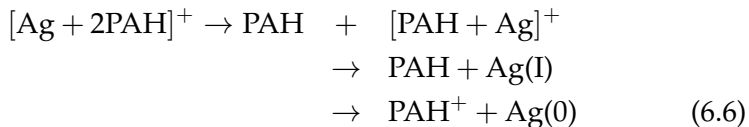
As described in section 4.1, the radical cations can be produced during electrospray ionisation of the molecules dissolved in a solution of water and methanol (1:1) with 0.1 mmol/L silver(I)nitrate (AgNO_3) [86–88, 158]. The simple explanation of how the radical cations are

produced is the reduction of Ag(I) to silver metal, Ag(0), by electron transfer from the PAH molecule as shown in reaction (6.5).



Here, the only requirement is that the ionisation energy of the PAH molecule is lower than that of silver. Hence, the electron transfer reaction is exothermic. Silver has an ionisation energy of 7.57 eV and pyrene one of 7.43 eV. This condition is verified by T. Ghislain *et al.* [87] as the radical cation of pyrene is produced while fluoranthene (ionisation energy of 7.9 eV) cannot be ionised.

An alternative explanation of the production process of the radical cations of PAHs was proposed by K. M. Ng *et al.* [158] and shown in reaction (6.6). The presence of $[\text{Ag}+2\text{PAH}]^+$ in their experiments support the proposed route. Again, the restriction on the ionisation energy of the PAH molecule applies.



Density functional theory calculations were performed for comparison with the experimental results with the Gaussian03 package [79]. Structure optimisation and energy calculations were carried out at the B3LYP level of theory and using the 6-311+G(d,p) basis set for the smaller molecules. TD-DFT was applied to obtain information on the electronic transitions and for these calculations the 6-31G(d,p) basis set was used to lower the computational costs. Zero point corrections and scaling of the vibrational energies were taken into account. All vibrational frequencies were found to be positive for the optimised structures.

6.3.2 Results

Lifetimes

For all three radical cations, both prompt and delayed action is observed. The prompt action (time scale of $\sim 10 - 15 \mu\text{s}$) has a very high yield. An example of the statistical dissociation giving the delayed action is shown in figure 6.10. Here, the lifetime spectra of $\text{H}_4\text{Pyrene}^{+\bullet}$

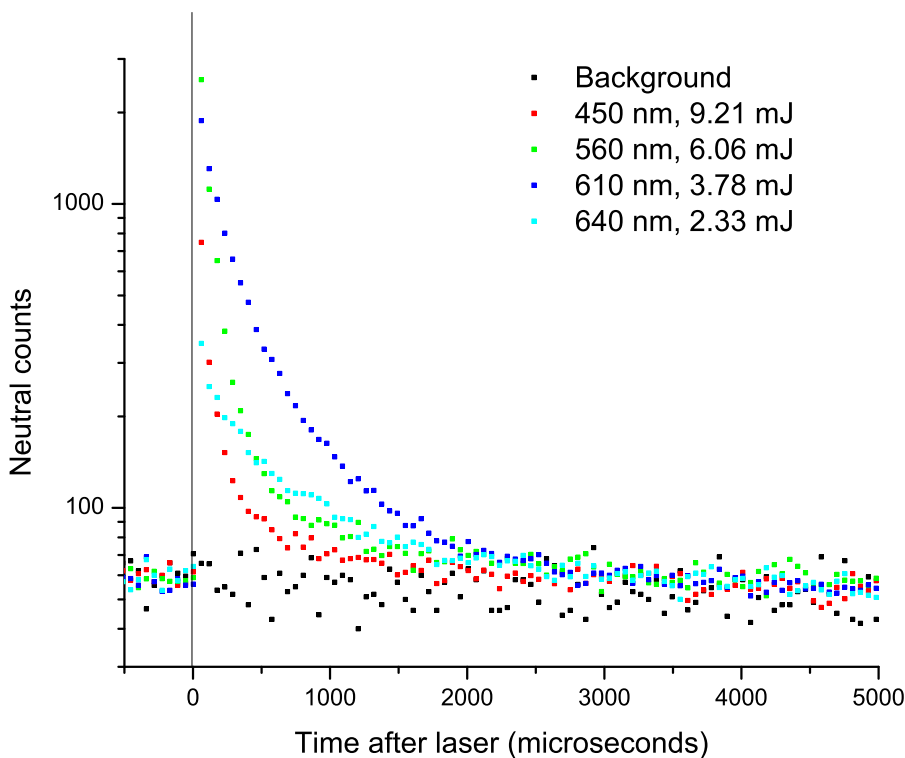


Figure 6.10: As an example of the statistical decay: the lifetime spectrum of $\text{H}_4\text{Pyrene}^{+\bullet}$ monitored by the MCP detector.

excited at different wavelengths monitored by the MCP detector are presented. The decay takes $\sim 2 - 3$ ms and becomes faster at shorter wavelengths. The higher photon energy associated with a shorter wavelength leaves the ions hotter after internal conversion of the electronic energy to vibrational energy in the ground state, which leads to faster dissociation of the ions. At higher laser pulse energies, the contribution from multiphoton processes becomes more dominant. In the experiments, the laser pulse energy increases with decreasing wavelength. This effect also contributes to faster decays at shorter wavelengths. This factor could be eliminated by keeping the laser pulse energy constant during the measurements of the lifetime spectra.

The statistical decay of $\text{Pyrene}^{+\bullet}$ is faster and the laser induced signal can only be distinguished from the background at times up to 1 ms. $\text{H}_6\text{Pyrene}^{+\bullet}$ shows a statistical decay up to ~ 2 ms.

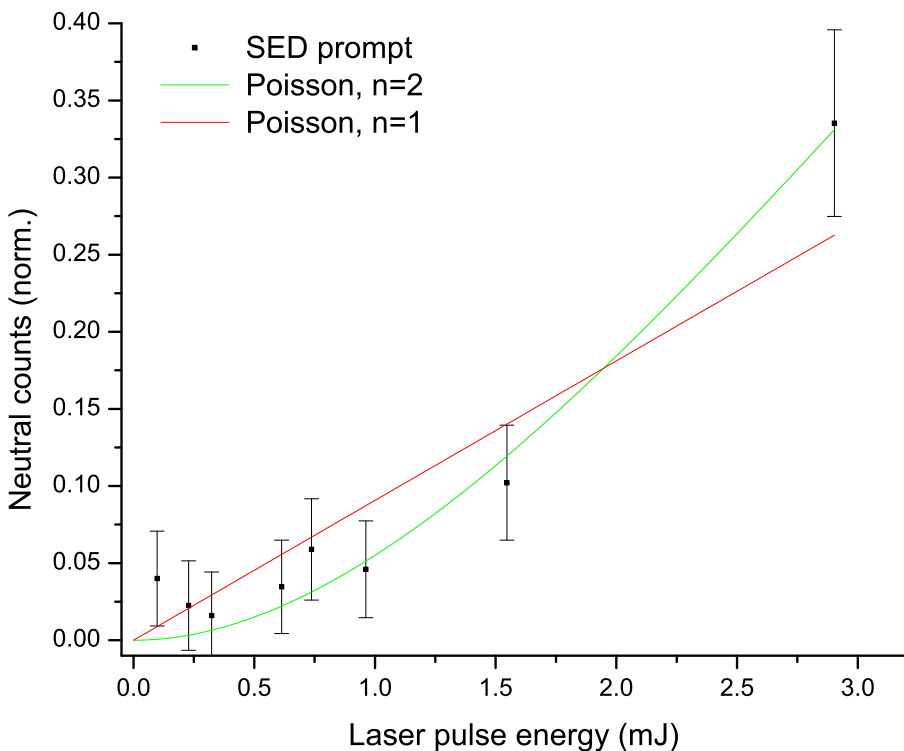


Figure 6.11: Determination of the absorption order of prompt action upon photoexcitation of $\text{H}_4\text{Pyrene}^{+\bullet}$ at 630 nm.

Order of absorption

To determine the order of absorption, the yield of neutral fragments as a function of laser pulse energy was measured. The order of absorption has been determined for both the prompt action and the delayed action. Both indicate multiphoton absorption for all three molecules.

The measurements of the neutral fragment yield as a function of laser pulse energy for $\text{H}_4\text{Pyrene}^{+\bullet}$ excited at 630 nm can be seen in figures 6.11 (prompt action) and 6.12 (delayed action). From both figures, it is clear that a single photon cannot cause dissociation at the time scale monitored in this experiment. Decay resulting from single photon absorption is expected to happen, but either the decay time scale is much too long to be measured with the chosen experimental parameters or the energy is irradiated as IR photons. The exact number of absorbed photons is very hard to determine as it requires careful measurements

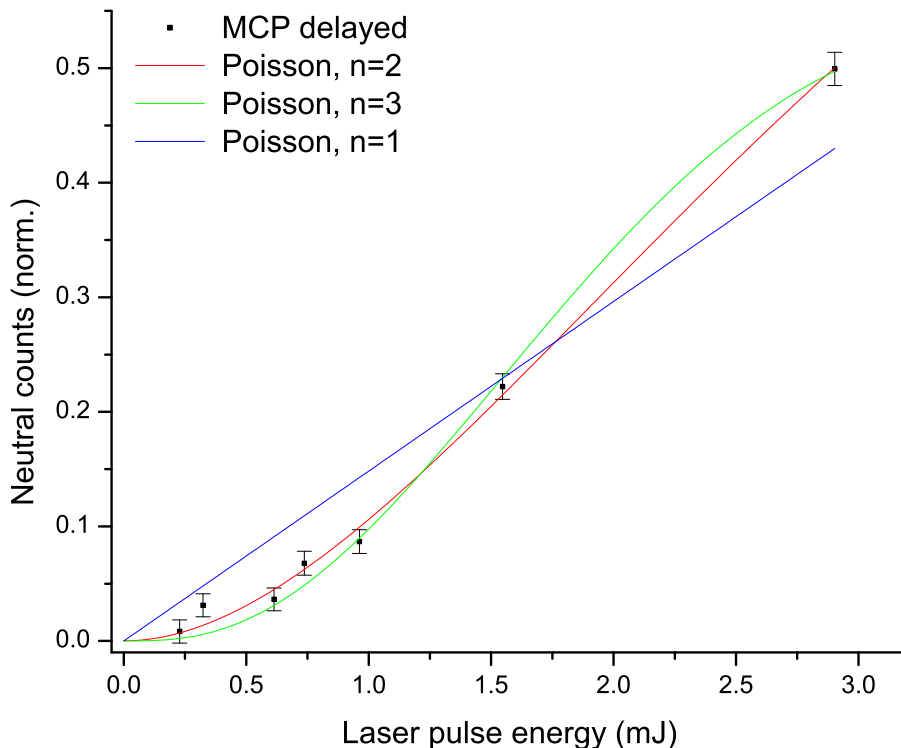


Figure 6.12: Determination of the absorption order of delayed action upon photoexcitation of $\text{H}_4\text{Pyrene}^{+\bullet}$ at 630 nm.

of the yield at especially very low laser pulse energies. As an example, in figure 6.12 the fits with $n=2$ and $n=3$ reproduce the data equally well. In the following treatment of the action absorption cross section, a two photon absorption process will be assumed although the absorption order might be higher at some laser pulse energies.

Absorption of the pyrene radical cation

Figures 6.13 and 6.14 show the action absorption profiles of $\text{Pyrene}^{+\bullet}$ (Sigma Aldrich, mass 202 amu, purity 98%) from the prompt and delayed action, respectively. In the figures, the absorption maximum is indicated with a vertical line. The absorption maximum is estimated to lie at 453 nm for the prompt action and at 436 nm for the delayed action. The peak for the delayed action is significantly broader than for the prompt action. To understand this, it is important to remember

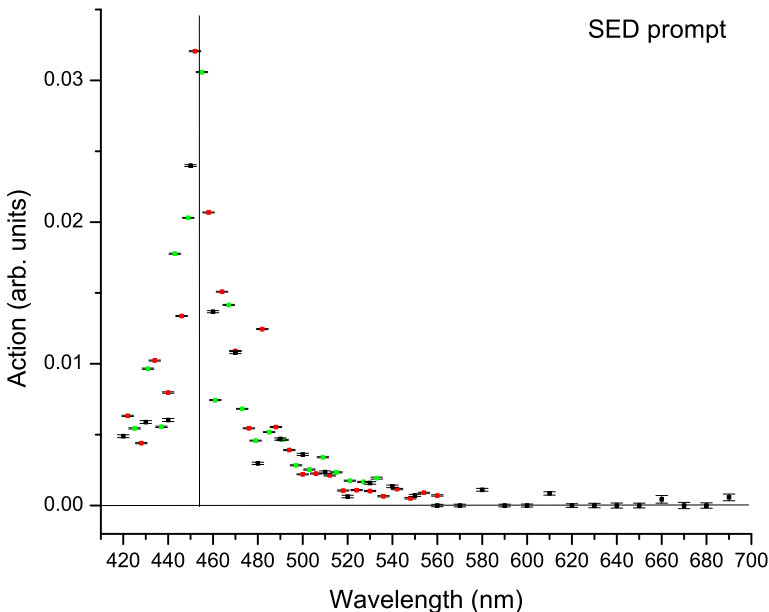


Figure 6.13: Absorption profile of the prompt action of $\text{Pyrene}^{+\bullet}$. The absorption maximum is estimated to lie at 453 nm and is indicated by the vertical black line. The different coloured data points (red, green, and black) represent independent wavelength scans.

that the prompt action includes all neutral fragments created during the first $10 - 15 \mu\text{s}$ after photoexcitation. As mentioned above, the action is a consequence of multiphoton absorption. Therefore moving towards wavelengths with a higher cross section drastically increases the average energy absorbed by the molecules and hence the probability of them dissociating within the first $\sim 10 - 15 \mu\text{s}$. Whereas at lower cross sections, the molecules may still have absorbed enough photons to dissociate at some point thereby mainly contributing to the delayed action.

The laser pulse energy has not been kept constant in these measurements, but vary from $\sim 3 - 10 \text{ mJ}$. From $420 - 550 \text{ nm}$, the laser pulse energy is above 7 mJ and peak around 445 nm . These high laser pulse energies also result in an increase in the prompt signal as multiphoton processes become more dominant. The narrower peak in the action absorption spectrum of the prompt action can therefore be explained by a higher multiphoton contribution. So, even though the cross section

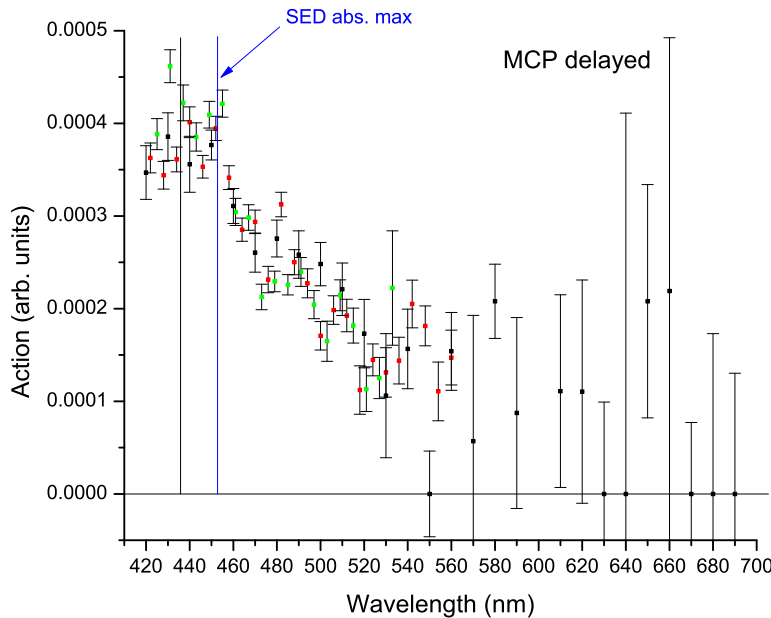


Figure 6.14: Absorption profile of the delayed action of Pyrene^{+•}. The absorption profile is broader around the maximum than for the prompt signal as the multiphoton contribution increases due to higher laser pulse energies in this region and the high absorption cross section. The absorption maximum is indicated by the vertical black line and the maximum obtained from the prompt spectrum is indicated by the vertical blue line. The different coloured data points (red, green, and black) represent independent wavelength scans. The large error bars at long wavelengths are due to poor statistics.

does have a maximum here as confirmed by the delayed action absorption spectrum, the height of the peak in the prompt spectrum cannot be used to make any conclusions.

The action absorption spectra of Pyrene^{+•} is in agreement with a multiphoton dissociation spectrum obtained by F. Useli-Bacchitta *et al.* [62]. In their spectrum, the absorption starts at ~ 460 nm and has a broad feature which falls off at 430 nm. The feature includes three peaks at 436 nm, 444 nm, and 450 nm. The 436 nm peak is ascribed to the $0 \rightarrow 0$ transition and the others to hot bands.

The calculations show that the charge is not located on a single carbon atom, but is not surprisingly distributed over the entire molecule.

The molecule carries a high degree of symmetry and this is also reflected in the charge distribution. The positive charge is mainly located on the four carbon atoms at the "corners" of the fusions.

The TD-DFT calculation gives a strong transition at 410 nm in agreement with the results given in [62]. This is the fifth electronic transition. A weaker transition is calculated to lie at 453 nm with an oscillator strength 20 times lower than the transition at 410 nm. F. Useli-Bacchitta *et al.* claims that the strong transition correlates with the experimental absorption peak. The calculated transition at 453 nm could then give rise to the tail into the red of the measured action absorption spectrum.

Absorption of the tetrahydropyrene radical cation

Figures 6.15 and 6.16 show the prompt and delayed action absorption spectra of $\text{H}_4\text{Pyrene}^{+\bullet}$ (TCI, mass 206 amu, purity > 98%). These spectra have been recorded with laser pulse energies of $\sim 3 - 10$ mJ. At a

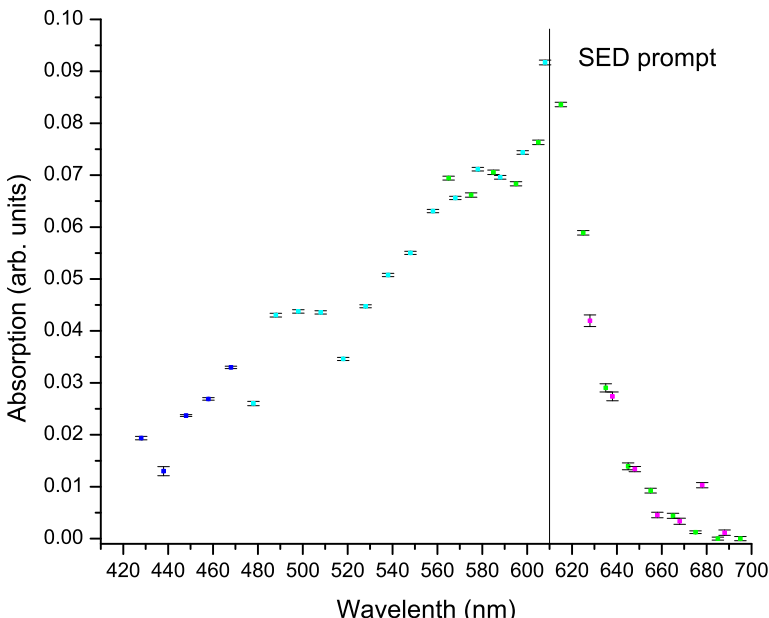


Figure 6.15: Absorption profile of the prompt action of $\text{H}_4\text{Pyrene}^{+\bullet}$. The maximum is estimated to lie at ~ 610 nm and is indicated by the black vertical line. The different coloured data points (red, green, and blue) represent independent wavelength scans.

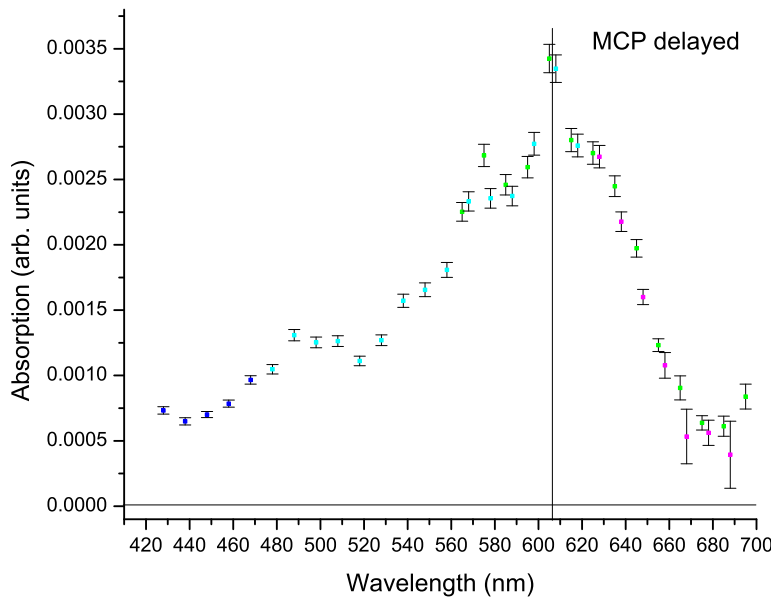


Figure 6.16: Absorption profile of the delayed action of H₄Pyrene⁺•. The maximum is estimated to lie at ~ 610 nm and is indicated by the black vertical line. The different coloured data points (red, green, and blue) represent independent wavelength scans.

first glance, the two spectra show great resemblance. The wavelength of the absorption maximum is estimated to 610 nm from the prompt spectrum and 608 nm from the delayed spectrum. The maximum is indicated by a vertical line in the figures. With the accuracy of these measurements, the determination cannot be expected to be more precise than a few nm. The absorption profile is very broad – action is observed from 420 nm in the blue region to 660 nm in the orange/red region.

However, there are some structural differences in the two spectra. In the delayed spectrum, a shoulder to the red of the absorption maximum is observed which is not observed in the prompt spectrum, where the rise to the absorption maximum is steeper. This may again be explained by a higher contribution to multiphoton processes around the absorption maximum. There is, however, no peak in the laser pulse energy in this region. At longer wavelengths, the lifetime of the molecule will be longer giving a higher contribution to the decay action than to the prompt action. On the blue side of the absorption profile, two shoulders

at ~ 575 nm and ~ 490 nm are visible in both absorption spectra. These features are likely to originate from a particularly good Franck-Condon overlap of vibrational states involved in the electronic transition.

There are two different isomers of tetrahydropyrene. The difference lies in the position of the hydrogenated carbon atoms and the energy difference is only 0.1 eV. The two aromatic benzene rings of the molecule are connected through (in the simple picture) a single bond. The angle between these rings is different for the two isomers and this difference can lead to a shift in the excitation energy of electronic transitions. Both the HOMO (highest occupied molecular orbital) and LUMO (lowest unoccupied molecular orbital) are nearly identical for the two isomers. Compared to Pyrene $^{+\bullet}$, the charge is more equally distributed over the entire molecule in the case of H₄Pyrene $^{+\bullet}$. The positive charge is mainly placed on the two central carbon atoms of the ring fusions and the hydrogen atoms on the hydrogenated carbon atoms sticking out of the main molecular plane.

According to the calculations, two electronic transitions with low or zero oscillator strength lie in the near IR region (1017 – 1250 nm) for both isomers. The third electronic transition has an oscillator strength two orders of magnitude higher than the previous. This transition involves the same orbitals for the two isomers and has an energy of 2.26 eV (549 nm) for the lowest energy isomer and 2.34 eV (531 nm) for the other. As mentioned, the aromatic part of the molecule resembles the biphenyl molecule (two benzene rings connected by a single bond). The two isomers of tetrahydropyrene have different angles between the two aromatic rings giving two different isomers of biphenyl. The orbitals of the first bright transitions are located on the biphenyl part of the molecule. TD-DFT calculations of the two biphenyl isomers give the exact same transitions as for tetrahydropyrene: The same ratio of oscillator strengths, the same orbitals involved in the transitions, and the same energy shift from one isomer to the other.

The experimental maximum was estimated to ~ 610 nm (2.03 eV). The absorption maximum cannot be directly compared to the calculated transition energies, as the maximum of the absorption profile corresponds to the best Franck-Condon overlap while the calculated transition energy corresponds to the vertical excitation energy. The vertical excitation energy is most likely found in the experimental spectrum to the red of the absorption maximum. The calculations and experimental determination differ by ~ 0.4 eV. The accuracy both of the calculations

as well as the estimates of the vertical excitation energy from the experimental data must be taken into account when comparing the two results.

Absorption of the hexahydropyrene radical cation

The absorption profiles of $\text{H}_6\text{Pyrene}^{+\bullet}$ (Sigma Aldrich, mass 208 amu, purity > 96,5%) are shown in figures 6.17 and 6.18. For these two spectra, the laser pulse energy has been kept constant at 5 mJ at 440 – 530 nm (red data points) and 3.4 mJ at 490 – 600 nm (green data points). The fact that the two wavelength regions overlap enables us to match the two scans, and the data has been scaled to do so. It was not possible to keep the laser pulse energy constant in the whole region as the appropriate filters were not available. Note that the absorption has only been measured from 440 – 600 nm in order to have sufficient laser pulse

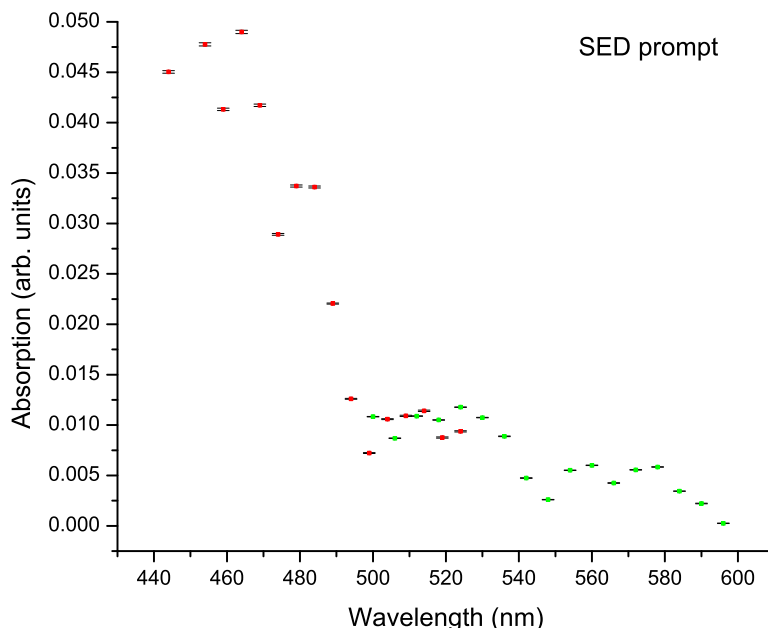


Figure 6.17: Absorption profile of the prompt action of $\text{H}_6\text{Pyrene}^{+\bullet}$. Three absorption features are observed in the spectrum with maxima at around 460 nm, 520 nm, and 575 nm. The laser pulse energy has been kept constant at 3.4 mJ (green data points) and at 5 mJ (red data points) during the experiment.

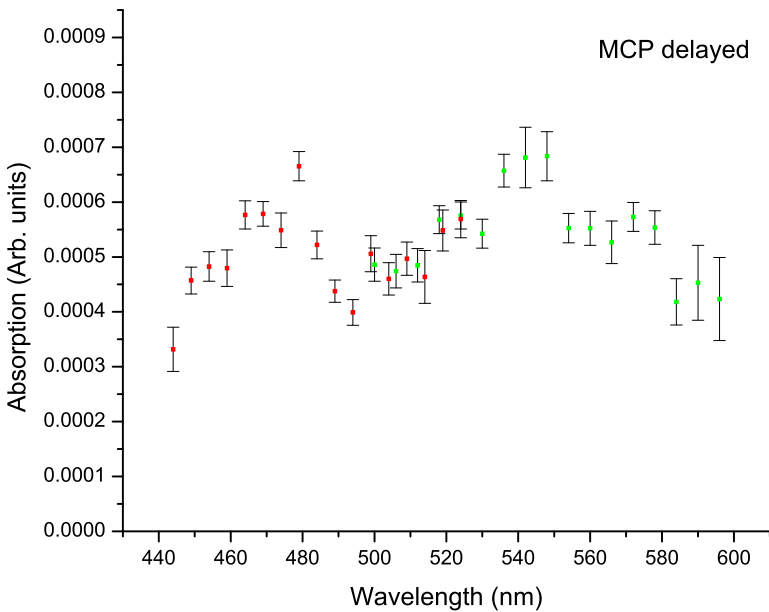


Figure 6.18: Absorption profile of the delayed action of $\text{H}_6\text{Pyrene}^{+\bullet}$. Only two absorption features are observed at 470 nm and 540 nm, respectively. The laser pulse energy has been kept constant at 3.4 mJ (green data points) and at 5 mJ (red data points) during the experiment.

energy to obtain a reasonable dissociation yield.

The prompt and delayed action spectra look very different. The prompt spectrum has a high peak at ~ 460 nm and two smaller ones at ~ 520 nm and ~ 575 nm. The delayed spectrum shows two equally high peaks at ~ 470 nm and ~ 540 nm. The delayed peak at 470 nm is approximately symmetric around the absorption maximum. The prompt peak at ~ 460 nm does not fall dramatically off towards the blue wavelengths. However, this is close to the edge of the investigated wavelength range, which makes it hard to make definite conclusions. The two lower peaks in the prompt spectrum are not recognised in the delayed spectrum. If the three points around 540 nm were ignored in the delayed spectrum, the two peaks in the delayed spectrum may be seen at 525 nm and 570 nm in the delayed spectrum. More and careful measurements in this region are necessary in order to confirm this claim.

The numerical optimisation of the molecular structure reveals two isomers of hexahydropyrene with nearly identical ground state ener-

gies (a difference of 0.002 eV is within the accuracy of the computational method). Both isomers contain a flat molecular plane consisting of the aromatic, naphthalene skeleton of the molecule and the four hydrogenated carbon atoms nearest to the ring fusions. The two centre carbon atoms of the hydrogenated rings either point in the same or opposite direction with relative the molecular plane. In both cases, the positive charge is mainly located on the hydrogen atoms of the hydrogenated rings. The naphthalene skeleton is approximately neutral.

The calculated electronic transition energies do not match the experimental absorption spectrum. The first transition is a dark state. The second transition has an energy corresponding to 688 nm and 690 nm for the two isomers, which is the same energy with the accuracy of the calculations. The electron density is not relocated in the transition, and the transition mainly has $\pi\pi^*$ -character. The same trend is seen for the next transition. This transition lies at 365 nm for both isomers and has an oscillator strength 10 times higher than the previous. The transition does not possess charge-transfer character and TD-DFT calculations for this kind of transitions are the most inaccurate. There is in general some uncertainty regarding the precision of the TD-DFT calculations. With this in mind, it can be speculated that the calculated excitation energy corresponding to ~ 689 nm can be ascribed to the features in the 510 – 590 nm region of the experimental spectra and the calculated excitation energy of ~ 365 nm can be ascribed to the prominent peak at ~ 460 nm. It should also be remembered that the absorption spectrum was only measured up to 600 nm. More experiments and higher level calculations must be done to investigate these speculations.

TD-DFT calculations have been carried out for both cationic and neutral naphthalene. The transitions of cationic naphthalene resemble the transitions of $\text{H}_6\text{Pyrene}^{+\bullet}$ very well. The first state is a dark state, and the second involves the same orbitals as the second transition of $\text{H}_6\text{Pyrene}^{+\bullet}$. Even though the charge of $\text{H}_6\text{Pyrene}^{+\bullet}$ is located on the peripheral hydrogen atoms, cationic naphthalene resembles the electronic transitions better than neutral naphthalene. The charge on the naphthalene cation is also mainly located on the peripheral hydrogen atoms and the skeleton is approximately neutral. The excitation energies (578 nm and 414 nm for the second and third transition) of cationic naphthalene actually match the experimental values better than the calculated energies for $\text{H}_6\text{Pyrene}^{+\bullet}$. The accuracy of the calculations can be doubted and a more thorough computational study may give values

that are in better agreement with the experimental results.

Hexahydropyrene has been studied previously [159, 160]. A. Chakraborty *et al.* [159] show that neutral hexahydropyrene fluoresces at ~ 350 nm with a lifetime of 18 ns and phosphoresces at > 490 nm with a lifetime of 45 ms in low temperature cyclohexane glass. These measurements were not done on the cationic form of hexahydropyrene and therefore the results cannot be directly compared. However, the lifetimes are worth noticing: the molecule will fluoresce before dissociation can be monitored at ELISA, and if the molecule is trapped in a triplet state dissociation is again not possible to detect.

Comparison

The three radical cations all have absorption features in the visible region, but show a large variation in position and height of these features. The absorption features are all very wide. The aromatic part of the molecules can be considered as boxes. In the quantum mechanical description of an electron in a box, the spacing of the energy levels decreases with increasing box area resulting in red shifting of the elec-

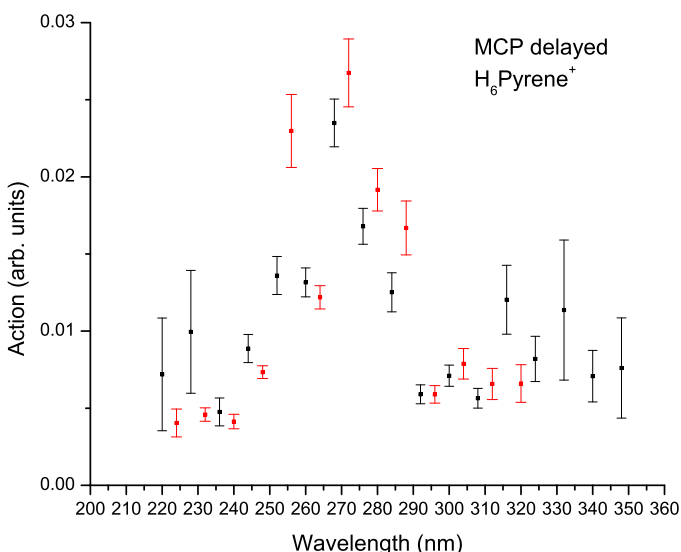


Figure 6.19: Action absorption spectrum of $\text{H}_6\text{Pyrene}^{+\bullet}$ in the UV spectral range. The different coloured data points (red and black) represent independent wavelength scans.

tronic transitions. Hence, the absorption might have been expected to shift towards more blue wavelengths when decreasing the area of the aromatic part of the molecule. However, this is not what is observed experimentally. The absorption maximum of $\text{H}_4\text{Pyrene}^{+\bullet}$ has the lowest transition energy (~ 610 nm). The absorption maximum of $\text{Pyrene}^{+\bullet}$ (which has the largest aromatic area) lies at ~ 445 nm. The absorption maximum for $\text{H}_6\text{Pyrene}^{+\bullet}$ is also shifted to the red compared to $\text{Pyrene}^{+\bullet}$. This shows that the simple "particle-in-a-box" picture cannot describe the difference in the experimentally determined absorption maxima – under the assumption that no transitions are shifted to higher wavelengths than 700 nm.

Scout measurements were performed from 210 to 300 nm on all three radical cations. Figure 6.19 shows as an example of the UV absorption, the delayed action absorption spectrum of $\text{H}_6\text{Pyrene}^{+\bullet}$ monitored by the MCP detector. The spectrum is constructed from two wavelength scans with 10 nm steps displaced by 5 nm. Both scans indicate an absorption maximum at ~ 270 nm. The measurements on $\text{Pyrene}^{+\bullet}$ suggest an absorption maximum at 240 nm. $\text{H}_4\text{Pyrene}^{+\bullet}$ also has absorption in this region, but no clear maximum is seen in the spectrum. The yield of neutral fragments created upon photoexcitation in this region is very low and the measurements are therefore very cumbersome also indicated by the big error bars in figure 6.19. The scout measurements encourage further experimental work in this spectral region as the UV absorption and dissociation pattern is of great astrophysical interest.

Dissociation channels

Figures 6.20, 6.21, and 6.22 show the masses of the charged dissociation products created upon photoexcitation of $\text{Pyrene}^{+\bullet}$, $\text{H}_4\text{Pyrene}^{+\bullet}$, and $\text{H}_6\text{Pyrene}^{+\bullet}$, respectively, by photons in the visible region. The masses on the axes are the direct readouts from the experiment. These must be scaled according to a known fragment. As the masses of the fragments are not known from other experiments, this has *not* been done for the mass spectra presented here. The correct scaling may change the masses by $\sim 1\%$ corresponding to the masses here being off by ~ 2 amu.

The mass spectrum in figure 6.20 of the charged dissociation products of $\text{Pyrene}^{+\bullet}$ show two prominent features. One is centered around $m=172$ amu and the other around $m=186$ amu. The mass of $\text{Pyrene}^{+\bullet}$

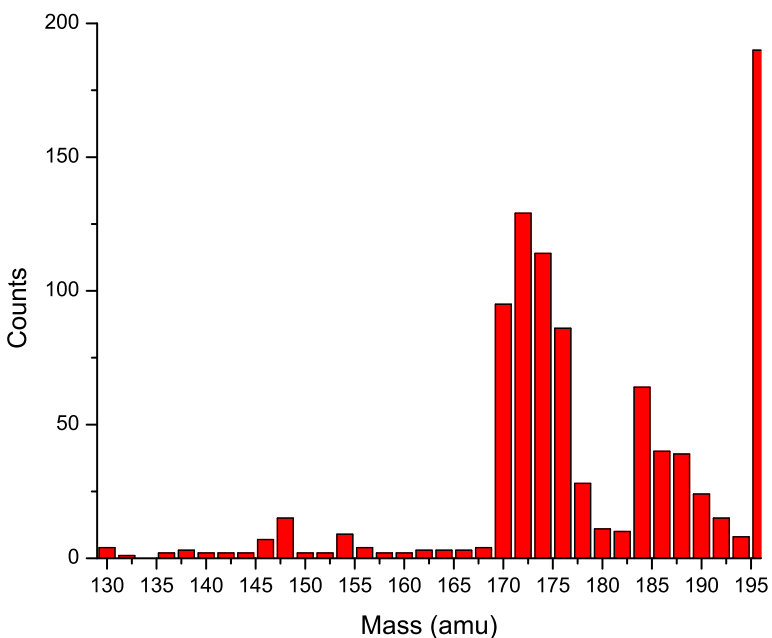


Figure 6.20: Charged dissociation products created upon photo-excitation of $\text{Pyrene}^{+\bullet}$ by 450 nm photons. The masses have not been scaled. The two peaks probably correspond to loss of one and two carbon atoms, and a number of hydrogen atoms. The high yield at mass 196 amu stems from the tail of the mother ion.

is 202 amu. Loss of a single carbon atom would result in a charged fragment with mass 190 amu and two carbon atoms in mass 178 amu. The two observed peaks are probably loss of one and two carbon atoms along with a number of hydrogen atoms. The high yield at mass 196 amu stems from the tail of the mother ion. Loss of either atomic or molecular hydrogen would result in charged fragments with masses too close to the mother ion to be able to observe them with this technique.

Loss of one and two carbon atoms and a number of hydrogen atoms is also observed for $\text{H}_4\text{Pyrene}^{+\bullet}$ along with loss of three carbon and a number of hydrogen atoms at both 450 and 600 nm, see figure 6.21. The peaks are centred around $m=161$ amu, $m=175$ amu, and $m=189$ amu. Loss of one, two, and three carbon atoms result in charged fragments with masses of 194 amu, 182 amu, and 170 amu. Again, loss of atomic and molecular hydrogen cannot be observed. The yield of the charged

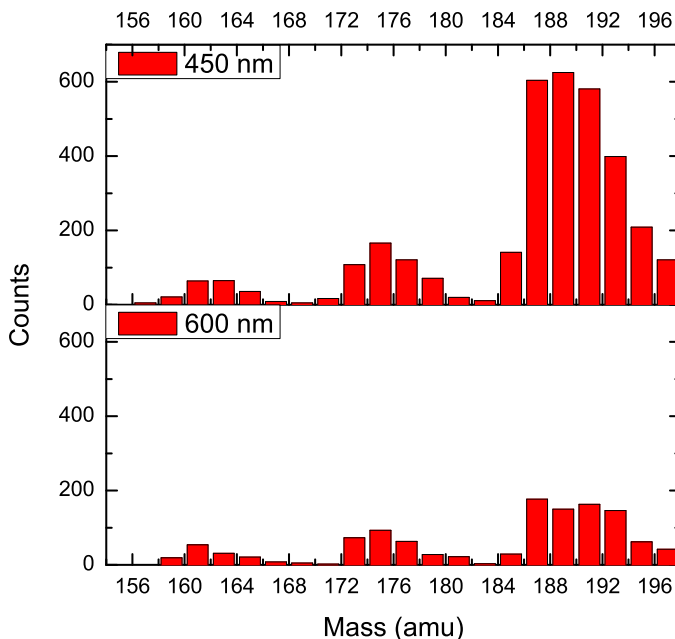


Figure 6.21: Charged dissociation products created upon photo-excitation of $\text{H}_4\text{Pyrene}^{+\bullet}$ by 450 and 600 nm photons. The masses have not been scaled. The three peaks probably correspond to loss of one, two, and three carbon atoms, respectively, and a number of hydrogen atoms.

fragment is lower at 600 nm than at 450 nm even though the observed action absorption maximum is located close to 600 nm. The barrier for loss of carbon atoms is expected to be higher than loss of atomic and molecular hydrogen. Since the 450 nm photons are more energetic than the 600 nm, absorption of these leads to warmer molecules (higher vibrationally excited in the electronic ground state) and, hence, larger probability of carbon loss. This probably explains the larger yield observed here at 450 nm even though the absorption cross section is smaller (as seen from figures 6.15 and 6.16).

Similar trends are seen for $\text{H}_6\text{Pyrene}^{+\bullet}$, see figure 6.22. Again, up to loss of three carbon atoms and a number of hydrogen atoms is observed with photon energies corresponding to 480 and 550 nm. The peaks are centred at mass 162 amu, 174 amu, and 192 amu. The charged fragments will have masses of 172 amu, 184 amu, and 196 amu with a mother ion of mass 208 amu. The yield of charged fragments is again

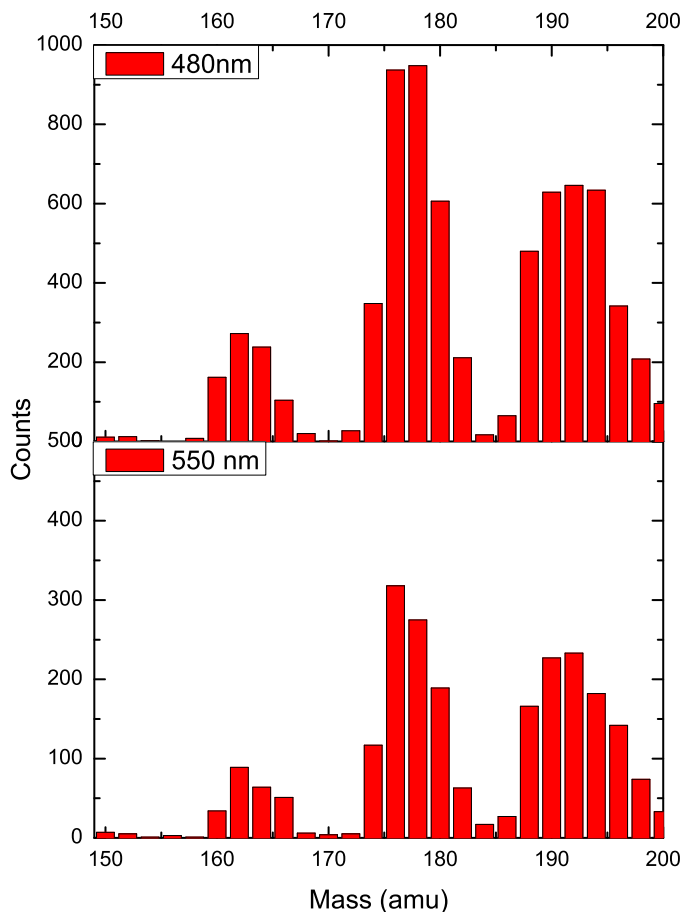


Figure 6.22: Charged dissociation products created upon photoexcitation of $\text{H}_6\text{Pyrene}^{+\bullet}$ by 480 and 550 nm photons. The masses have not been scaled. The three peaks probably correspond to loss of one, two, and three carbon atoms, respectively, and a number of hydrogen atoms.

considerably lower at 550 nm than at 480 nm as was also the case for $\text{H}_4\text{Pyrene}^{+\bullet}$. The same explanation as given above is expected to be the cause of this, even though the absorption is a bit higher at 550 nm.

DFT calculations were performed to investigate the potential energy surfaces of the dissociation pathways of $\text{H}_4\text{Pyrene}^{+\bullet}$. Unfortunately, not all structures were successfully optimised to a local minimum and only calculations to create the potential energy surface for H_2 loss were completed. H_2 is emitted from one of the hydrogenated

carbon atoms, and after which the extra hydrogen atom of the adjacent hydrogenated carbon atom moves to the emission site. The result is a hydrogen molecule and a dihydropyrene cation ($\text{H}_2\text{Pyrene}^{+\bullet}$) consisting of three aromatic rings and a single hydrogenated ring. The highest barrier of this dissociation pathway is the relocation of the hydrogen atom of the adjacent hydrogenated carbon atom. This barrier is 4.2 eV relative to the initial structure. The end complex of dihydropyrene and H_2 has a relative energy of 1.1 eV.

The dissociation channels have been studied both experimentally and theoretically by several groups [88, 116–122] as mentioned in section 5.2. Experimental results of keV ion impact on neutral PAHs show that fragments C_nH_x with n up to nine are generated. The theoretical results show that C_2H_2 is the lowest energy channel with an adiabatic dissociation energy of $\sim 3 - 4.5$ eV for smaller PAHs and 7.3 eV for coronene.

6.3.3 Summary

The action absorption spectra of the radical cations of pyrene, tetrahydropyrene and hexahydropyrene were measured in the visible region. All three molecules dissociate upon photoexcitation and the charged daughter masses monitored show rich dissociation patterns. The fragments seem to consist of 1 – 3 carbon atoms and a number of hydrogen atoms. The technique cannot resolve the masses to obtain a more precise determination as well as monitor fragments after loss of only atomic or molecular hydrogen – both dissociation channels are expected to be open. The dissociation has prominent prompt and delayed components and both channels are determined to have multiphoton contribution. The exact order of absorption is, however, hard to determine.

These preliminary results give a good basis for further spectroscopic investigations of hydrogenation states of pyrene. The production method showed to be very efficient and enabled production of sufficient amounts of ions for experiments at ELISA. Other PAH radical cations with the appropriate ionisation potential are expected to be formed using this method. The dissociation pattern sheds light on the possible components of the interstellar medium. The action absorption spectra recorded in the visible spectral range ask for further experimental and computational studies under more astrophysical relevant conditions.

6.3.4 Mass 205 and 207 amu

One of the strengths of ELISA is the separator magnet placed in the injection beam line. As described above, this makes it possible to choose a specific mass over charge for the experiment. In order to be able to identify the desired ion, a good calibration of the magnet is needed. During the experiments of this study, two ions extensively studied at ELISA were used to calibrate the magnet as the mass spectrum of these samples are well known. These two ions are the chromophore of the green fluorescence protein [161] and the retinal chromophore [162]. They both contain a nitrogen atom with an electron lonepair, hence protonation of the molecules is very easy. The unforeseen complication of the cali-

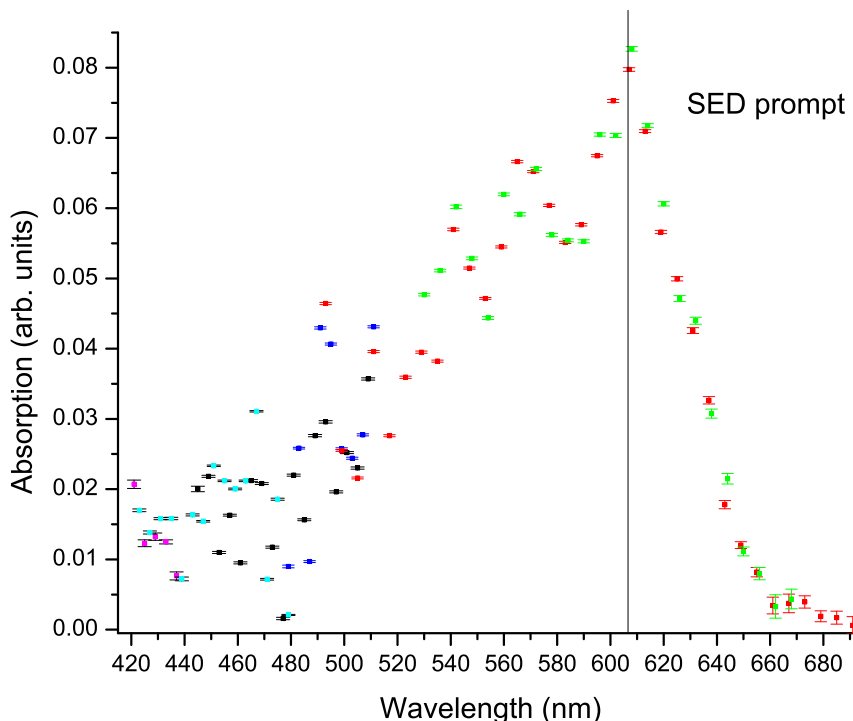


Figure 6.23: Absorption profile of the prompt action of an ion with mass 205 amu when spraying tetrahydropyrene. The absorption maximum is estimated to lie at 608 nm and is indicated by the black vertical line. On the blue side of the maximum, features ascribed to good Franck-Condon overlap is observed. The different coloured data points (pink, blue, black, red, and green) represent independent wavelength scans.

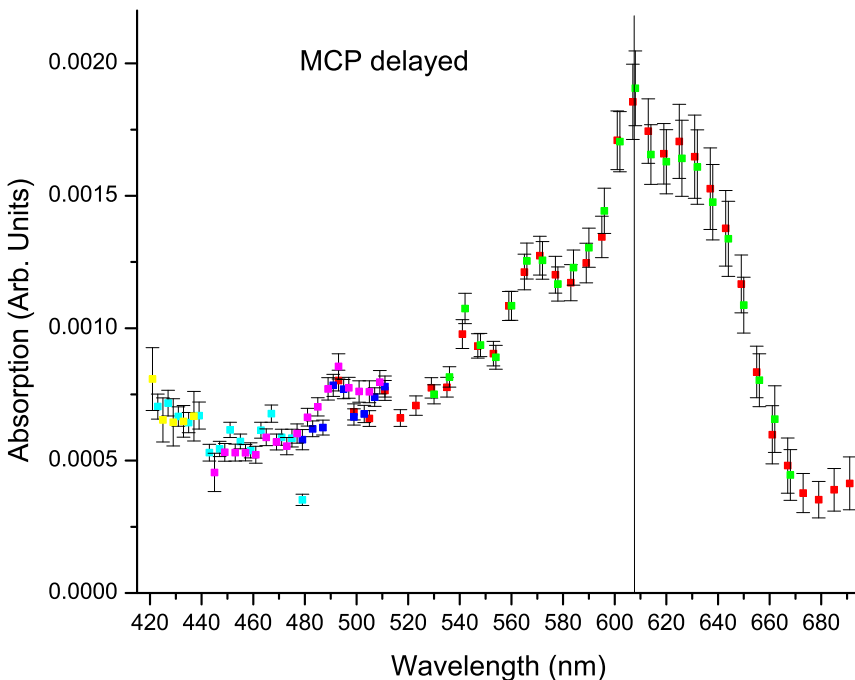


Figure 6.24: Absorption profile of the delayed action of an ion with mass 205 amu when spraying tetrahydropyrene. The absorption maximum is estimated to lie at 608 nm and is indicated by the black vertical line. A shoulder is present on the red side of the maximum. On the blue side of the maximum, features ascribed to good Franck-Condon overlap is observed. The different coloured data points (yellow, turquoise, blue, pink, and green) represent independent wavelength scans.

bration was the production of the radical cation of both species. The ratio between the radical cation and the protonated cation showed to be highly dependent on the voltage applied to the needle of the electrospray ion source. The incorrect magnetic fields of the calibration resulted in absorption spectra of ions with a mass of 205 amu when spraying the sample of tetrahydropyrene and 207 amu when spraying the sample of hexahydropyrene – one amu below the correct masses. These spectra are shown in figures 6.23–6.26.

Figures 6.23 and 6.24 show the prompt and delayed action absorption spectra of an ion with mass 205 amu from spraying tetrahydropyrene. Both spectra indicate an absorption maximum at ~ 608 nm. The slope on the red side of the maximum is steeper in the prompt spectrum

than in the delayed, where a shoulder is visible. Both spectra show more or less pronounced features towards the blue wavelengths (565 nm, 540 nm, and 490 nm), which can be interpreted as Franck-Condon structures. The absorption maximum lies close to the absorption maximum of $\text{H}_4\text{Pyrene}^{+\bullet}$ (~ 610 nm). Two of the the Franck-Condon structures in these measurements are also seen for $\text{H}_4\text{Pyrene}^{+\bullet}$ spectrum (~ 490 nm and ~ 565 nm), while the feature at 540 nm is not.

There are two possible explanations of the appearance of an ion with mass 205 amu from the sample of tetrahydropyrene (mass 206 amu). As was seen in the case of protonated quinoline (see section 6.2.1), dehydrogenated species can be formed during the electrospray ionisation process. Loss of a single hydrogen atom from tetrahydropyrene results in an ion with mass 205 amu. The other possibility origins in the electrospray ion source having a kind of "sample memory". Some of the sample being sprayed may condense in the capillary going from the syringe to the needle, and ions from the remnants may be seen up to weeks after. During the weeks of the experiments on hydrogenated pyrene cations, the samples of pyrene, tetrahydropyrene, and hexahydropyrene were interchanged several times. Hence, the mass at 205 amu may originate from either of the three samples. Tetrahydropyrene and hexahydropyrene may have been dehydrogenated. A study of electrospray ionisation of pyrene with a purity of 98% by M. Vala *et al.* [89] show that even with a high purity, the impurity of nitrogen substituted pyrene (azapyrene) with a much higher proton affinity than pyrene gives a yield 50 times as high as protonated pyrene. Protonated azapyrene has a mass of 204 amu. Therefore, singly hydrogenated protonated azapyrene would result in mass 205 amu and hence could the observed ion considering the results of hydrogenation of quinoline (figure 6.2). Nevertheless, since the spectra for the 205 amu ion mostly resemble the $\text{H}_4\text{Pyrene}^{+\bullet}$ spectra, the first explanation is believed to be the most plausible.

Figures 6.25 and 6.26 show the prompt and delayed action absorption spectra of an ion with mass 207 amu from spraying hexahydropyrene. Both the prompt and delayed spectrum suggest an absorption maximum at ~ 545 nm. At shorter wavelengths, the prompt action indicates a small increase independently of the delayed action. This is most likely a consequence of an increase in the multiphoton contribution, as was also observed in some of the other action absorption spectra in this study. Similar to the 205 amu ion, the possible candidates for the

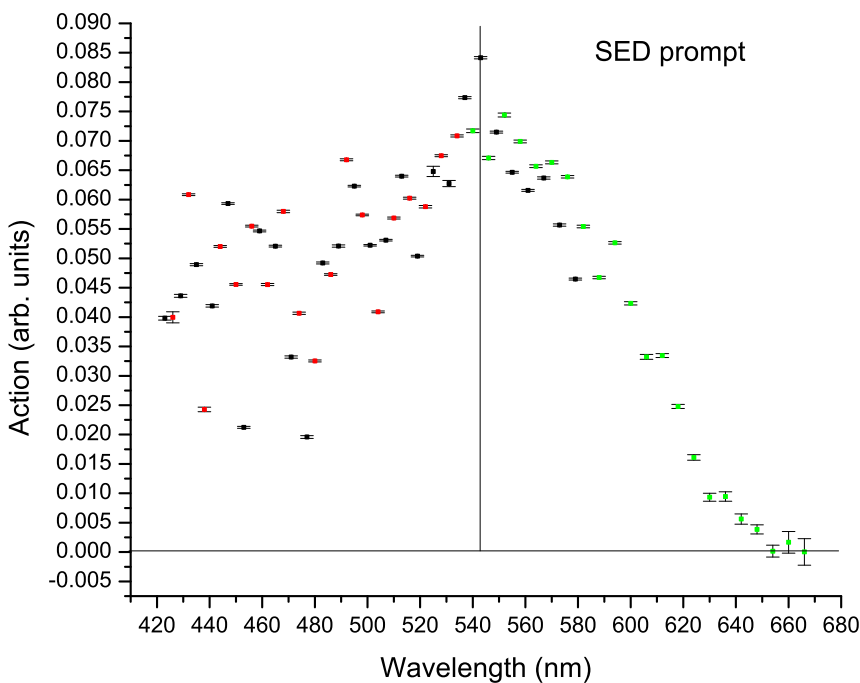


Figure 6.25: Absorption profile of the prompt action of an ion with mass 207 amu when spraying hexahydriopyrene. The absorption maximum is estimated to lie at ~ 540 nm and is indicated by the black vertical line. At shorter wavelengths and higher laser pulse energies, the prompt action increases. The different coloured data points (black, red, and green) represent independent wavelength scans.

207 amu ion are: Singly dehydrogenated hexahydriopyrene, singly hydrogenated tetrahydriopyrene, and triply hydrogenated azapyrene. In this case, there is no clear correlation with the absorption spectra of the hexapyrene radical cation.

The TD-DFT calculations carried out did not give any conclusions in the determination of the molecular origin. The identification of mass 205 amu and 207 amu requires other experiments, careful measurements and a bigger computational search.

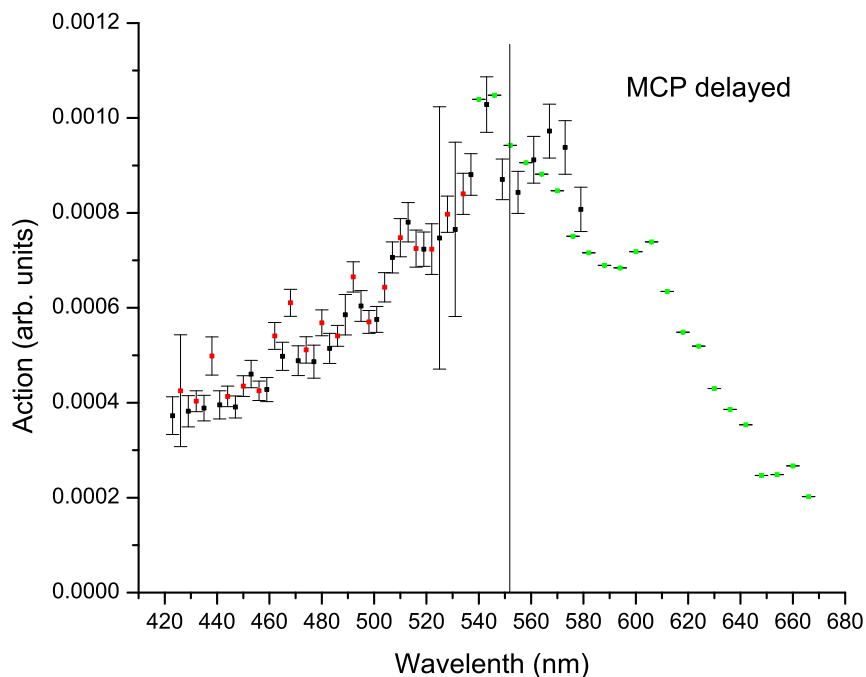


Figure 6.26: Absorption profile of the prompt action of an ion with mass 207 amu when spraying hexahydriopyrene. The absorption maximum is estimated to lie at ~ 550 nm and is indicated by the black vertical line. At shorter wavelengths and higher laser pulse energies, the delayed action decreases compared to the prompt action. The different coloured data points (black, red, and green) represent independent wavelength scans.

6.4 Summary and outlook

In the previous two sections, experimental results for hydrogenated PAHs were presented and discussed. The results show that hydrogenated PAHs can be formed under very different conditions and that they undergo dissociation upon photoexcitation in both in the visible and the UV region. Several visible photons are needed to dissociate the PAHs, but the molecules can still absorb a single photon and thereby cause absorption lines in the interstellar spectra. In that case, the energy is probably re-emitted as IR photons. The dissociation products also give insight into other possible components of the ISM. The results can be used to initiate further experimental and computational studies of this class of astrophysical relevant molecules. Several steps towards new experiments have already been taken in Aarhus.

A 1x1 m electrostatic storage ring named SAPHIRA has been installed at the so-called Separator II facility under Professor Lars H. Andersen. Here, the injection beam line is nearly identical to that of ELISA and also has the capability of installing different ion sources. Experiments similar to the ones being done at ELISA can be performed at SAPHIRA, but the smaller circumference makes it possible to monitor shorter time scale. One of the main purposes of installing this ring, is the possibility of doing time resolved mass spectrometry with a resolution better than 1 amu. This is enabled by a pick-up system built into the ring. At present, the effort in the laboratory is focused on storing an ion beam in the ring. A tuneable laser is also available at the facility. With this setup, it will be possible to obtain mass spectra of the charged dissociation products upon photoexcitation with the possibility of distinguishing different hydrogenated states of the dissociation products. This will give a clearer picture of the dissociation pattern of photoexcited hydrogenated PAHs.

Another addition to the Separator II facility is a fragment analyser placed in extension to the injection beam line. Ions generated in the ion source are irradiated by a laser pulse and both neutral and charged dissociation products move in the same direction as of the mother ion. The fragment analyser consists of a quadrupole deflector and by tuning the voltages of the electrodes, ions with a specific mass will be deflected towards a channeltron detector placed ~ 1 m from the deflector. Simulations of the trajectories of an ion with mass 200 amu show that the resolution is better than 1 amu, making it possible to distinguish loss of

1 or 2 hydrogen atoms from e.g. hydrogenated pyrene.

The problem with both of the described techniques is that although they are able to distinguish between loss of 1 and 2 amu from the mother ion, they cannot tell whether a loss of two mass units stems from loss of two individual hydrogen atoms or a single hydrogen molecule. A technique that can monitor the neutral fragments is needed to answer this essential question.

A facility under Associate Professor Liv Hornekær has the ability to do this. In a chamber of ultra high vacuum a gas of sample PAH molecules (e.g. coronene) is damped onto a graphite substrate to form either mono- or multilayers of PAHs depending on the dosing time. The type of layer can be determined using the technique of temperature programmed desorption (TPD). Here, the substrate is slowly heated and molecules with different bindings to the substrate will have sufficient energy to leave at different temperatures. The molecules are detected using a mass filter. By exposing the PAHs to a deuterium gas, the PAHs will become deuterated (hydrogenated). The degree of deuteration can also be determined by TPD. With this technique, the group of Liv Hornekær have proven that PAHs can exist in many different hydrogenated states on a substrate [145].

The tuneable EKSPLA laser was moved to this facility and a deuterated coronene sample was irradiated with UV photons. The mass filter was moved as close as possible to the sample during irradiation to detect photofragments. After irradiation, TPD was applied to the sample to identify any change upon irradiation. Neither any photofragments nor any change in the TPD spectrum was observed upon irradiation of the sample. It could in fact be that no changes occur to the sample but it could also be that the experiment itself does not monitor the effect.

There are several factors complicating the experiments, which have to be considered before repeating them. The absorption spectra of different hydrogenation states of coronene are unknown and the experiment is complicated by this. These could either be computed using TD-DFT (with the errors of the method in mind) or be obtained experimentally. ELISA is no help for this, as only action absorption spectra of ions can be measured. When monitoring changes after UV irradiation of the sample, the TPD spectrum is compared to spectra measured without irradiating the sample. The sample must be carefully prepared; first by dosing the sample, then by dosing of deuterium onto the sample. The repetition from sample to sample of the thickness of the dosed

PAH and the degree of deuteration requires experience and time. The experience and excellence of the group under Liv Hornekær is essential in these experiments, but small changes e.g. in the position of the doser complicates a uniform preparation of the samples. With more time and some luck these experiments could provide important information on the production of H₂ with hydrogenated PAHs as catalysts.

With reference to the unsolved mystery of the diffuse interstellar bands, more experiments are needed to clarify whether hydrogenated PAH cations contribute to these interstellar absorption features or not. The preliminary results on hydrogenated pyrene radical cations suggest that the photophysical properties of a molecule are very dependent on the degree of hydrogenation. As all three molecules show absorption in the visible, further experiments with better resolution than obtained with hot molecules are likely to supply the astronomers with conclusive results to compare with their observational spectra and to verify the proposal of hydrogenated PAHs being the carriers of the DIBs.

CHAPTER 7

Summary

Polycyclic aromatic hydrocarbons (PAHs) are unambiguous and ubiquitous components of the interstellar medium of the Milky Way and other galaxies. The PAH family is identified through the frequencies of their characteristic vibrational modes and now give name to the aromatic infrared bands. The variation in the IR emission from photoexcited PAHs can be used to obtain important information on the physical and chemical conditions of different parts of the interstellar medium. PAHs play an important role in star formation and possibly also as catalysts in the formation of molecular hydrogen – the most abundant interstellar molecule.

PAHs are exposed to radiation in the interstellar medium, and the interaction between PAHs and photons is of great interest in order to understand the interstellar mechanisms. Electronic excitation by UV and visible photons makes the molecules very hot, and their excess energy can be emitted as IR photons. Another scenario is dissociation upon photoexcitation and understanding the competition between these two de-excitation channels is important to gain further insight into the interstellar medium. At the electrostatic storage ring, ELISA, this interaction has been studied for a number of PAHs:

Four isomers of a small nitrogen and methyl substituted PAH were excited by UV photons in the 215 – 338 nm spectral range. It is shown that the absorption profile is both red shifted and broadened when moving the methyl group from the heterocycle containing nitrogen to the homoatomic ring. The absorption profiles are understood by comparison with by TD-DFT calculations. The dissociation time of the stud-

ied molecules is found to be of several milliseconds at 230 nm, and it is shown that after redistribution of the absorbed energy the molecules dissociate through several different channels. The determined dissociation time is an order of magnitude shorter than the estimated IR relaxation time.

Hydrogenated PAHs were produced in two different ionisation processes, and the measured yield indicates high stability suggesting a high abundance in the interstellar medium. A clear pattern in the yield and binding energies of hydrogen is revealed. Hydrogenated closed shell molecules with an even number of attached hydrogen atoms are significantly more stable than molecules with an odd number of hydrogen atoms and show as a consequence to be more abundant in the mass spectra of H_n PAHs. The binding energy of a hydrogen atom to H_{n-1} PAH with an even n is ~ 2 eV higher than for odd n .

The photophysical properties of hydrogenated pyrenes have been investigated and the preliminary results show some interesting features. The molecules dissociate when absorbing more than one visible photon and again, a rich dissociation pattern is seen. The difference seen in the both measured and calculated absorption spectra for the three investigated molecules provides a tool for identifying different hydrogenation state of molecules.

This thesis presents important absorption spectra for the search for interstellar PAHs as well as information on other photophysical properties. The identification of dissociation products upon photoexcitation by photons both in the visible and UV spectral range give information on probable components of the interstellar medium.

CHAPTER 8

Dansk resumé

Polycykiske aromatiske kulbrinter (PAH'er) er kendte komponenter af det interstellare medium i Mælkevejen og i andre galakser. PAH familiens kan identificeres via frekvenserne af dens karakteristiske vibrationelle tilstande og har derfor lagt navn til de aromatiske infrarøde bånd. Variationer i det udsendte IR lys fra fotoexciterede PAH'er giver information om de fysiske og kemiske forhold i forskellige dele af det interstellare medium. PAH'er spiller en vigtig rolle i stjernedannelse og sandsynligvis også som katalysatorer i dannelsen af molekulært brint – det mest forekomne interstellare molekyle. Kendskab til PAH'ernes egenskaber er derfor vigtigt for at forstå mange processer i det interstellare medium.

PAH'er udsættes for stråling i det interstellare medium og vekselvirkningen mellem PAH'er og fotoner er derfor meget interessant. Elektronisk excitation med UV og synlige fotoner efterlader molekylerne meget varme, og den overskydende energien kan udsendes som IR fotoner. Et andet scenarie er dissociation efter excitation og konkurrencen mellem disse to kanaler er vigtig for videre processer. Denne vekselvirkning er studeret ved den elektrostatiske lagerring, ELISA:

Fire isomere af en lille nitrogen- og methylsubstitueret PAH blev exciteret af UV fotoner med bølgelængder i området 215 – 338 nm. Det er vist, at absorptionsprofilen rødkiftes og forbredes, når methylgruppen flyttes fra ringen indeholdende nitrogen til ringen udelukkende bestående af kulstof atomer. Absorptionsprofilen forklares ud fra TD-DFT beregninger. Dissociationstiden for de studerede molekyler ved 230 nm findes til at være adskellige millisekunder og det vises, at

molekyler-ne dissocierer via flere forskellige kanaler efter omfordeling af den absorberede energi. Dissociationstiden er en størrelsesorden kørtere end den estimerede IR relaksationstid.

Hydrogenerede PAH'er blev produceret i to forskellige ionisationsprocesser, og det målte udbytte fra ionkilderne indikerer en høj stabilitet, hvilket tyder på mulig høj forekomst i det interstellare medium. Der ses et klart mønster i udbyttet samt bindingsenergerne af hydrogen. Hydrogenerede, lukket-skal molekyler med et lige antal påsatte hydrogen atomer er betydeligt mere stabile end molekyler med et ulige antal påsatte hydrogen atomer og har derfor en større forekomst i massespektrene af H_nPAH . Bindingsenergien af et hydrogen atom til en $H_{n-1}PAH$ med et lige n er ~ 2 eV større end for ulige n . Den nøjagtige fordeling i n observeret i de eksperimentelle massespektre mangler stadig en forklaring, da de interne forhold i ionkilderne ikke kendes.

De fotofysiske egenskaber af hydrogenerede pyrener blev undersøgt, og de foreløbige resultater viser nogle interessante karakteristika. Molekyler-ne dissocierer ved absorption af mere end én foton i det synlige område og igen ses et rigt dissociationsmønster. Forskellen set i både de eksperimentelle og beregnede absorptionsspektre for de tre undersøgte mole-kyler giver et værkøj til identifikation af forskellige hydrogenerede tilstande af molekyler.

Denne afhandling præsenterer vigtige absorptionsspektre til søgen efter interstellare PAH'er samt information om andre fotofysiske egenskaber. Identifikationen af dissociationsprodukter dannet efter fotoexcitation af både synlige og UV fotoner giver information om mulige komponenter af det interstellare medium.

CHAPTER 9

Acknowledgements

First, I would like to thank my two dedicated supervisors, Lars and Liv, for giving me the opportunity to continue the work on gas phase PAHs I started during my bachelor project in the spring of 2008. As my everyday and main supervisor, Lars has always taken the time to help me in the laboratory and discuss results. He has taught me how to be an experimental physicist with respect for both experimental and theoretical work. Liv has inspired the direction of the experimental work with her great knowledge about the interstellar medium and PAHs in particular, which she has always been prepared to share when needed. Also, I would like to mention that in these two people I have found great support as well as sympathy and understanding when things have been tough.

I would like to thank the rest of the Molecular Dynamics group for taking the time to discuss my experimental results and help me in the laboratory even though the topic does not overlap with their work. I have had the pleasure to work in the laboratory with both talented post docs (Yoni, Aravind, and Joyti) as well as fellow PhD students (Dennis and Hjalte) during my PhD time. I am greateful for the fun, the runs and the collaboration we had. Also, thanks to Steen for taking the time to always answer my questions and to Kristian for invaluable help in the lab.

A laboratory cannot be run without technical assistance, and therefore I wish to thank the workshop and electronic department of the Insitute of Physics and Astronomy. The people working here have always been very helpful both in guiding and repairing equipment when

needed. Life in the laboratory has been a lot easier with their willingness to make things happen.

During my more than seven years at the Department of Physics and Astronomy, I have met many wonderful people who have made my time here very enjoyable. Lisbeth, Dennis, Hjalte, Camilla, Anne, and Maj-Britt have all made coming to work very enjoyable. Thanks for all the fun we had and useful discussions. Also, a big thanks to Dennis for the scientific notes on this thesis, and to Kristian for proofreading.

Last, I would like to appreciate the support of my family and friends for taking an interest in my work and trying to understand, why one wants to spend countless hours investigating a small family of molecules. This thesis would not have been written without the love and support from Kristian.

References

- [1] B. Klærke, A. I. S. Holm, and L. H. Andersen, *UV action spectroscopy of protonated PAH derivatives. Methyl substituted quinolines*, Astron. & Astrophys. **532**, A132 (2011).
- [2] B. Klærke, Y. Toker, D. B. Rahbek, L. Hornekær, and L. H. Andersen, *Formation and stability of hydrogenated PAHs in gas phase*, Astron. & Astrophys. **549**, A84 (2012).
- [3] S. R. Langhoff, C. W. Bauschlicher Jr., D. M. Hudgins, S. A. Sandford, and L. J. Allamandola, *Infrared spectra of substituted polycyclic aromatic hydrocarbons*, Jour. Phys. Chem. A **102**, 1632 (1998).
- [4] L. J. Allamandola, D. M. Hudgins, and S. A. Sandford, *Modeling the unidentified infrared emission with combinations of polycyclic aromatic hydrocarbons*, Astrophys. Jour. Lett. **511**, L115 (1999).
- [5] A. G. G. M. Tielens, *25 Years of PAH Hypothesis*, in PAHs and the Universe, EAS Publications Series, ed. C. Joblin and A. G. G. M. Tielens (EDP Sciences: Les Ulis, France) p. 3 (2011).
- [6] P. Ehrenfreund, S. Rasmussen, J. Cleaves, and L. Chen, *Experimentally tracing the key steps in the origin of life: The aromatic world*, Astrobiology **6**, 490 (2006).
- [7] C. D. K. Herd, A. Blinova, D. N. Simkus et al., *Origin and evolution of prebiotic organic matter as inferred from the Tagish Lake Meteorite*, Science **332**, 1304 (2011).
- [8] E. Habart, F. Boulanger, L. Verstraete, C. M. Walmsley, and G. Pineau des Forets, *Some empirical estimates of the H₂ formation rate in photon-dominated regions*, Astron. & Astrophys. **414**, 531 (2004).
- [9] E. Rauls and L. Hornekær, *Catalyzed routes to molecular hydrogen formation and hydrogen addition reactions on neutral polycyclic aromatic hydrocarbons under interstellar conditions*, Astrophys. Jour. **679**, 531 (2008).
- [10] H. Karttunen, P. Kröger, H. Oja, M. Poutanen, and K. J. Donner, *The interstellar medium*, in Fundamental Astronomy, Springer p. 289 (2007).

- [11] J. Cami, J. Bernard-Salas, E. Peeters, and S. E. Malek, *Detection of C₆₀ and C₇₀ in a young planetary nebula*, *Science* **329**, 1180 (2010).
- [12] T. P. Snow and V. M. Bierbaum, *Ion chemistry in the interstellar medium*, *Ann. Rev. Anal. Chem.* **1**, 229 (2008).
- [13] A. Leger and J. L. Puget, *Identification of the "unidentified" IR emission features of interstellar dust?*, *Astron. & Astrophys.* **137**, L5 (1984).
- [14] L. J. Allamandola, A. G. G. M. Tielens, and J. R. Barker, *Polycyclic aromatic hydrocarbons and the unidentified infrared emission bands - Auto exhaust along the Milky Way*, *Astrophys. Jour. Lett.* **290**, L25 (1985).
- [15] F. C. Gillett, W. J. Forrest, and K. M. Merrill, *8-13-micron spectra NGC 7027, BD+30°3639, and NGC 6572*, *Astrophys. Jour.* **183**, 87 (1973).
- [16] A. G. G. M. Tielens, *Interstellar polycyclic aromatic hydrocarbon molecules*, *Ann. Rev. Astron. Astrophys.* **46**, 289 (2008).
- [17] F. Salama, *PAHs in Astronomy - A review*, *Proceedings of the International Astronomical Union* **4**, 357 (2008).
- [18] P. W. Merrill, *Unidentified interstellar bands*, *Publications of the Astronomical Society of the Pacific* **46**, 206 (1934).
- [19] F. Salama and L. J. Allamandola, *Polycyclic aromatic hydrocarbon ions and the diffuse interstellar bands*, *Advance Space Research* **15**, 413 (1995).
- [20] F. Salama, G. A. Galazutdinov, J. Krelowski, L. J. Allamandola, and F. A. Musaev, *Polycyclic aromatic hydrocarbons and the diffuse interstellar bands: a survey*, *Astrophys. Jour.* **526**, 265 (1999).
- [21] A. Pathak and P. J. Sarre, *Protonated PAHs as carriers of diffuse interstellar bands*, *Mon. Not. Royal Astron. Soc.* **391**, L10 (2008).
- [22] M. Hammonds, A. Pathak, and P. J. Sarre, *TD-DFT calculations of electronic spectra of hydrogenated protonated polycyclic aromatic hydrocarbon (PAH) molecules: implications for the origin of the diffuse interstellar bands?*, *Phys. Chem. Chem. Phys.* **11**, 4458 (2009).
- [23] M. Steglich, J. Bouwman, F. Huisken, and T. Henning, *Can neutral and ionized polycyclic aromatic hydrocarbons be carriers of the ultraviolet extinction bump and the diffuse interstellar bands?*, *Astrophys. Jour.* **742**, 2 (2011).
- [24] F. Salama, G. A. Galazutdinov, J. Krelowski, L. Biennier, Y. Beletsky, and I.-O. Song, *Polycyclic aromatic hydrocarbons and the diffuse interstellar bands: a survey*, *Astrophys. Jour.* **728**, 154 (2011).
- [25] L. M. Hobbs, D. G. York, T. P. Snow, T. Oka, J. A. Thorburn, M. Bishof, S. D. Friedman, B. J. McCall, B. Rachford, P. Sonnentrucker, and D. E. Welty, *A catalog of diffuse interstellar bands in the spectrum of HD 204827*, *Astrophys. Jour.* **680**, 1256 (2008).

- [26] P. J. Sarre, *The diffuse interstellar bands: a major problem in astronomical spectroscopy*, Jour. Mol. Spectrom. **238**, 1 (2006).
- [27] A. G. G. M. Tielens, *The Physics and Chemistry of the Interstellar Medium*, Cambridge University Press (2005).
- [28] M. Rapacioli, C. Joblin, and P. Boissel, *Spectroscopy of polycyclic aromatic hydrocarbons and very small grains in photodissociation regions*, Astron. & Astrophys. **429**, 193 (2005).
- [29] C. Cecchi-Pestellini, G. Malloci, G. Mulas, C. Joblin, and D. A. Williams, *The role of the charge state of PAHs in ultraviolet extinction*, Astron. & Astrophys. **486**, L25 (2008).
- [30] D. M. Hudgins and L. J. Allamandola, *The spacing of the interstellar 6.2 and 7.7 micron emission features as an indicator of polycyclic aromatic hydrocarbon size*, Astrophys. Jour. Lett. **513**, L41 (1999).
- [31] W. A. Schutte, A. G. G. M. Tielens, and L. J. Allamandola, *Theoretical modeling of the infrared fluorescence from interstellar polycyclic aromatic hydrocarbons*, Astrophys. Jour. **415**, 397 (1993).
- [32] V. Le Page, T. P. Snow, and V. M. Bierbaum, *Hydrogenation and charge states of polycyclic aromatic hydrocarbons in diffuse clouds. II. Results*, Astrophys. Jour. **584**, 316 (2003).
- [33] T. Allain, S. Leach, and E. Sedlmayr, *Photodestruction of PAHs in the interstellar medium II. Influence of the states of ionization and hydrogenation*, Astron. & Astrophys. **305**, 616 (1996).
- [34] A. Simon and C. Joblin, *The computed infrared spectra of a variety of [FePAH]⁺ complexes: mid- and far-infrared features*, Astrophys. Jour. **712**, 69 (2010).
- [35] S. J. Clemett, C. R. Maechling, R. N. Zare, P. D. Swan, and R. M. Walker, *Identification of complex aromatic molecules in individual interplanetary dust particles*, Science **262**, 721 (1993).
- [36] M. P. Bernstein, S. A. Sandford, and L. J. Allamandola, *Hydrogenated polycyclic aromatic hydrocarbons and the 2940 and 2850 wavenumber (3.40 and 3.51 micron) infrared emission features*, Astrophys. Jour. Lett. **472**, L127 (1996).
- [37] G. C. Sloan, J. D. Bregman, T. R. Begalle, L. J. Allamandola, and C. E. Woodward, *Variations in the 3 micron spectrum across the orion bar: polycyclic aromatic hydrocarbons and related molecules*, Astrophys. Jour. **474**, 735 (1997).
- [38] D. R. Wagner, H. Kim, and R. J. Saykally, *Peripherally hydrogenated neutral polycyclic aromatic hydrocarbons as carriers of the 3 micron interstellar infrared emission complex: results from single-photon infrared emission spectroscopy*, Astrophys. Jour. **545**, 854 (2000).

- [39] L. W. Beegle, T. J. Wdowiak, and J. G. Harrison, *Hydrogenation of polycyclic aromatic hydrocarbons as a factor affecting the cosmic 6.3 micron emission band*, Spectrochimica Acta Part A **57**, 737 (2001).
- [40] G. Mallochi, G. Mulas, C. Cecchi-Pestellini, and C. Joblin, *Dehydrogenated polycyclic aromatic hydrocarbons and UV bump (research note)*, Astron. & Astrophys. **489**, 1183 (2008).
- [41] L. Verstraete, *The role of PAHs in the physics of the interstellar medium*, in PAHs and the Universe, EAS Publications Series, ed. C. Joblin and A. G. G. M. Tielens (EDP Sciences: Les Ulis, France) p. 415 (2011).
- [42] O. Berné, A. Fuente, J. R. Goicoechea, P. Pilloni, G. González-García, and C. Joblin, *Mid-infrared polycyclic aromatic hydrocarbon and H₂ emission as a probe of physical conditions in extreme photodissociation regions*, Astrophys. Jour. Lett. **706**, L160 (2009).
- [43] V. M. Bierbaum, V. Le Page, and T. P. Snow, *PAHs and the chemistry of the ISM*, in PAHs and the Universe, EAS Publications Series, ed. C. Joblin and A. G. G. M. Tielens (EDP Sciences: Les Ulis, France) p. 427 (2011).
- [44] M. Flenklach, D. W. Clary, W. C. Gardiner, and S. E. Stein, *Detailed kinetic modeling of soot formation in shock-tube pyrolysis of acetylene*, 20th Symp. (Int.) on Combustion, The Combustion Institute **20**, 887 (1984).
- [45] M. J. McEwan, G. B. I. Scott, N. G. Adams, L. M. Babcock, R. Terzieva, and E. Herbst, *New H and H₂ reactions with small hydrocarbon ions and their roles in benzene synthesis in dense interstellar clouds*, Astrophys. Jour. **513**, 287 (1999).
- [46] J. A. Cole, J. D. Bittner, J. P. Longwell, and J. B. Howard, *Formation mechanisms of aromatic compounds in aliphatic flames*, Combustion and Flame **56**, 51 (1984).
- [47] B. M. Jones, F. Zhang, R. I. Kaiser, A. Jamal, A. M. Mebel, M. A. Cordiner, and S. B. Charnley, *Formation of benzene in the interstellar medium*, Proceedings of the National Academy of Science **108**, 452 (2011).
- [48] G. Mulas, G. Mallochi, C. Joblin, and C. Cecchi-Pestellini, *Polycyclic aromatic hydrocarbons and the extinction curve*, in PAHs and the Universe, EAS Publications Series, ed. C. Joblin and A. G. G. M. Tielens (EDP Sciences: Les Ulis, France) p. 327 (2011).
- [49] P. Thaddeus, *The prebiotic molecules observed in the interstellar medium*, Philosophical Transaction of the Royal Society B **361**, 1681 (2006).
- [50] J. Szczepanski and M. Vala, *Infrared frequencies and intensities for astrophysically important polycyclic aromatic hydrocarbon cations*, Astrophys. Jour. **414**, 646 (1993).
- [51] C. Moutout, A. Leger, and L. d'Hendecourt, *Far-infrared emission of PAH molecules (14 – 40 μm): A preparation for ISO spectroscopy*, Astron. & Astrophys. **310**, 297 (1996).

- [52] D. M. Hudgins and L. J. Allamandola, *Interstellar PAH emission in the 11-14 micron region: New insights from laboratory data and a tracer for ionized PAHs*, *Astrophys. Jour. Lett.* **516**, L41 (1999).
- [53] D. Romanini, L. Biennier, F. Salama, A. Kachanov, L. J. Allamandola, and F. Stoeckel, *Jet-discharge cavity ring-down spectroscopy of ionized polycyclic aromatic hydrocarbons: progress in testing the PAH hypothesis for the diffuse interstellar band problem*, *Chem. Phys. Lett.* **303**, 165 (1999).
- [54] O. Sukhorukov, A. Staicu, E. Diegel, G. Rouillé, T. Henning, and F. Huisken, *$D_2 \leftarrow D_0$ transition of the anthracene cation observed by cavity ring-down absorption spectroscopy in a supersonic jet*, *Chem. Phys. Lett.* **3860**, 259 (2004).
- [55] G. Rouillé, S. Krasnokutski, F. Huisken, and T. Henning, *Ultraviolet spectroscopy of pyrene in a supersonic jet and in liquid helium droplets*, *Jour. Chem. Phys.* **120**, 6028 (2004).
- [56] X. Tan and F. Salama, *Cavity ring-down spectrometry and vibronic activity of benzog[ghi]perylene*, *Jour. Chem. Phys.* **123**, 01412 (2005).
- [57] C. L. Ricketts, C. S. Contreras, R. L. Walker, and F. Salama, *The coupling of a re-electron time-of-flight mass spectrometer with a cosmic simulation chamber: A powerful new toll for laboratory astrophysics*, *Int. Jour. Mass Spectrom.* **300**, 26 (2011).
- [58] C. Joblin, L. d'Hendecourt, A. Léger, and D. Défourneau, *Infrared spectroscopy of gas-phase PAH molecules*, *Astron. & Astrophys.* **281**, 923 (1994).
- [59] J. Oomens, A. J. A. van Roij, G. Meijer, and G. von Helden, *Gas-phase infrared photodissociation spectroscopy of cationic polyaromatic hydrocarbons*, *Astrophys. Jour.* **542**, 404 (2000).
- [60] J. Oomens, B. G. Sartakov, A. G. G. M. Tielens, G. Meijer, and G. von Helden, *Gas-phase infrared spectrum of the coronene cation*, *Astrophys. Jour. Lett.* **560**, L99 (2001).
- [61] J. Oomens, A. G. G. M. Tielens, B. G. Sartakov, G. von Helden, and G. Meijer, *Laboratory infrared spectroscopy of cationic polycyclic aromatic hydrocarbon molecules*, *Astrophys. Jour.* **591**, 968 (2003).
- [62] F. Useli-Bacchitta, A. Bonnamy, G. Mulas, G. Malloci, D. Toublanc, and C. Joblin, *Visible photodissociation spectroscopy of PAH cations and derivatives in the PIRENEA experiment*, *Chem. Phys.* **371**, 16 (2010).
- [63] H. S. Kim, D. R. Wagner, and R. J. Saykally, *Single photon infrared emission spectroscopy of the gas phase pyrene cation: Support for a polycyclic aromatic hydrocarbon origin of the Unidentified infrared emission bands*, *Phys. Rev. Lett.* **86**, 5691 (2001).
- [64] H. S. Kim and R. J. Saykally, *Single-photon infrared emission spectroscopy of gaseous polycyclic aromatic hydrocarbon cations: A direct test for proposed carriers of the unidentified infrared emission bands*, *Astrophys. Jour. Supp. Series* **143**, 455 (2002).

- [65] S. R. Langhoff, *Theoretical infrared spectra for polycyclic aromatic hydrocarbon neutrals, cations and anions*, Jour. Phys. Chem. **100**, 2819 (1996).
- [66] C. W. Bauschlicher Jr. and E. L. O. Bakes, *Infrared spectra of polycyclic aromatic hydrocarbons (PAHs)*, Chem. Phys. **262**, 285 (2000).
- [67] C. W. Bauschlicher Jr., *The infrared spectra of $C_{96}H_{24}$, $C_{96}H_{24}^+$ and $C_{96}H_{25}^+$* , Astrophys. Jour. **564**, 782 (2002).
- [68] G. Mallocci and G. M. C. Joblin, *Electronic absorption spectra of PAHs up to vacuum UV. Towards a detailed model of interstellar PAH photophysics*, Astron. & Astrophys. **426**, 105 (2004).
- [69] G. Mallocci, C. Joblin, and G. Mulas, *On-line database of the spectral properties of polycyclic aromatic hydrocarbons*, Chem. Phys. **332**, 353 (2007).
- [70] C. W. Bauschlicher Jr., E. Peeters, and L. J. Allamandola, *The infrared spectra of very large, compact, highly symmetric polycyclic aromatic hydrocarbons (PAHs)*, Astrophys. Jour. **678**, 316 (2008).
- [71] J. A. Rasmussen, G. Henkelman, and B. Hammer, *Pyrene: Hydrogenation, hydrogen evolution, and π -band model*, Jour. Chem. Phys. **134**, 164703 (2011).
- [72] A. J. Huneycutt, R. N. Casaes, B. J. McCall, C. Y. Chung, Y. P. Lee, and R. J. Saykally, *Infrared cavity ringdown spectroscopy of jet-cooled polycyclic aromatic hydrocarbons*, Phys. Chem. Phys. **5**, 321 (2004).
- [73] B. H. Bransden and C. J. Joachain, Physics of Atoms and Molecules, Benjamin Cummings (2nd Edition) (2003).
- [74] P. W. Atkins and R. Friedman, Molecular Quantum Mechanics, Oxford University Press (4th Ed) (2004).
- [75] P. Atkins and J. De Paula, Atkins' Physical Chemistry, Oxford University Press (2006).
- [76] P. Hohenberg and W. Kohn, *Inhomogeneous electron gas*, Phys. Rev. B **136**, B864 (1964).
- [77] C. Lee, W. Yang, and R. G. Parr, *Development of the Colle-Salvetti correlation-energy formula into a functional of the electron density*, Phys. Rev. B **37**, 785 (1988).
- [78] A. D. Becke, *Density-functional thermochemistry. III. The role of exact exchange*, Jour. Chem. Phys. **98**, 5648 (1993).
- [79] M. J. Frisch, G. W. Trucks, H. B. Schlegel et al., Gaussian 03, Revision C.02 (Wallingford, CT: Gaussian, Inc., 2004).
- [80] J. B. Foresman and A. Frisch, Exploring chemistry with electronic structure methods, Gaussianm Inc. (2nd edition, Pittsburgh, PA) (1996).

- [81] E. Runge and E. K. U. Gross, *Density-Functional Theory for Time-Dependent systems*, Phys. Rev. Lett. **52**, 997 (1984).
- [82] K. Burke, J. Werschnik, and E. K. U. Gross, *Time-dependent density functional theory: past, present, and future*, Jour. Chem. Phys. **123**, 062206 (2005).
- [83] <http://cccbdb.nist.gov/>.
- [84] A. J. Cohen, P. Mori-Sanchez, and W. Yang, *Insights into current limitations of density functional theory*, Science **321**, 792 (2008).
- [85] J. B. Fenn, M. Mann, C. K. Meng, S. F. Wong, and C. M. Whitehouse, *Electrospray ionization for mass spectrometry of large biomolecules*, Science **246**, 64 (1989).
- [86] E. P. Maziarz III, G. A. Baker, and T. D. Wood, *Electrospray ionization Fourier transform mass spectrometry of polycyclic aromatic hydrocarbons using silver(I)-mediated ionization*, Can. Jour. Chem. **83**, 1871 (2005).
- [87] T. Ghislain, P. Faure, and R. Michels, *Detection and monitoring of PAH and oxy-PAHs by high resolution mass spectrometry: Comparison of ESI, APCI and APPI source detection*, Jour. Am. Soc. Mass Spectrom. **23**, 530 (2012).
- [88] H. A. B. Johansson, H. Zettergren, A. I. S. Holm, N. Haag, S. B. Nielsen, J. A. Wyer, M. B. S. Kirketerp, K. S. chkel, P. Hvelplund, H. T. Schmidt, and H. Ced-erquist, *Unimolecular dissociation of anthracene and acridine cations: The importance of isomerization barriers for the C₂H₂ loss and HCN loss channels*, Jour. Chem. Phys. **135**, 084304 (2011).
- [89] M. Vala, J. Szczepanski, R. Dunbar, J. Oomens, and J. D. Steill, *Infrared multiphoton dissociation spectrum of isolated protonated 1-azapyrene*, Chem. Phys. Lett. **473**, 43 (2009).
- [90] K. O. Nielsen, *The development of magnetic ion sources for an electromagnetic isotope separator*, Nuclear Instruments **1**, 289 (1957).
- [91] S. Tomita, J. U. Andersen, C. Gottrup, P. Hvelplund, and U. V. Pedersen, *Dissociation energy for C₂ loss from fullerene cations in a storage ring*, Phys. Rev. Lett. **87**, 073401 (2001).
- [92] S. P. Møller, *ELISA, an electrostatic storage ring for atomic physics*, Nuclear Instruments and Methods in Physics Research Section A **394**, 281 (1997).
- [93] S. P. Møller, *Design and first operation of the electrostatic storage ring, ELISA*, Proceedings of 6th European Particle Accelerator Conference, Stockholm p. 73 (1998).
- [94] S. P. Møller and U. V. Pedersen, *Operational experience with the electrostatic storage ring, ELISA*, Proceedings of the 1999 Particle Accelerator Conference, New York p. 2295 (1999).

- [95] S. P. Møller, P. Bowe, J. S. Nielsen, and U. V. Pedersen, *Intensity limitations of the electrostatic storage ring ELISA*, Proceedings of EPAC 2000, Vienna p. 788 (2000).
- [96] L. H. Andersen, H. Bluhme, S. Boye, T. J. D. Jørgensen, H. Krogh, I. B. Nielsen, S. Brondsted Nielsen, and A. Svendsen, *Experimental studies of the photophysics of gas-phase fluorescent protein chromophores*, Phys. Chem. Chem. Phys. **6**, 2617 (2004).
- [97] D. B. Rahbek, *Photo-fragmentation and electron-detachment studies of gas-phase chromophore ions*, PhD Thesis (2012).
- [98] L. H. Andersen, *Lecture Notes* (2009).
- [99] J. U. Andersen, E. Bonderup, and K. Hansen, *Thermionic emission from clusters*, Jour. Phys. B. **35**, R1 (2002).
- [100] K. Stochkel, U. Kadkhane, J. U. Andersen, A. I. S. Holm, P. Hvelplund, M. S. Kirkegaard, M. K. Larsen, M. K. Lykkegaard, S. B. Nielsen, S. Panja, and H. Zettergren, *A new technique for time-resolved daughter ion mass spectrometry on the microsecond to millisecond time scale using an electrostatic ion storage ring*, Review of Scientific Instruments **79**, 023107 (2008).
- [101] M. P. Bernstein, A. L. Mattioda, S. A. Sandford, and D. M. Hudgins, *Laboratory infrared spectra of polycyclic aromatic nitrogen heterocycles: Quinoline and Phenanthridine in solid argon and H₂O*, Astrophys. Jour. **626**, 909 (2005).
- [102] D. M. Hudgins, C. W. Bauschlicher Jr., and L. J. Allamandola, *Variations in the peak position of the 6.2 μm interstellar emission feature: A tracer of N in the interstellar polycyclic aromatic hydrocarbon population*, Astrophys. Jour. **632**, 316 (2005).
- [103] A. L. Mattioda, D. M. Hudgins, C. W. Bauschlicher Jr., M. Rosi, and L. J. Allamandola, *Infrared Spectroscopy of matrix-isolated polycyclic aromatic compounds and their ions. 6. Polycyclic aromatic nitrogen heterocycles*, Jour. Phys. Chem. A **107**, 1486 (2003).
- [104] A. L. Mattioda, D. M. Hudgins, C. W. Bauschlicher Jr., and L. J. Allamandola, *Infrared spectroscopy of matrix-isolated polycyclic aromatic compounds and their ions. 7. Phenazine, a dual substituted polycyclic aromatic nitrogen heterocycle*, Advances in Space Research **36**, 156 (2005).
- [105] H. Alvaro Galué, O. Pirali, and J. Oomens, *Gas-phase infrared spectra of cationized nitrogen-substituted polycyclic aromatic hydrocarbons*, Astron. & Astrophys. **517**, A15 (2010).
- [106] E. Peeters, S. Hony, C. Van Kerckhoven, A. G. G. M. Tielens, L. J. Allamandola, D. M. Hudgins, and C. W. Bauschlicher Jr., *The rich 6 to 9 vec μ m spectrum of interstellar PAHs*, Astron. & Astrophys. **390**, 1089 (2002).
- [107] S. B. Charnley, Y. Kuan, H. Huang, O. Botta, H. M. Butner, N. Cox, D. Despois, P. Ehrenfreund, Z. Kisiel, Y. Lee, A. J. Markwick, Z. Peeters, and S. D. Rodgers, *Astronomical searches for nitrogen heterocycles*, Advances in Space Research **36**, 137 (2005).

- [108] P. G. Stoks and A. W. Schwartz, *Basic nitrogen-heterocyclic compounds in the Murchison meteorite*, *Geochimica et Cosmochimica Acta* **46**, 309 (1982).
- [109] M. A. Sephton, *Organic Compounds in Carbonaceous Meteorites*, *Natural Product Reports* **33**, 262 (2002).
- [110] A. Ricca, C. W. Bauschlicher Jr., and E. L. O. Bakes, *A computational study of the mechanisms for the incorporation of a nitrogen atom into polycyclic aromatic hydrocarbons in the Titan haze*, *Icarus* **154**, 516 (2001).
- [111] F. Salama, C. Joblin, and L. J. Allamandola, *Electronic absorption spectroscopy of matrix-isolated polycyclic aromatic hydrocarbon cations. II. The phenanthrene cation ($C_{14}H_{10}^+$) and its 1-methyl derivative*, *Jour. Chem. Phys.* **101**, 10252 (1994).
- [112] D. J. Cook, S. Schlemmer, N. Balucani, D. R. Wagner, B. Steiner, and R. J. Saykally, *Infrared emission spectra of candidate interstellar aromatic molecules*, *Nature* **380**, 227 (1994).
- [113] C. W. Bauschlicher Jr. and S. R. Langhoff, *Infrared spectra of polycyclic aromatic hydrocarbons: methyl substitution and loss of H*, *Chem. Phys.* **234**, 79 (1998).
- [114] M. M. Husain, M. S. Khan, and Z. H. Khan, *Electronic spectra of 1-methyl and 2-methyl phenanthrenes and their radical cations*, *Spectrochimica Acta Part A: Molecular and Biomolecular Spectroscopy* **56**, 2741 (2000).
- [115] V. Dryza, J. A. Sanelli, E. G. Robertson, and E. J. Bieske, *Electronic Spectra of Gas-Phase Polycyclic Aromatic Nitrogen Heterocycle Cations: Isoquinoline(+) and Quinoline(+)*, *Jour. Chem. Phys. A* **116**, 4323 (2012).
- [116] Y. A. Dyakov, C.-K. Ni, S. H. Lin, Y. T. Lee, and A. M. Mebel, *Ab initio and RRKM study of photodissociation of azulene cation*, *Phys. Chem. Chem. Phys.* **8**, 1404 (2006).
- [117] Y. Gotkis, M. Oleinikova, M. Naor, and C. Lifshitz, *Time-dependent mass spectra and breakdown graphs. 17. Naphthalene and phenanthrene*, *Jour. Phys. Chem.* **97**, 12282 (1993).
- [118] H. W. Jochims, E. Ruhl, H. Baumgartel, S. Tobita, and S. Leach, *Size effects on dissociation rates of polycyclic aromatic hydrocarbon cations: Laboratory studies and astrophysical implications*, *Astrophys. Jour.* **420**, 307 (1994).
- [119] A. I. S. Holm, H. Zettergren, H. A. B. Johansson et al., *Ions colliding with cold polycyclic aromatic hydrocarbon clusters*, *Phys. Rev. Lett.* **105**, 213401 (2010).
- [120] A. I. S. Holm, H. A. B. Johansson, H. Cederquist, and H. Zettergren, *Dissociation and multiple ionization energies for five polycyclic aromatic hydrocarbon molecules*, *Jour. Chem. Phys.* **134**, 044301 (2011).
- [121] A. Lawicki, A. I. S. Holm, P. Rousseau, M. Capron, R. Maisonne, S. Maclot, F. Seitz, H. A. B. Johansson, S. Rosén, H. T. Schmidt, H. Zettergren, B. Manil, L. Adoui, H. Cederquist, and B. A. Huber, *Multiple ionization and fragmentation of isolated pyrene and coronene molecules in collision with ions*, *Phys. Rev. A* **83**, 022704 (2011).

- [122] F. Seitz, A. I. S. Holm, H. Zettergren et al., *Polycyclic aromatic hydrocarbon-isomer fragmentation pathways: Case study for pyrene and flouranthene molecules and clusters*, Jour. Chem. Phys. **135**, 064302 (2011).
- [123] D. A. Williams, *Introductory lecture - Frontiers of astrochemistry*, Faraday Discuss. **109**, 1 (1998).
- [124] D. Hollenbach and E. E. Salpeter, *Surface recombination of hydrogen molecules*, Astrophys. Jour. **163**, 155 (1971).
- [125] N. Katz, I. Furman, O. Biham, V. Pirronello, and G. Vidali, *Molecular hydrogen formation on astrophysically relevant surfaces*, Astrophys. Jour. **522**, 305 (1999).
- [126] G. Manico, G. Raguní, V. Pirronello, J. E. Roser, and G. Vidali, *Laboratory measurements of molecular hydrogen formation on amorphous water ice*, Astrophys. Jour. Lett. **548**, L253 (2001).
- [127] L. Hornekær, A. Baurichter, V. V. Petrunin, D. Field, and A. C. Luntz, *Importance of surface morphology in interstellar H₂ formation*, Science **302**, 1943 (2003).
- [128] V. Mennella, *HD formation by abstraction of H/D chemisorbed in carbon grains with D/H atoms under simulated interstellar conditions*, Astrophys. Jour. Lett. **684**, L25 (2008).
- [129] V. Mennella, *Interaction of atomic hydrogen with carbon grains*, in PAHs and the Universe, EAS Publications Series, ed. C. Joblin and A. G. G. M. Tielens (EDP Sciences: Les Ulis, France) p. 393 (2011).
- [130] S. Cazaux and A. G. G. M. Tielens, *H₂ formation on grain surfaces*, Astrophys. Jour. **604**, 222 (2004).
- [131] Cuppen and E. Herbst, *Monte Carlo simulations of H₂ formation on grains of varying surface roughness*, Mon. Not. Royal. Astron. Soc. **361**, 565 (2005).
- [132] C. Joblin, J. P. Maillard, I. Vauglin, C. Pech, and P. Boissel, *Probing the Connection between PAHs and Hydrogen (H, H₂) in the Laboratory and in the Interstellar Medium*, in Molecular hydrogen in space, Cambridge Univ. Press, ed. F. Combes and G. Pineau des Forets (Cambridge) (2000).
- [133] P. Cassam-Chenaï, F. Pauzat, and Y. Ellinger, *Is stripping of polycyclic aromatic hydrocarbons a route to molecular hydrogen?*, in Molecules and Grains in Space, American Institute of Physics Conference Series, ed. I. Nenner (vol. 312) p. 543 (1994).
- [134] M. Hirama, T. Ishida, and J.-I. Aihara, *Possible molecular hydrogen formation mediated by the radical cations of anthracene and pyrene*, Comput. Chem. **24**, 1378 (2003).
- [135] F. Jolibois, A. Klotz, F. X. Gadéa, and C. Joblin, *Hydrogen dissociation of naphthalene cations: a theoretical study*, Astron. & Astrophys. **444**, 629 (2005).

- [136] V. Le Page, T. P. Snow, and V. M. Bierbaum, *Molecular hydrogen formation catalyzed by polycyclic aromatic hydrocarbons in the interstellar medium*, *Astrophys. Jour.* **704**, 274 (2009).
- [137] L. S. Rodrigues, F. Ruette, M. Sanchez, and C. Mendoza, *Interstellar catalysis: Formation of small molecules on a graphitic flake*, *Jour. Mol. Cat. A* **316**, 16 (2010).
- [138] S. Petrie, G. Javahery, and D. K. Bohme, *Gas-phase reactions of benzenoïs hydrocarbon ions with hydrogen atoms and molecules: uncommon constraints to reactivity*, *Jour. Am. Chem. Soc.* **114**, 9203 (1992).
- [139] G. B. I. Scott, D. A. Fairley, C. G. Freeman, M. J. McEwan, N. G. Adams, and L. M. Babcock, *$C_mH_n^+$ reactions with H and H_2 : An experimental study*, *Jour. Phys. Chem.* **101**, 4973 (1997).
- [140] V. Le Page, Y. Keheyian, V. M. Bierbaum, and T. P. Snow, *Chemical constraints on organic cations in the interstellar medium*, *Jour. Am. Chem. Soc.* **119**, 8373 (1997).
- [141] T. Snow, V. Le Page, Y. Keheyian, and V. Bierbaum, *The interstellar chemistry of PAH cations*, *Nature* **391**, 59 (1998).
- [142] C. W. Bauschlicher Jr., *The reaction of polycyclic aromatic hydrocarbon cations with hydrogen atoms: The astrophysical implications*, *Astrophys. Jour. Lett.* **509**, L125 (1998).
- [143] J. D. Thrower, L. Nilsson, B. Jørgensen, S. Baouche, R. Balog, A. C. Luntz, I. Stensgaard, E. Rauls, and L. Hornekær, *Superhydrogenated PAHs: Catalytic formation of H_2* , in PAHs and the Universe, EAS Publications Series, ed. C. Joblin and A. G. G. M. Tielens (EDP Sciences: Les Ulis, France) p. 453 (2011).
- [144] V. Mennella, L. Hornekær, J. Thrower, and M. Accolla, *The catalytic role of coronene for molecular hydrogen formation*, *Astrophys. Jour. Lett.* **745**, L2 (2012).
- [145] J. D. Thrower, B. Jørgensen, E. E. Friis, S. Baouche, V. Mennella, A. C. Luntz, M. Andersen, B. Hammer, and L. Hornekær, *Experimental evidence for the formation of highly superhydrogenated polycyclic aromatic hydrocarbons through H atom addition and their catalytic role in H_2 formation*, *Astrophys. Jour.* **752**, 3 (2012).
- [146] Y. Fu, J. Szczepanski, and N. C. Polfer, *Photon-induced formation of molecular hydrogen from a neutral polycyclic aromatic hydrocarbon: 9,10-dihydroanthracene*, *Astrophys. Jour.* **744**, 61 (2012).
- [147] M. Vala, J. Szczepanski, and J. Oomens, *Formation of molecular hydrogen from protonated 9,10-dihydroanthracene: Is the ejected H_2 rotationally and vibrationally excited?*, *Int. Jour. Mass Spectrom.* **308**, 181 (2011).
- [148] J. Szczepanski, J. Oomens, J. D. Steill, and M. T. Vala, *H_2 ejection from polycyclic aromatic hydrocarbons: Infrared multiphoton dissociation study of protonated acenaphthene and 9,10-dihydrophenanthrene*, *Astrophys. Jour. Lett.* **727**, 12 (2011).

- [149] T. M. Halansinski, F. Salama, and L. J. Allamandola, *Investigation of the ultraviolet, visible, and near-infrared absorption spectra of hydrogenated polycyclic aromatic hydrocarbons and their cations*, *Astrophys. Jour.* **628**, 555 (2005).
- [150] S. Chakraborty, R. Omidyan, I. Alata, I. B. Nielsen, C. Dedonder, M. Broquier, and C. Jouvet, *Protonated benzene dimer: An experimental and ab initio study*, *Jour. Am. Chem. Soc.* **131**, 11091 (2009).
- [151] A. M. Ricks, G. E. Doublerly, and M. A. Duncan, *The infrared spectrum of protonated naphthalene and its relevance for the unidentified infrared bands*, *Astrophys. Jour.* **702**, 301 (2009).
- [152] H. Knorke, J. Langer, J. Oomens, and O. Dopfer, *Infrared spectra of isolated protonated polycyclic aromatic hydrocarbon molecules*, *Astrophys. Jour. Lett.* **706**, L66 (2009).
- [153] I. Garkusha, J. Fulara, A. Nagy, and J. P. Maier, *Electronic absorption spectra of protonated anthracenes and phenanthrenes, and their neutrals in neon matrices*, *Astrophys. Jour.* **728**, 131 (2011).
- [154] I. Alata, C. Dedonder, M. Broquier, E. Marceca, and C. Jouvet, *Role of the charge-transfer state in the electronic absorption of protonated hydrocarbon molecules*, *Jour. Am. Chem. Soc.* **132**, 17483 (2010).
- [155] A. Bonaca and G. Bilalbegovic, *Electronic absorption spectra of hydrogenated protonated naphthalene and proflavine*, *Mon. Not. Royal Astron. Soc.* **416**, 1509 (2011).
- [156] A. Ricca, E. L. O. Bakes, and C. W. Bauschlicher Jr., *The energetics for hydrogen addition to naphthalene cation*, *Astrophys. Jour.* **659**, 858 (2007).
- [157] L. Boschman, G. Reitsma, S. Cazaux, T. Schlathölter, R. Hoekstra, M. Spaans, and O. González-Magaña, *Hydrogenation of PAH cation: A first step toward H₂ formation*, *Astrophys. Jour. Lett.* **761**, L33 (2012).
- [158] K. M. Ng, N. L. Ma, and C. W. Tsang, *Differentiation of isomeric polycyclic hydrocarbons by electrospray Ag(I) cationization mass spectrometry*, *Rapid Commun. Mass Spectrom.* **17**, 2082 (2003).
- [159] A. Charkraborty, D. Nath, M. Halder, N. Guchhait, and M. Chowdury, *Spectral assignment of dual conformers of 1,2,3,6,7,8-hexahydrophenanthrene in the supersonic jet*, *Jour. Chem. Phys.* **114**, 865 (2001).
- [160] P. J. Morgan, J. R. Roscioli, A. J. Fleisher, and D. W. Pratt, *Measuring the conformational properties of 1,2,3,6,7,8-hexahydrophenanthrene and its *ander der Waals* complexes*, *Jour. Chem. Phys.* **133**, 024302 (2010).
- [161] S. B. Nielsen, A. Lapierre, J. U. Andersen, U. V. Pedersen, L. H. Andersen, and S. Tomita, *Absorption spectrum of the green fluorescent protein chromophore anion in vacuo*, *Phys. Rev. Lett.* **87**, 228102 (2001).

- [162] L. H. Andersen, I. B. Nielsen, M. B. Kristensen, M. O. A. E. Ghazaly, S. Haacke, M. B. Nielsen, and M. Åxman Petersen, *Absorption of Schiff-base retinal chromophores in vacuo*, Jour. Am. Chem. Soc. **127**, 12347 (2005).